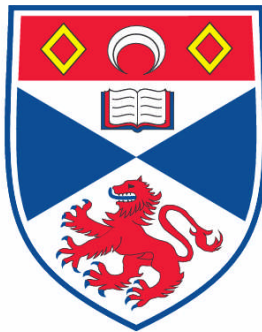


**OPTICALLY CONTROLLED MICROFLUIDICS**

**Steven Leonard Neale**

**A Thesis Submitted for the Degree of PhD  
at the  
University of St. Andrews**



**2008**

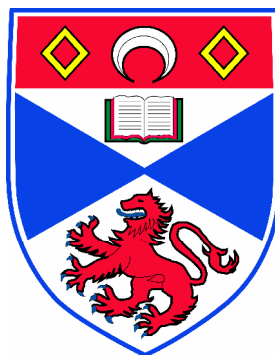
**Full metadata for this item is available in the St Andrews  
Digital Research Repository  
at:  
<https://research-repository.st-andrews.ac.uk/>**

**Please use this identifier to cite or link to this item:  
<http://hdl.handle.net/10023/147>**

**This item is protected by original copyright**

**This item is licensed under a  
Creative Commons License**

# **Optically Controlled Microfluidics**



**Thesis presented for the degree of  
Doctor of Philosophy  
to the University of St Andrews**

**by  
Steven Leonard Neale, MSci**

School of Physics and Astronomy  
University of St. Andrews  
North Haugh  
St. Andrews  
Scotland KY16 9SS

September, 2006

## **Declarations**

I, Steven Leonard Neale, hereby certify that this thesis, which is approximately twenty eight thousand words in length, has been written by me, that it is a record of the work carried out by me and that it has not been submitted in any previous application for a higher degree.

Signature of candidate:

Date:

I was admitted as a research student and as a candidate for the degree of Doctor of Philosophy in September, 2002; the higher study for which this is a record was carried out at the University of St Andrews between 2002 and 2006.

Signature of candidate:

Date:

I hereby certify that the candidate has fulfilled the conditions of the Resolution and Regulations appropriate for the degree of Doctor of Philosophy in the University of St Andrews and that the candidate is qualified to submit this thesis in application for that degree.

Signature of supervisor:

Date:

In submitting this thesis to the University of St Andrews I understand that I am giving permission for it to be made available for use in accordance with the regulations of the University Library for the time being in force, subject to any copyright vested in the work not being affected thereby. I also understand that the title and abstract will be published, and that a copy of the work may be made and supplied to any bona fide library or research worker, that my thesis will be electronically accessible for personal or research use, and that the library has the right to migrate my thesis into new electronic forms as required to ensure continued access to the thesis. I have obtained any third-party copyright permissions that may be required in order to allow such access and migration.

Signature of candidate:

Date:

## **Acknowledgements**

Firstly, I would like to acknowledge the role of my supervisor Thomas F Krauss, without whose help and encouragement this thesis would not exist. Thank you for your endless enthusiasm and constant stream of (usually) good ideas.

I would also like to acknowledge the help and support of my family and friends. I would especially like to thank my parents and Jenny, your patience has been greatly appreciated.

## **Publications**

Journal publications;

- 1 Cell Cytometry with a Light Touch: Sorting Microscopic Mater with a Light Touch. *Journal of Biological Regulators and Homeostatic Agents*, 18 (2), pp. 200-205, (2004).
- 2 All Optical Control of Microfluidic Components Using Form Birefringence. Steven L. Neale, Michael P. MacDonald, Kishan Dholakia, Thomas F. Krauss. *Nature Materials* 4 (7): 530-533 (2005).
- 3 Limiting factors to the size resolution achievable with Light Induced Dielectrophoresis (LIDEP). S.L. Neale, M Mazilu, M.P. MacDonald, J.I.B. Wilson, K. Dholakia and T.F. Krauss. In preparation (2006).

Conference publications;

- 4 Microfluidic Optical Sorting: Particle selection in an optical lattice. Michael P. MacDonald, Steven L. Neale, Lynn Paterson, Andrew Riches, Gabriel C. Spalding and Kishan Dholakia. *Proceedings of Optical Trapping and Optical Micromanipulation*, SPIE Vol 5514, pp. 1, (2004).
- 5 Optically actuated form birefringent microfluidic components. Steven L. Neale, Michael P MacDonald, Kishan Dholakia and Thomas F. Krauss. *Proceedings of Optical Trapping and Optical Micromanipulation II*, SPIE Vol 5930 (2005).
- 6 Size resolution with light-induced dielectrophoresis (LIDEP). S.L. Neale, M Mazilu, M.P. MacDonald, J.I.B. Wilson, K. Dholakia and T.F. Krauss. *Proceedings of Optical Trapping and Optical Micromanipulation III*, SPIE Vol 6326 (2006).
- 7 Spatial resolution of Light Induced Dielectrophoresis (LIDEP). SL Neale, M Mazilu, JIB Wilson, MP MacDonald, K Dholakia and TF Krauss. Proceeding of Photon 06, not yet published.

# CONTENTS

0.1 Abstract . . . . .	1
1 Introduction	2
1.1 Microfluidics . . . . .	3
1.1.1 Definitions . . . . .	3
1.1.2 Knudsen number . . . . .	4
1.1.3 Reynolds Number . . . . .	5
1.1.4 Mixing by diffusion . . . . .	6
1.1.5 Flow Resistance . . . . .	6
1.2 Optical tweezers . . . . .	7
1.2.1 Particle tracking . . . . .	9
Bibliography	11
2 Microgears	14
2.1 Introduction . . . . .	14
2.1.1 Rotating microgears with optical forces, the state of the art . . . . .	14

## CONTENTS

---

2.1.2	Gradient force . . . . .	16
2.1.3	Scattered light . . . . .	16
2.1.4	Transfer of angular momentum . . . . .	16
2.2	Simulation . . . . .	19
2.2.1	FIMMwave simulations . . . . .	19
2.3	Optical Setup . . . . .	23
2.4	Fabrication . . . . .	25
2.4.1	Microfabrication techniques . . . . .	25
2.4.2	Silicon microgears . . . . .	28
2.4.3	Polymer microgears . . . . .	36
2.4.4	Photonic Crystal MicroGears (PCMg) . . . . .	43
2.5	Results . . . . .	49
2.5.1	Circularly polarised light . . . . .	49
2.6	Summary and Outlook . . . . .	53
2.6.1	Increasing the birefringence . . . . .	53
2.6.2	Multiple pass systems . . . . .	56
2.6.3	A new way to make the world go 'round? . . . . .	58
2.6.4	Conclusion . . . . .	60
2.7	Appendix . . . . .	61
2.7.1	Reactive Ion Etching . . . . .	61
	Bibliography	67
3	Optical Sorting	69
3.1	Introduction . . . . .	69
3.1.1	State of the art, Fluorescence-Activated Cell Sorting FACS	70
3.2	Fabrication of a microfluidic flow chamber . . . . .	74
3.2.1	Photolithography . . . . .	74

## CONTENTS

---

3.2.2	SU-8 microfluidic channels . . . . .	76
3.2.3	PDMS microfluidic channels . . . . .	77
3.3	Optical setup . . . . .	87
3.4	Results . . . . .	91
3.5	Conclusions . . . . .	96
	Bibliography	97
4	Light Induced Dielectrophoresis (LIDEP)	99
4.1	Introduction . . . . .	100
4.1.1	Dielectrophoresis (DEP) . . . . .	100
4.1.2	Clausius-Mossotti Factor . . . . .	102
4.1.3	Dielectrophoresis of cells . . . . .	103
4.1.4	Light Induced Dielectrophoresis . . . . .	107
4.1.5	State of the art . . . . .	108
4.2	Simulation . . . . .	110
4.2.1	COMSOL and the Finite Element Method . . . . .	110
4.2.2	Maxwell's equations and the The Quasi Static Approximation . . . . .	111
4.2.3	The quasi static approximation . . . . .	113
4.2.4	Boundary conditions . . . . .	114
4.2.5	Subdomain settings . . . . .	115
4.2.6	Checking the simulated potential drop against circuit analysis . . . . .	116
4.2.7	Plotting the electrical fields . . . . .	120
4.2.8	Plotting the gradient of the square of the electrical field .	123
4.3	Fabrication . . . . .	126
4.3.1	Dielectrophoresis chamber . . . . .	126

## CONTENTS

---

4.3.2	Light Induced Dielectrophoresis (LIDEP) chamber . . . . .	128
4.4	Optical setup . . . . .	131
4.4.1	Light Induced Dielectrophoresis (LIDEP) with a laser . .	131
4.4.2	LIDEP with a data projector . . . . .	133
4.5	Results . . . . .	135
4.5.1	Traditional dielectrophoresis (DEP) . . . . .	135
4.5.2	Dielectrophoresis (DEP) of red blood cells . . . . .	137
4.5.3	Light Induced Dielectrophoresis (LIDEP) . . . . .	139
4.6	Conclusions . . . . .	151
4.6.1	Dielectrophoresis (DEP) . . . . .	151
4.6.2	Light Induced Dielectrophoresis (LIDEP) . . . . .	151
4.6.3	Future development . . . . .	153
	Bibliography	155
5	Conclusions	158
5.1	Microgears . . . . .	158
5.1.1	Increasing the rotation rate . . . . .	159
5.1.2	Microgear applications . . . . .	160
5.2	Optical Sorting . . . . .	160
5.2.1	Fabricating a flow chamber . . . . .	160
5.2.2	Maximum flow rate for optical sorting . . . . .	161
5.3	Light Induced Dielectrophoresis (LIDEP) . . . . .	161
5.3.1	Designing a LIDEP device . . . . .	161
5.3.2	Combining a LIDEP chamber with microfluidic channels	163
5.3.3	The future of LIDEP . . . . .	164
5.4	Optically controlled microfluidics . . . . .	166

## **CONTENTS**

---

Bibliography	168
--------------	-----

## **0.1. ABSTRACT**

---

### **0.1 Abstract**

Three projects are described in this thesis that combine microfabrication techniques with optical micromanipulation. The aim of these projects is to use expertise in microlithography and optical tweezing to create new tools for Lab-on-Chip devices.

The first project looks at the creation of microgears that can be moved using an optical force. The microgears include one dimensional photonic crystal that creates birefringence. This allows the transfer of angular momentum from a circularly polarised light beam to the microgear, making them spin. The microgears are simulated, fabricated and tested. Possible biological applications are suggested.

The second project looks at creating microchannels to perform micromanipulation experiments in. Different methods of fabricating the microfluidic channels are compared, and the resulting chambers are used to find the maximum flow rate an optical sorting experiment can be performed at.

The third project involves using a thin photoconductive layer to allow the optical control of an electrical force called dielectrophoresis. This light induced dielectrophoresis (LIDEP) allows similar control to optical tweezing but requires less irradiance than optical tweezing, allowing control over a larger area with the same input optical power. A LIDEP device is created and experiments to measure the electrical trap size that is created with a given optical spot size are performed.

These three projects show different microfabrication techniques, and highlight how well suited they are for use in optical manipulation and microfluidic experiments. As the size of objects that can be optically manipulated matches well with the size of objects that can be created with microfabrication, it seems likely that many more interesting applications will develop.

---

---

# CHAPTER 1

---

## Introduction

Technology led advances in miniaturization along with interest in micrometer and nanometer scale machining have accelerated since Feynman's prophetic talk "There's Plenty of Room at the Bottom" (1959)[1]. In computing for example advances in miniaturization technology allowed a revolution that has shaped all aspects of modern day life. Later the same technologies have been used in other fields, such as optics where microfabrication techniques taken straight from the semiconductor microchip industry have allowed the creation of sub wavelength features that can be used to guide light and much more [2].

Early pioneers who used micro machining techniques to create a fluidic chip for the sensing of chemical and biological components were Harrison and Manz in 1992 [3]. Early efforts were concentrated on the electrokinetic control of liquids using electroosmotic forces [4]. These early devices were typically used to perform separation techniques like capillary electrophoresis. Advantages of miniaturization are increased speed of analysis, increased reproducibility and

## **1.1. MICROFLUIDICS**

---

reduction in reagent consumption. Multiple tests can be carried out at the same time increasing confidence in the results. However, it was realized early on that the real benefits would come from integrating many processes onto one chip, thereby eliminating manual labour time. Human errors such as pipetting errors would also be reduced [5]. The field came to be known as Lab-on-Chip (LOC) which has since proliferated with many active research groups [6][7][8][9], dedicated journals [10][11], and dedicated conferences [12][13]. Recently, commercial devices have also become available that use LOC technology [14] to analyze DNA, RNA and cells with many different techniques [15]. An example system consists of a machine the size of a desktop computer that reads a disposable cassette. The processes available include cell fluorescence assays and RNA fragmentation, analysis and quality assurance. Also DNA analysis and Polymerase chain reaction (PCR) end point monitoring process are available [16]. Different processes use the same reading machine with different cassette kits.

### **1.1 Microfluidics**

#### **1.1.1 Definitions**

Microfluidics: fluid phenomena in microstructures with one dimension 0.1 to 100  $\mu m$ .

Nanofluidics: fluid phenomena in nanostructures with one dimension less than 100 nm.

Lab-on-a-chip: microfluidic system for the generation, manipulation or analysis of (bio)chemical information [17]. The term micro Total Analytical System ( $\mu TAS$ ) refers to a system similar to a Lab-on-a-chip but with integrated sample preparation steps such as reaction chambers or mixers. Recent years have

## 1.1. MICROFLUIDICS

---

seen a huge surge of interest in the field of microfluidics fueled mainly by the promise of Lab-On-Chip (LOC) devices. Miniaturization may cause a revolution in fluidics similar to the one it caused in computing as using similar technologies may give similar benefits of speed and parallel processing. To study microfluidics it is first necessary to look at two dimensionless numbers, the Knudsen number and the Reynolds number, that show how fluid flow on the micro scale differs from that on the macro scale.

### 1.1.2 Knudsen number

The equations that govern fluid flow on a macro scale are based on a continuum hypothesis which assumes that the number of molecules in the fluid is large enough for statistical averages to be valid. The continuum hypothesis is valid for systems that have a Knudsen number less than 0.01 [18]. The Knudsen number is defined by equation 1.1.

$$K_n = \frac{\lambda}{L} \quad (1.1)$$

Where  $\lambda$  is the mean free molecular path and  $L$  is a characteristic length for the system such as the diameter of a channel. The mean free path for a water molecule at room temperature and pressure is  $1.1 \times 10^{-7} m$ . From this we find that the Knudsen number is less than 0.01 for channels larger than  $11 \mu m$  diameter. As the microfluidic channels used here (see section 3) are  $100 \mu m$  diameter this means the continuum hypothesis is valid. When we go down from the micro to the nano scale this assumption can be invalid and single molecular approaches are needed. Thus the equations that govern fluid flow on a macro scale in general also hold on a micro scale. However this is only a general rule and there are exceptions such as for gas flow in the micro range where the continuum hypothesis can become invalid. The main equations to

## 1.1. MICROFLUIDICS

---

describe fluid dynamics are the Navier-Stokes equations which only have a few analytical solutions.

### 1.1.3 Reynolds Number

An important description of a flow is its Reynolds number. The Reynolds number of a system is the ratio of the inertial forces to the viscous forces acting on the fluid. When the viscous forces dominate the flow is laminar, when the inertial forces dominate the flow is turbulent. The transition occurs when this ratio is around 2300. Thus the Reynolds number can be used as a measure of the transition between laminar and turbulent flow. As the velocity of fluid through a given geometry is increased, the Reynolds number is increased. The Reynolds number for flow down a channel is given by equation 1.2.

$$Re = \frac{\rho v l}{\mu} \quad (1.2)$$

Where  $\rho$  is the density,  $v$  is the average velocity,  $l$  is the most relevant length scale (for a circular pipe the diameter), and  $\mu$  is the viscosity. So for a pipe 10cm in diameter a Reynolds number of 2300 gives a flow velocity of 4.6 cm per second. This means that any flow velocity faster than this would give turbulent flow. As the size of the pipe increases the velocity at which the fluid becomes turbulent decreases and hence most macroscopic flows are turbulent. For a microfluidic channel of diameter  $100\mu m$  with flow of velocity  $10\mu s^{-1}$  the Reynolds number is 0.001. This shows that for microfluidic channels flow will be laminar. This is important for optical sorting experiments where laminar flow is required (see section 3).

The size of the channels is an important aspect of a LOC device. The channels need to be large enough for the application but if too large mixing will take too long as the only mixing mechanism in laminar flow is diffusion.

## 1.1. MICROFLUIDICS

---

This gives us an optimal regime for most microfluidic applications of between 10 and 100  $\mu\text{m}$  [5].

### 1.1.4 Mixing by diffusion

If the flow is laminar, no turbulent mixing occurs and all the mixing is by diffusion. The distance traveled by diffusion is given by:

$$d_{diff} = \sqrt{2Dt} \quad (1.3)$$

Where  $d_{diff}$  is the distance traveled by diffusion. D is the diffusion coefficient and t is the time. The time the particles have to diffuse across the channel is equal to the channel length divided by the fluid velocity. If the particles are 1  $\mu\text{m}$  spheres the diffusion coefficient is  $0.4 \mu\text{m}^2\text{s}^{-1}$ . Then for a sorting experiment (see section 3) where the channel is 200  $\mu\text{m}$  long and the fluid velocity is  $10 \mu\text{ms}^{-1}$  then the diffusion time is 20s. This gives a diffusion distance of 4  $\mu\text{m}$ . This means that if the channels are 100  $\mu\text{m}$  wide the particles will only diffuse across a very small proportion of their width. If the particles are larger, the diffusion coefficient is lower so the mixing takes even longer. Also, as the channels get larger the distance the particles have to diffuse gets larger and the time this takes goes up by the square of the distance. Thus large particles can take a long time to diffuse across wide channels.

### 1.1.5 Flow Resistance

Flow through a microfluidic channel can be controlled using a syringe pump. When flow is due to a known pressure difference the volume flow rate can be calculated if the flow resistance is also known. The flow resistance for a cylindrical channel is given by equation 1.4.

## 1.2. OPTICAL TWEEZERS

---

$$R_{flow} = \frac{8\mu L}{\pi r^4} \quad (1.4)$$

Where  $R_{flow}$  is the flow resistance,  $\mu$  is the viscosity,  $L$  is the channels length and  $r$  is the channels radius. The volume flow rate can then be gained from equation 1.5.

$$Q = \frac{\Delta P}{R_{flow}} \quad (1.5)$$

Where  $Q$  is the volume flow rate and  $\Delta P$  is the pressure drop [17]. This shows us that the pressure necessary for a given flow rate increases with  $r^{-4}$ . This means that as there is a limit to the pressure that the syringe pump can apply there is a limit to flow rate that it can achieve through small channels. However for experiments with optical manipulation the flow rates generally used are so slow that this is not usually a problem. It is necessary to note that a flow set up by a pressure difference forms a parabolic Poiseuille flow profile with slower flow at the edges of the channels than in the center.

## 1.2 Optical tweezers

When a microscopic particle is illuminated with a well focused laser beam it can experience forces exerted by light strong enough to move it around. When these forces are used to pick up and move a particle they are referred to as optical tweezers, a phenomenon first studied by Ashkin in 1986 [19]. A particle in an optical field experiences a total force  $F_{mag}$  where:

$$F_{mag} = (F_s^2 + F_g^2)^{1/2} \quad (1.6)$$

Where  $F_s$  is the scattering force and  $F_g$  is the optical gradient force (see figure 1.1). The magnitude of the optical gradient force is given by [20]:

## 1.2. OPTICAL TWEEZERS

---

$$F_g = -\frac{n_m^2 r^3}{2} \left( \frac{n_p^2 - n_m^2}{n_p^2 + 2n_m^2} \right) \nabla E^2 \quad (1.7)$$

Where  $n_m$  and  $n_p$  are the refractive indices of the medium and the particle respectively,  $r$  is the radius of the particle and  $E$  is the electric field. This force acts in the direction of increasing optical gradient and is typically in the range of  $pN$  to  $fN$ . For large particles (Mie regime  $r > \lambda$ ) the reason for this can be understood using a ray optics approach, see figure 1.1.

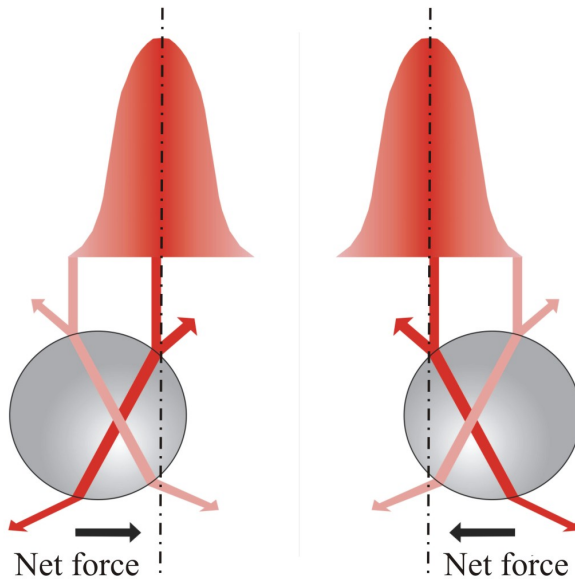


Figure 1.1: A dielectric particle in a Gaussian laser beam. Light reflected and refracted by the sphere apply force to it. The particle experiences a net force towards the center of the beam, if the gradient force is stronger than the scattering force, as the light is more intense in the center.

## 1.2. OPTICAL TWEEZERS

---

This shows a sphere in a Gaussian beam and how it reflects and refracts light. If the gradient force, due to the refracted light, is stronger than the scattering force, due to the reflected light, the particle will feel a net force towards the center of the beam.

For smaller particles (Rayleigh regime  $r < \lambda$ ) we can not use ray optics approach. Instead we consider the particle's polarisability. When a polarisable particle is placed in an electric field a dipole is set up within the particle. This dipole will feel a force if there is a gradient in the electric field, towards the stronger electric field and hence towards the higher optical intensity. Again there is a scattering force due to reflections, so the particle is only trapped when the gradient force is stronger than the scattering force.

### 1.2.1 Particle tracking

Many of the experiments in the thesis rely on the tracking of the movement of colloidal particles under various forces. This was accomplished using a particle tracking program called StAT written in LabVIEW by Graham Milne.

This program relies on the pattern matching features built into LabVIEW and allow the user to track any size and shape particle. Once the video to be analyzed has been converted into a set of bitmap images the program allows one to define the particle to be tracked on the first frame and then follows this and any other similar particles through the video plotting their trajectory (see figure 1.2). This approach has proved very successful for tracking one species of colloid in the presence of another as different refractive indices can be distinguished. One limitation of the program is shown if figure 1.2. A particle touching the edge of the screen or another particle may not be recognised by the pattern matching, here it has not seen the lowest particle. The program has been made freely available through the website of the Optical Trapping

## 1.2. OPTICAL TWEEZERS

---

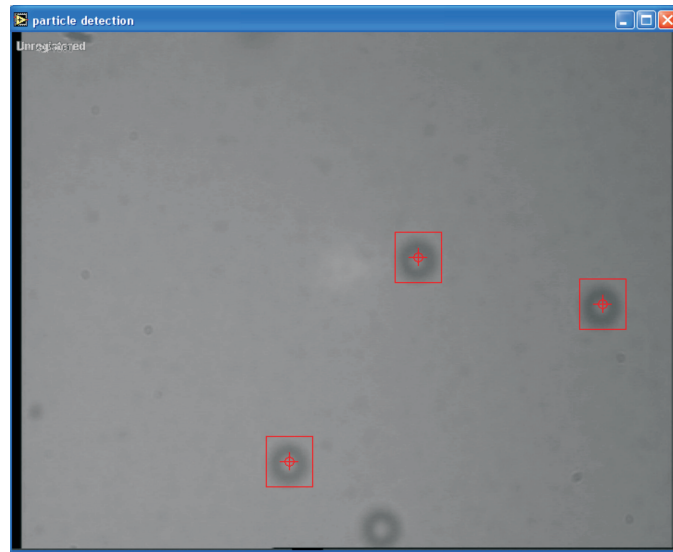


Figure 1.2: This figure shows a screen shot of StAT tracking particles.  $5\mu m$  colloid can be seen marked with red boxes that show the program has recognised them.

Group of the University of St Andrews [21].

---

## BIBLIOGRAPHY

- [1] Feynman RP. There's Plenty of Room at the Bottom. Talk given at the annual meeting of the American Physical Society 1959.
- [2] Krauss TF, DeLaRue RM, Brand S. Two-dimensional photonic-bandgap structures operating at near infrared wavelengths. *Nature* 383 (6602): 699-702 OCT 24 1996
- [3] Harrison JD, Manz A, Fan Z, Ludi H, Widmer HM. Capillary Electrophoresisand Sample Injection Systems Integrated on a Planar Glass Chip. *Anal Chem* 1992 Vol 64 p1926-1932.
- [4] Harrison JD, Manz A, Fan Z, Fluir K, Fan Z, Effenhauser CS. Micromachining a miniaturized capillary electrophoresis-based chemical analysis system. *Science* 261 p895-897
- [5] Bousse L, Cohen C, Nikiforov T, Chow A, Kopf-Sill AR, Dubrow R, Parce JW. Electrokinetically Controlled Microfluidic Analysis Systems. *Annual Review of Biophysics and Biomolecular Structures* 2000 29:155-81

## BIBLIOGRAPHY

---

- [6] Ramsey JM. MIC, Technical University of Denmark,  
<http://www.mic.dtu.dk/research/microtas/microtas.htm>
- [7] Manz A. Imperial College London,  
<http://www.achem.ic.ac.uk/Web2002/zentral20group%20page.htm>
- [8] van den Berg A. The Lab-on-a-Chip Group, University of Twente,  
<http://www.mesaplus.utwente.nl/mutas/bios/index.php>
- [9] Harrison JD. Department of Chemistry, University of Alberta,  
<http://www.chem.ualberta.ca/faculty/harrison.htm>
- [10] Lab on a Chip, Published by the Royal Society of Chemistry, Chairman  
Manz A.
- [11] microTAS, a virtual journal on micro Total Analysis Systems, Edited by  
van den Berg A.
- [12] microTAS 2003, <http://ww.mictotas2003.org/>
- [13] Microfluidics, Physics and Chemistry of,  
<http://grc.org/programs/2003/microflu.thm>
- [14] Caliper, <http://www.caliper.com/>
- [15] Agilent, <http://www.chem.agilent.com/Scripts/PDS.asp?lPage=51>
- [16] Agilent Bioanalyzer 2100 applications,  
<http://www.chem.agilent.com/scripts/LiteratureResults.asp?iproductotype=4&1115>
- [17] Andresson H, van den Berg A. Microfluidics for Lab-on-Chip, FSRM  
Training Course

## BIBLIOGRAPHY

---

- [18] Happel and Brenner, Low reynolds number hydrodynamics, Prentice Hall (1965)
- [19] Ashkin A, Dziedzic JM, Bjorkholm JE, Chu S, Optics Letters, 11, 288 (1986)
- [20] Hughes M.P., Nanoelectromechanics in engineering and biology, CRC Press (2003).
- [21] <http://www.st-andrews.ac.uk/%7Egfm2/tracker.htm>

---

---

# CHAPTER 2

---

## Microgears

### 2.1 Introduction

#### 2.1.1 Rotating microgears with optical forces, the state of the art

Since they were first demonstrated in 1986 [1] optical tweezers (see section 1.2) have rapidly developed into a diverse research area giving physicists and biologists control over the micro world. No longer just used to move particles around, optical tweezers have formed a comprehensive micro tool kit. One valuable tool is the ability to rotate or align micro particles to a particular direction.

Applications in biology for rotating particles in optical tweezers include microrheology [2] and the application of force to biological samples. Furthermore if sufficient torque can be generated, rotating particles can also be used to create pumps and valves for the growing areas of Lab-On-a-Chip (LOC)

## 2.1. INTRODUCTION

---

and micro Total Analysis Systems (microTAS). Here it is envisioned to perform experiments that were traditionally carried out on macroscopic samples in centralised laboratories, on tiny volumes of analyte on a microfluidic chip. They could also be used to help mixing which is a problem as discussed in section 1.1.4.

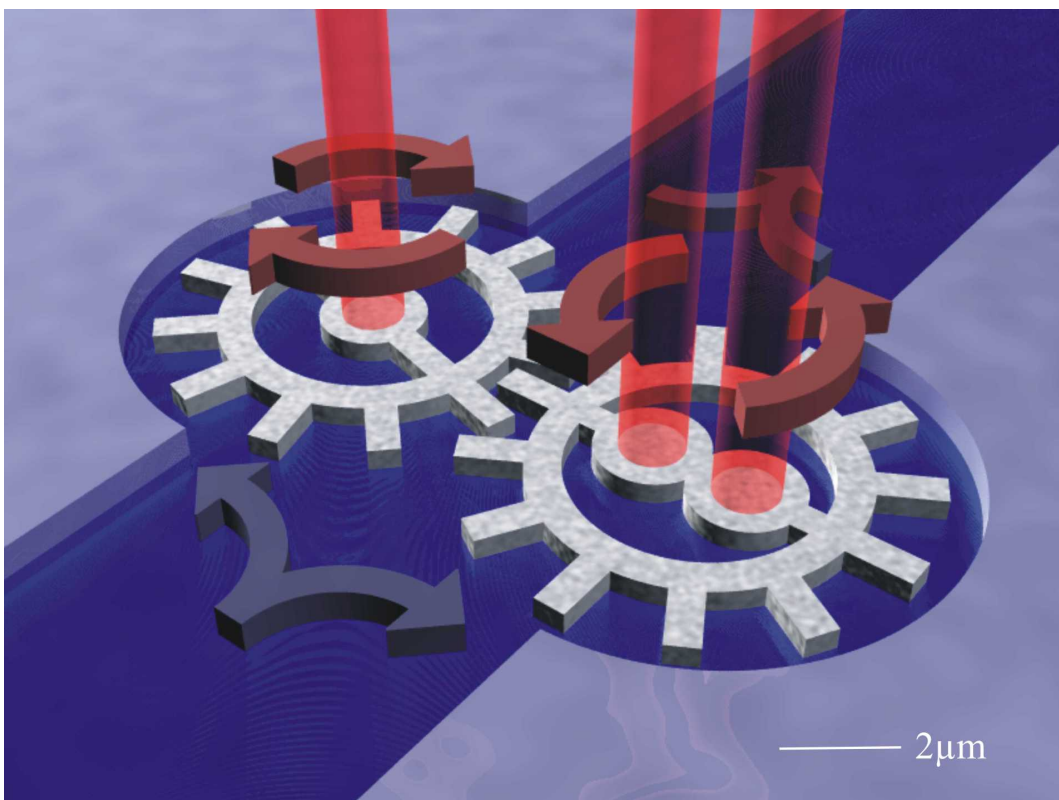


Figure 2.1: A microgear pump. Silicon microgears are optically tweezed by a rotating light pattern (red arrows) driving fluid through the channel (blue arrows).

Rotation of microscopic particles whilst holding them in an optical trap has been demonstrated in a number of different ways. The methods can be split into three groups differentiating them by driving forces.

## 2.1. INTRODUCTION

---

### 2.1.2 Gradient force

An asymmetric particle can be rotated by the optical gradient force (see section 1.2) with a rotating light pattern. The principle of this idea has been demonstrated [3] but not applied to any specific applications. The motivation for this work was to create an optically powered micropump (see figure 2.1).

### 2.1.3 Scattered light

The second group depend on the scattering of light from an appropriately shaped object (similar to a propeller in a fluid) to use radiation pressure as the driving force [4, 5, 6]. This approach has the advantage of simplicity as no complicated light pattern is required. It suffers from the drawback of not being able to precisely rotate the microgear or align it but to only spin it at a speed controlled by the input power. The scattering forces also push the particle away from the focus of the laser beam reducing the quality of the optical trap.

### 2.1.4 Transfer of angular momentum

The third group, explored here, relies on the transfer of angular momentum, that is intrinsic in the light beam, to the object. Light can have both Orbital Angular Momentum (OAM) and Spin Angular Momentum (SAM). Any absorbing particle in a beam with high OAM, such as a Laguerre-Gaussian beam, will have a torque exerted on it due to the transfer of OAM. A birefringent particle in a circularly or elliptically polarised beam will also have a torque exerted on it from SAM. When light passes through a birefringent material, its polarisation state is changed, changing the SAM associated with it. This change of angular momentum results in a torque being exerted on the birefringent particle. If the particle is small enough and suspended in a liquid the

## 2.1. INTRODUCTION

---

particle will rotate. This method has the advantage over OAM that there is no associated absorption to cause heating which is a problem when high powers are used.

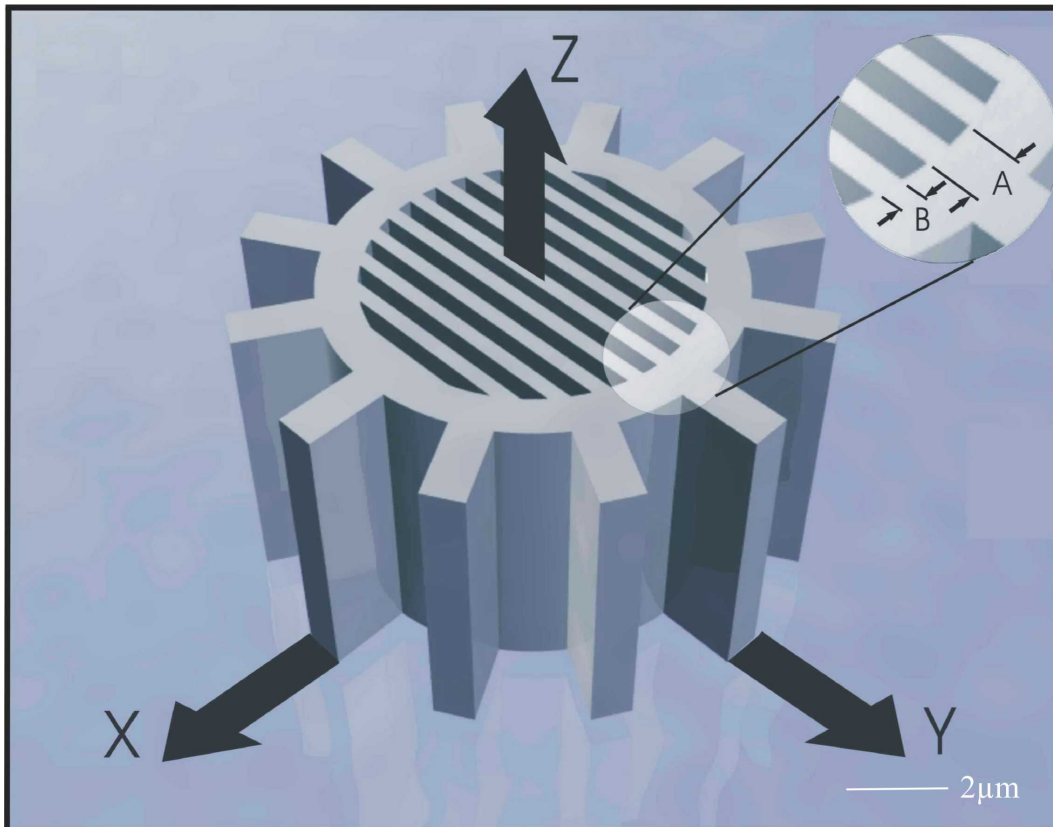


Figure 2.2: A Photonic Crystal MicroGear (PCMG). The one dimensional photonic crystal in the center of the microgear refracts light anisotropically, along and across its slots, creating birefringence. The pitch of the photonic crystal is given by A whilst the fill factor is B/A.

However, most materials are not birefringent and making usefully shaped particles such as microgears out of birefringent materials such as calcite or

## 2.1. INTRODUCTION

---

quartz is not trivial. Birefringent microlenses and microprisms have been realised by creating in plane birefringence in a polyimide. This is achieved with a curing process that aligns rod like structures within the polyimide film, however the birefringence achieved is only  $\Delta n = 0.05$  [7]. Another solution to the problem is to transfer angular momentum from light to an arbitrary shaped birefringent particle which is close to the microgear. The rotating particle causes fluid flow that rotates the microgear [8]. A more elegant approach however, is to use form birefringence. Here we create slots in the material that are roughly the same size as the wavelength of light (a one dimensional Photonic Crystal (PC), see figure 2.2). The light propagates preferentially along the slots to across them creating an artificial birefringence called form birefringence. This allows the use of any material convenient for microfabrication and also can give a birefringence of up to  $\Delta n_{eff} = 0.5$ , higher than found in naturally birefringent materials such as calcite  $\Delta n = 0.16$  (see section 1.2). In this chapter I will show the modeling, fabrication and testing of form birefringent microgears. I will discuss their applications, ways to maximise the interaction between light and the microgear and their limitations. This work has been published [15].

## 2.2. SIMULATION

---

### 2.2 Simulation

#### 2.2.1 FIMMwave simulations

The magnitude of the birefringence was modeled using a vector mode solver (FIMMWAVE, Photon Design). This located the Fundamental Transverse Electric (FTE) and Fundamental Transverse Magnetic (FTM) modes of the 1D photonic Crystal lattice. FTE was defined as having the polarisation aligned with the slots and FTM as having polarisation across the slots. The difference between the effective refractive indices of the two modes is taken to be the birefringence  $\Delta n_{eff}$ . Figure 2.3 shows simulated FTE and FTM modes. Here the slots run horizontally and it is clear that the FTM mode (a) is more evenly spread across the slots, whereas, the FTE mode (b) is better confined. The confinement is in the higher refractive index parts of the slots, the microgear material rather than the medium they are suspended in, making the FTE mode see a higher  $n_{eff}$ .

The magnitude of this difference in refractive index, the birefringence, was modeled for different pitches and fill factors and is shown in figure 2.4. This shows the birefringence increases with pitch and for each pitch there is a maximum fill factor. However this maximum fill factor is different for different pitches. These models are for SU-8, refractive index 1.56, and water, refractive index 1.33 (all refractive indices are for wavelength 1070nm as this is the wavelength used in the experimental section). The modeling shows that the maximum birefringence that can be achieved, without using a pitch greater than  $2\mu\text{m}$ , is 0.022.

## 2.2. SIMULATION

---

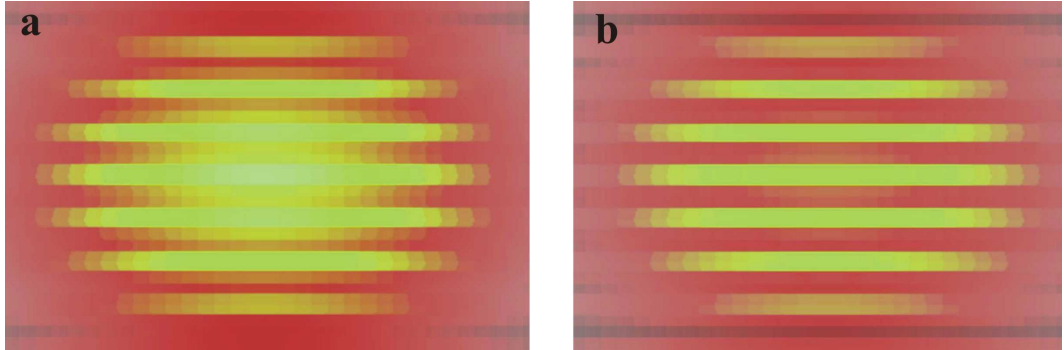


Figure 2.3: Simulated form birefringence of a microgear. The slots in the center of the microgears are simulated as a one dimensional photonic crystal lattice. The Fundamental Transverse Magnetic (FTM, a) and Fundamental Transverse Electric (FTE, b) modes are located. This plot shows the magnitude of the electrical field with yellow showing areas of high field.

The exchange of momentum between the light and the microgear due to the birefringence exerts a torque,  $\tau$ , on the microgear given by [10];

$$\tau \propto E_o^2[1 - \cos(kd\Delta n_{eff})] \quad (2.1)$$

Where  $E_o$  is the electric field,  $k$  is the wave vector,  $d$  is the microgear's thickness and  $\Delta n_{eff}$  is the birefringence. From this it can be seen the maximum torque will be achieved at  $d\Delta n_{eff} = \lambda/2$ , when the particle acts as a half wave plate. Circularly polarised light has SAM of  $\pm\hbar$  per photon. If passed through a half wave plate the light will be changed into circularly polarised light of the other handedness giving  $2\hbar$  angular momentum to the microgear per photon. As our value for  $d\Delta n_{eff}$  is less than a tenth of the value for a half wave plate we can increase the force by either increasing the thickness or increasing the birefringence.

## 2.2. SIMULATION

---

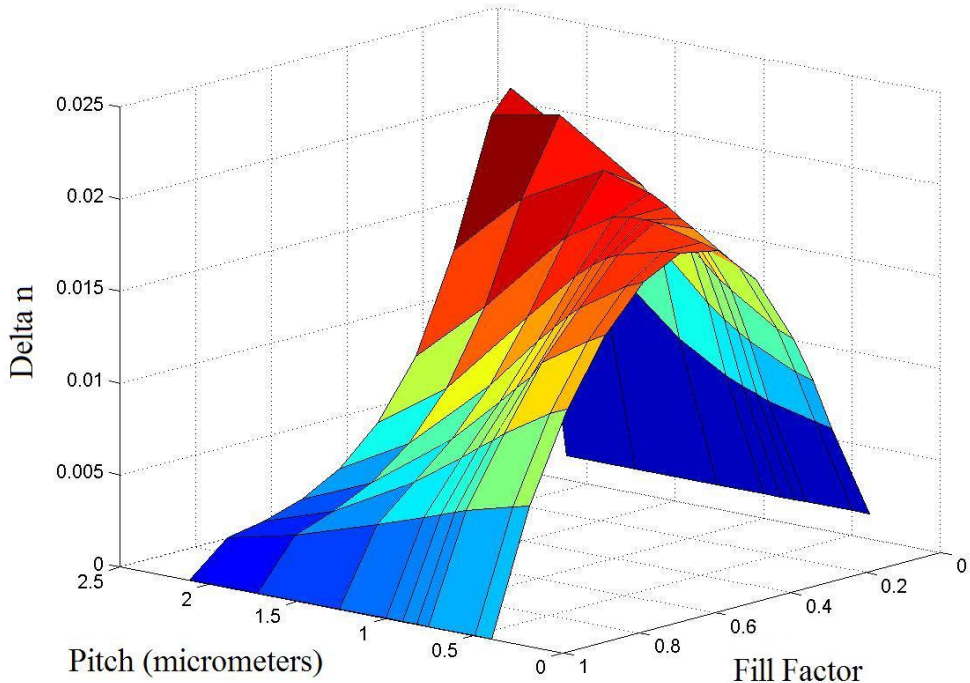


Figure 2.4: Form birefringence as a function of pitch and fill factor, simulated for Su-8 in water. As the pitch increases so does the maximum form birefringence. The optimum fill factor changes with pitch.

Simulations were also carried out for the possibility of increasing the refractive index of the microgear material. If the microgears could be made from a high refractive index polymer such as Optindex A14 (refractive index 1.95, Brewer Science) the models show that the birefringence could be as high as 0.14. This is close to the value for calcite (0.16) which is regarded as having a very high birefringence and as such is often used to show rotation in optical tweezers. If the microgears could be made from a semiconductor such as silicon (refractive index 3.5) the modeled birefringence is as high as 0.5. This would mean a particle could be spun much more effectively than using

## **2.2. SIMULATION**

---

a naturally birefringent material. The higher refractive index has a drawback in that the higher scattering forces caused by higher reflections will hinder the optical trapping. It may be possible to use an antireflection coating to reduce these reflections and allow the gear to be tweezed.

### **2.3. OPTICAL SETUP**

---

## **2.3 Optical Setup**

The sample cell containing the microgears was placed into a simple optical tweezing setup shown in figure 2.5. The sample cell consisted of a microscope slide and a cover slip separated by a vinyl spacer. The laser used was an IPG Photonics fibre laser operating at 1070nm with a max power of 10W. This was focused down to a spot  $5\mu\text{m}$  in diameter. Laser powers up to one Watt were used as it was found that at higher powers the radiation pressure (see section 1.2) pushed the microgears against the microscope slide causing friction that hindered the microgears rotation.

The microgears are optically trapped in two dimensions allowing them to be moved around horizontally in the sample cell and then rotated in one of two ways. Either using circularly polarised light (use the Quarter Wave Plate (QWP)), or with linearly polarised light that has had its direction of polarisation rotated (by rotating the Half Wave Plate (HWP) in a rotating mount). The rotation of the microgears was observed on a CCD camera and videos were recorded for analysis.

The magnitude of the birefringence of the microgears can be measured by observing the transmitted light [9]. As circularly polarised light passes through the microgear its polarisation state is altered due to the birefringence of the microgear. By placing a polarising beam splitter after the microgear sample we can observe this change in polarisation state as a change in intensity measured by the photodiode.

## 2.3. OPTICAL SETUP

---

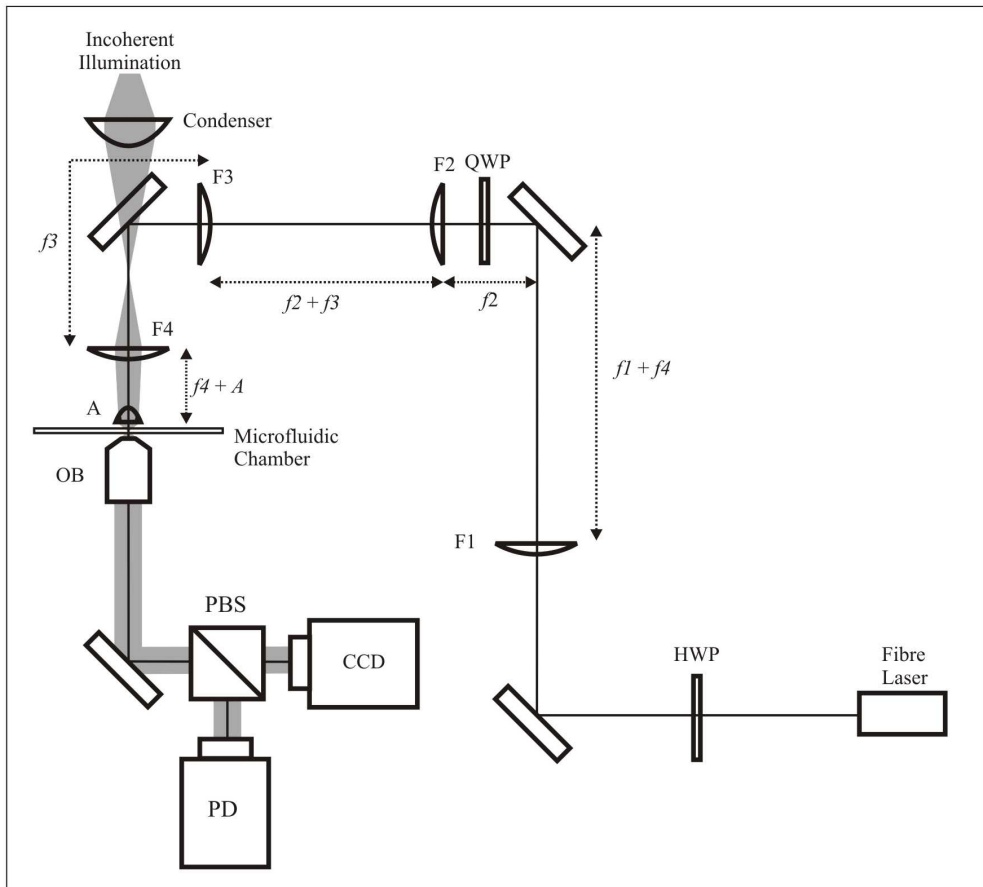


Figure 2.5: Optical Setup. HWP = Half Wave Plate, QWP = Quarter Wave Plate, F1-F4 = planar convex lenses with focal distances  $f_1-f_4$ . A= Aspheric Lens ( $NA=0.68$ , effective focal length= 2.75mm, clear aperture= 4mm), OB= Microscope Objective ( $NA= 0.42$ ,  $f=20\text{mm}$ ), PBS= Polarising Beam Splitter, PD= Photodiode.

## 2.4. FABRICATION

---

### 2.4 Fabrication

#### 2.4.1 Microfabrication techniques

Microgears have been created for optical manipulation in a number of different ways. The most popular fabrication method is two photon polymerization [3][4]. Here light is focused tightly into a photocurable resin which absorbs two photons in a single quantum event polymerizing the resin into a hard shape which is defined by moving the focus of the beam within the resin. As the two-photon absorption is proportional to the square of the light intensity the area of polymerization is small compared to the optical spot size allowing the fabrication of features down to 100s of nm.

Other methods include photolithographic liftoff [8], conventional MEMS fabrication techniques [5] and commercial MEMS fabrication [6]. Microcomponents have been made from a birefringent polyimide film by electron beam lithography and reactive ion etching [7]. Soft lithography has also been used to create PDMS microgears [11] which could have been optically driven but were magnetically driven. Which fabrication method is most suitable depends primarily on the material that the microgears are to be made from and the minimum feature size of the microgears.

Silicon was chosen as the microgear material as it has a high refractive index which gives a high refractive index difference between the microgear and the medium it is put into. This gives a high optical gradient force (see section 1.7) and hence a strong interaction with an optical pattern. The first microgears were designed to have circles of material in their centers that could be grabbed by this force and rotated by rotation of the optical pattern (see figure 2.1).

Optical tweezing generates forces typically in the pN range which makes this technique useful for moving picking up or rotating particles in the mi-

## 2.4. FABRICATION

---

crometer size range. We chose to use two methods to pattern material on these length scales, photolithography and electron beam lithography. These techniques have the advantage of being widely available and well understood due to their use in the construction of microprocessors. Two photon polymerization has the advantage of being able to easily construct 3D features but is not compatible with mass fabrication so is unlikely to become as popular. Features down to two micrometers can be made using photolithography whilst the e-beam lithography system at St Andrews can go down to 16nm but has the drawback of being more technologically demanding. To construct a gear that could be moved using optical tweezers it is desirable to make features that are smaller than two micrometers hence it is necessary to use electron beam lithography whilst photolithography could be used to construct channels for the microgears to spin in. For an explanation of photolithography see section 3.2.1.

### 2.4.1.1 Electron Beam Lithography (EBL)

Electron beam lithography (EBL) involves the exposure of a thin layer of polymer, the resist, to a focused beam of electrons. The resist is chosen and prepared so that the electron beam effects its solubility. In a positive resist the polymer chains in the exposed areas are cut by the beam making it more soluble. When the sample is placed in a developer these areas are washed away. In a negative resist the exposure cross-links polymer chains so that they are less soluble and when it is placed in developer the unexposed areas are washed away (see figure 2.6).

In comparison to other forms of resist patterning EBL is a high resolution and flexible approach with feature sizes down to 16nm possible in any 2D pattern [12]. EBL suffers from being comparatively slow with each feature

## 2.4. FABRICATION

---

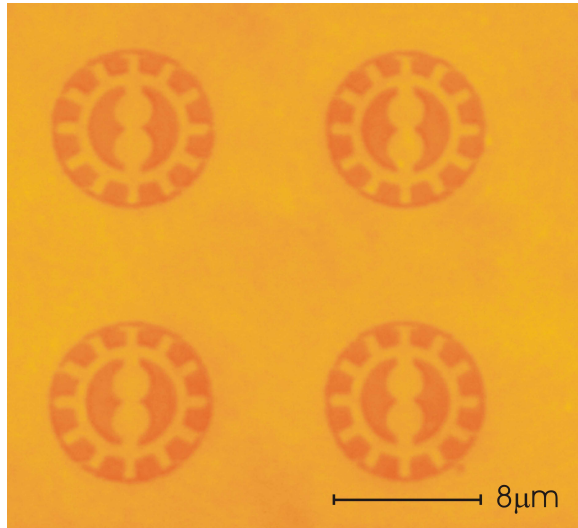


Figure 2.6: A pattern of microgears that has been written using Electron Beam Lithography (EBL). Here PMMA, a positive resist, has been used so the areas around the microgears have been exposed and hence removed when the sample was developed.

being written in series, but this also gives it flexibility allowing the design to be changed easily giving fast prototyping. The high resolution also comes at a high financial price with the high precision system being expensive to purchase and to maintain due to its complexity.

The major components of an EBL system consist of an electron gun, a column which shapes the electron beam, a high precision stage to move the sample, a vacuum system and the necessary control electronics including a pattern generator. The system at St Andrews is a conversion of a Scanning Electron Microscope (SEM, Leo Gemini 1530) into an ELB system using a Raith Elphy Plus pattern generator. For a thorough explanation of e-beam lithography see [13]. More detail and the most relevant parameters to each particular process are described in the recipes below (for exposure parameters

## **2.4. FABRICATION**

---

see section 2.4.3.2, for electrons scattering and the proximity effect see section 2.4.4).

### **2.4.1.2 Reactive Ion Etching**

Transfer of the pattern from the resist into the microgear material was performed by Reactive Ion Etching (RIE) in a home built RIE setup. The process of RIE involves exposing areas of material that are to be removed to a plasma of a gas that will chemically react with this material forming a volatile gas. Ions are accelerated towards the sample to make the etching anisotropic, giving vertical side walls. Areas covered by the resist are not affected by the plasma so remain. The resist will be eroded by the plasma but by choosing the chemistry wisely a combination of gas, material and resist can be found to give good selectivity (the selectivity is defined as the thickness of material removed divided by the thickness of resist removed). The key parameters in RIE are the power used and the pressure the etching is carried out at. How these parameters affect the different etching and the different recipes used will be discussed in the relevant chapters.

## **2.4.2 Silicon microgears**

### **2.4.2.1 Using PMMA as an etch mask**

A Silicon On Insulator (SOI) wafer consists of a substrate of silicon covered in a one micrometer thick layer of silicon dioxide, the insulator, with a thin layer of silicon on top. If a resist is spun onto this and patterned with EBL the pattern can be transferred into the top layer of silicon by selective RIE using PMMA as an etch mask. If the silicon dioxide layer is isotropically etched away the microgears can be released ready for optical manipulation. This patterning

## 2.4. FABRICATION

---

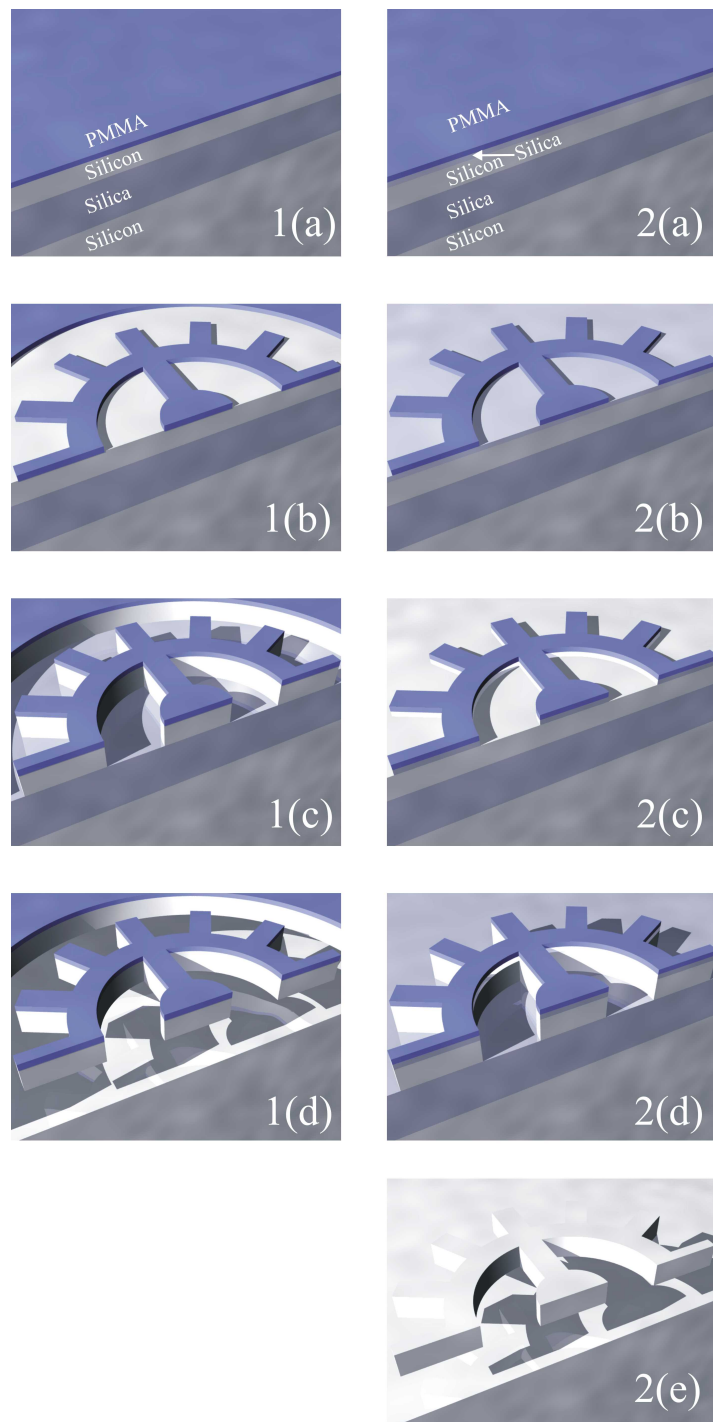


Figure 2.7: Comparison of a one (1) and two (2) mask process for making a silicon microgear.

## 2.4. FABRICATION

---

and lifting off technique is similar to a previously used microgear fabrication technique [6]. For this process to work a thick enough layer of resist is needed so that the silicon can be etched away before the resist. If this is not possible then a two mask process is required where the pattern is transferred from the resist into a hard mask that is then used as a mask to etch the microgear material.

The two processes are shown in figure 2.7. First PMMA is spun on (1(a), 2(a)) and patterned by EBL (1(b), 2(b)). The pattern is then transferred into the silicon in a one step process 1(c) or into a hard mask for a two step process 2(c). This hard mask is then used to pattern the silicon 2(d) before the microgear is released (1(d), 2(e)).

A sample of microgears patterned into 130nm thick PMMA on SOI was obtained from the University of Glasgow. The silicon on top of the SOI was 330nm thick so a selectivity of three was required to be able to use the PMMA as an etch mask. A series of experiments were conducted to find the optimum conditions for high selectivity (see appendix 2.7.1). It was found that the maximum selectivity achievable was 1.2 so it was necessary to go to a two step mask method using PMMA and silica as masks.

### 2.4.2.2 Using silica as an etch mask

The etching of the resist is due more to physical bombardment of ions from the plasma than it is due to actual chemical etching. Thus to etch deeper into the silicon a harder mask that will not be effected by either the physical or chemical etching is needed. Using silica as an etch mask, a much higher selectivity can be achieved. Although silica can be etched using fluorine chemistry (the fluorine in  $CHF_3$  reacts with the  $Si$  in  $SiO_2$  to form the volatile gas  $SiF_4$ ) it etches much less due to the physical ionic bombardment. Thus if the pattern can be

## 2.4. FABRICATION

---

transferred from PMMA into silica it can then be transferred from the silica into the silicon (see figure 2.7). SOI coated with 100nm of silica was obtained and 130nm of PMMA was spun on and patterned by EBL. The pattern was transferred into the silica using  $CHF_3$  at 0.03 mbarr, 33W with the gas ring at position 30mm for 15 minutes. This removed almost all of the resist giving a selectivity of 1 but as the layer of silica is thinner than the resist, this is all that is needed. The pattern was then transferred into the silicon with  $SF_6$  at 0.03 mbarr, 10W with the gas ring at position 30mm for 4 minutes. The silica on top and underneath the silicon layer was then removed by wet chemical etching with Hydrofluoric Acid (HF), freeing the microgears (see figures 2.8, 2.9). The sample was then washed in water and a drop of water containing free microgears was placed onto a microscope slide for manipulation with an optical trap.

## 2.4. FABRICATION

---

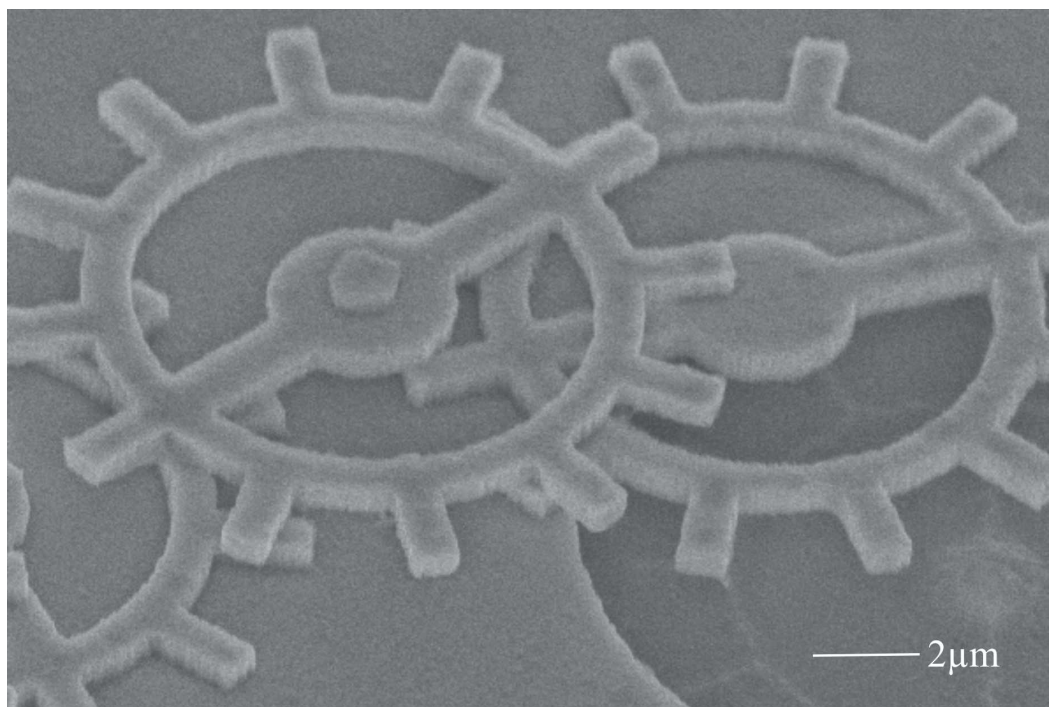


Figure 2.8: Silicon microgears. The microgear pattern was created in resist by e-beam lithography and the pattern was transferred into the silicon by Reactive Ion Etching. The silica release layer was then wet etched away freeing the microgears.

## 2.4. FABRICATION

---

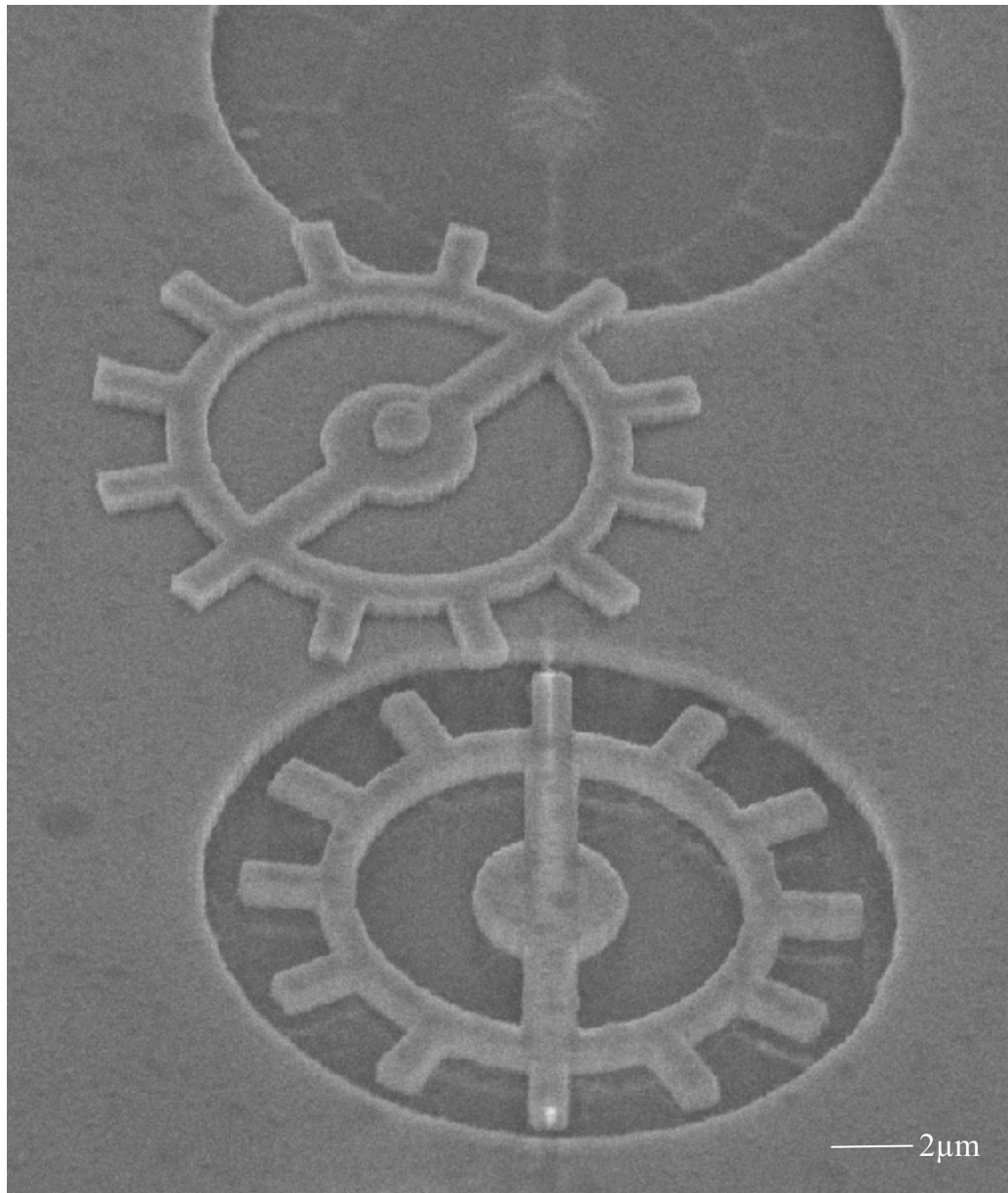


Figure 2.9: Here one microgear has become free while another below it is still attached to the substrate. The acid etches isotropically but has less time to etch the material under the microgear that is uncovered. This leaves an outline of the microgear in the silica where the silicon microgear has been. There is also a small amount of material left in the center of the circles on the microgear.

## **2.4. FABRICATION**

---

When the microgears were put into an optical trapping setup they were not attracted to the light as they had been designed to, but were repelled by the areas of high intensity. This can be seen in figure 2.10 which is a series of images taken from a video of a silicon microgear.

Here the microgear is spun by an asymmetrical rotating light pattern. The microgear does not stay central however but tries to escape the light as it rotates. It is only kept within the light beam as most of the light goes through the holes in the center of the microgear so it can not escape. The repulsion was due to the scattering forces being stronger than the optical gradient force (see section 2.1.2). Both of these forces are dependant on the material being trapped and the objects shape. As it was desired to create an object in the shape of a microgear a different material was required. To see how different materials tweeze differently see section 2.6.1.

## 2.4. FABRICATION

---

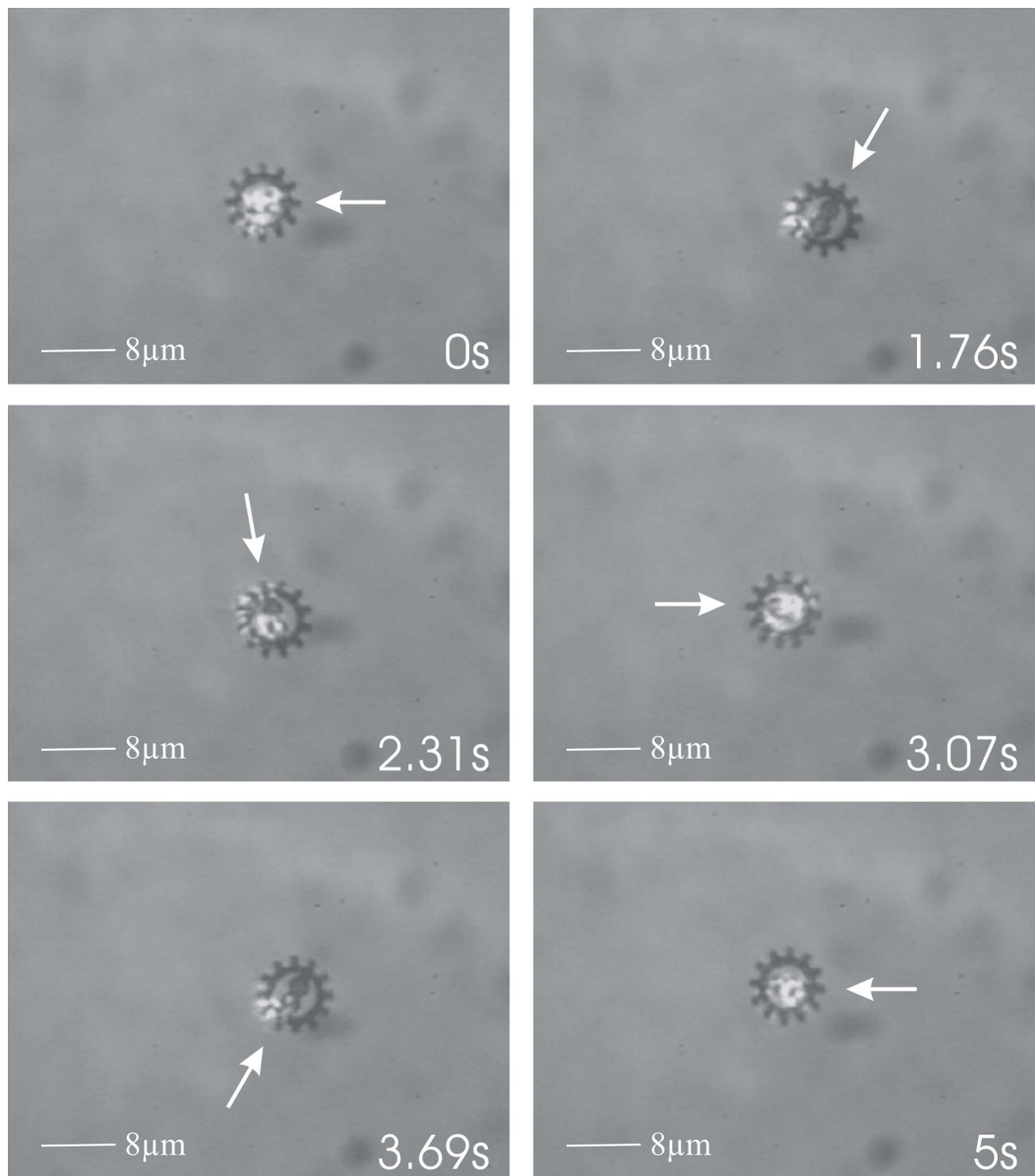


Figure 2.10: These images are taken from a video of a silicon microgear being rotated by an asymmetrical rotating light pattern. The microgear takes 5 seconds to rotate 360 degrees. The beam can be seen as a bright spot.

## 2.4. FABRICATION

---

### 2.4.3 Polymer microgears

SU8 photoresist (2000.5 and 2050, MicroChem) was chosen to be used as a microgear material due to its refractive index of 1.56. This index reduces the scattering forces making it more likely for the microgear to be attracted to an optical trap. SU8 is easily processed, it can be spun onto a substrate into nearly any thickness desirable and patterned by either photolithography or EBL.

#### 2.4.3.1 Direct Writing

The simplest way to create microgears in SU-8 is to directly write into the SU-8 layer with EBL. The process is shown in figure 2.11 with the substrate being spin coated in release layer then SU-8 (figure 2.11, 1(a)), the SU-8 being patterned by EBL (figure 2.11, 1(b)) and then the release layer being removed (figure 2.11, 1(c)). SU-8 acts as a negative resist for EBL so that the areas of the microgear that we want to remain are exposed to the electron beam. A silicon substrate was coated in a release layer (SU-8 release layer, MicroChem, spun at 3000rpm for 60s then baked on a hot plate at 200°C for 60s) then in a 350nm layer of SU8 (SU-8 2000.5 spun at 5000rpm for 60s, hot plate at 100°C for 60s) and patterned by EBL. After the exposure the resist needs a further bake, 30s at 100°C, to ensure full polymerization. The resist was developed in EC solvent (MicroChem) for 5s. In order to get the desired pattern with EBL the key parameter is the dose that the resist receives. In order to know how to control this parameter it is necessary to examine how the exposure works.

## 2.4. FABRICATION

---

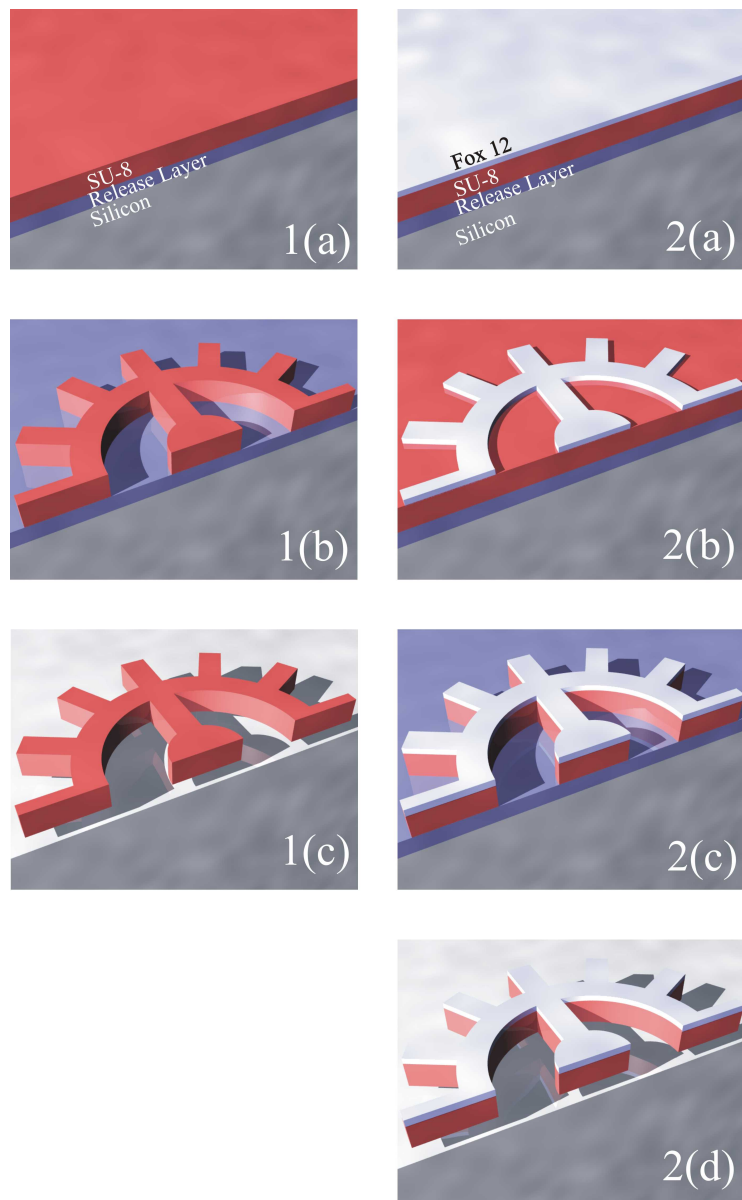


Figure 2.11: Comparison of a directly writing Su-8 (1) and using FOX12 to make a mask which can then be used to etch the pattern into the SU-8 (2).

## 2.4. FABRICATION

---

### 2.4.3.2 EBL exposure parameters

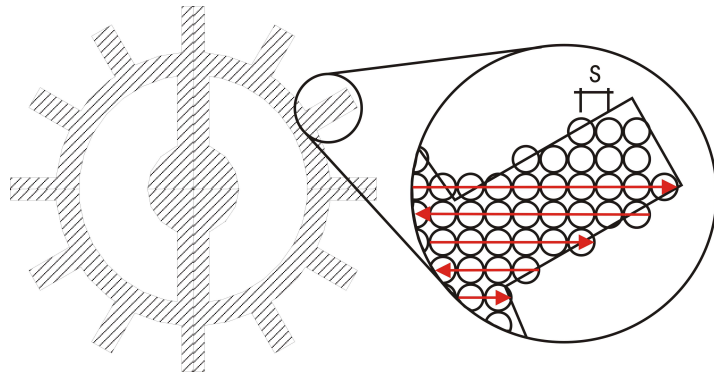


Figure 2.12: EBL exposure. This figure shows how the beam in the EBL system moves. It follows the red line in a vector scan stopping at points separated by the area step size,  $s$ .

The dose is how many electrons hit the resist per unit area measured in  $\mu As/cm^2$ . Usually a negative resist is used and the dose required to break enough of the polymer chains making the resist soluble is called the clearing dose. Writing in SU-8 we expose the areas we wish to keep by cross linking the polymer chains. The beam moves along the desired pattern as shown in figure 2.12 in what is called a vector scan. It moves a distance defined by the area step size and waits for a time called the dwell time. The dose is then given by;

$$Dose = \frac{I_{beam} T_{dwell}}{s^2} \quad (2.2)$$

Where  $I_{beam}$  is the current of the electron beam,  $T_{dwell}$  is the dwell time and  $s$  is the area step size. The electron gun gives a constant beam current for a particular acceleration voltage (set at 20 or 30kV) and is in the nA range. However it can be changed by placing an aperture into the beam. Usually a 30 micrometer diameter aperture is used but SU-8 is a very fast resist (it

## 2.4. FABRICATION

---

needs very little dose to expose it) so a 10 micrometer diameter aperture was used instead. There is a limit to the minimum dwell time, corresponding to 6 MHz, that the system can use. This means for a given area step size there is a minimum dose that can be given. To decrease the dose further a larger area step size must be used. It is clear from figure 2.12 a small area step size is desired for small features to give a smooth edge to the pattern. Although the area step size was increased from 16 to 20nm a low enough dose could not be given to the resist to prevent overexposure. The best microgears that could be fabricated are shown in figure 2.13. This is an optical photograph taken after the microgears had been released from the substrate by dissolving the SU-8 release layer in N-methylpyrrolidone (NMP, Aldrich). Although it would have been possible to try other ways to decrease the dose given by the EBL system by changing down to the smallest aperture (7.5 micrometers diameter) or increasing the acceleration voltage so that more of the electrons go through the resist without interacting with it, I decided instead to go to a two step masking approach as this was more likely to be successful.

## 2.4. FABRICATION

---

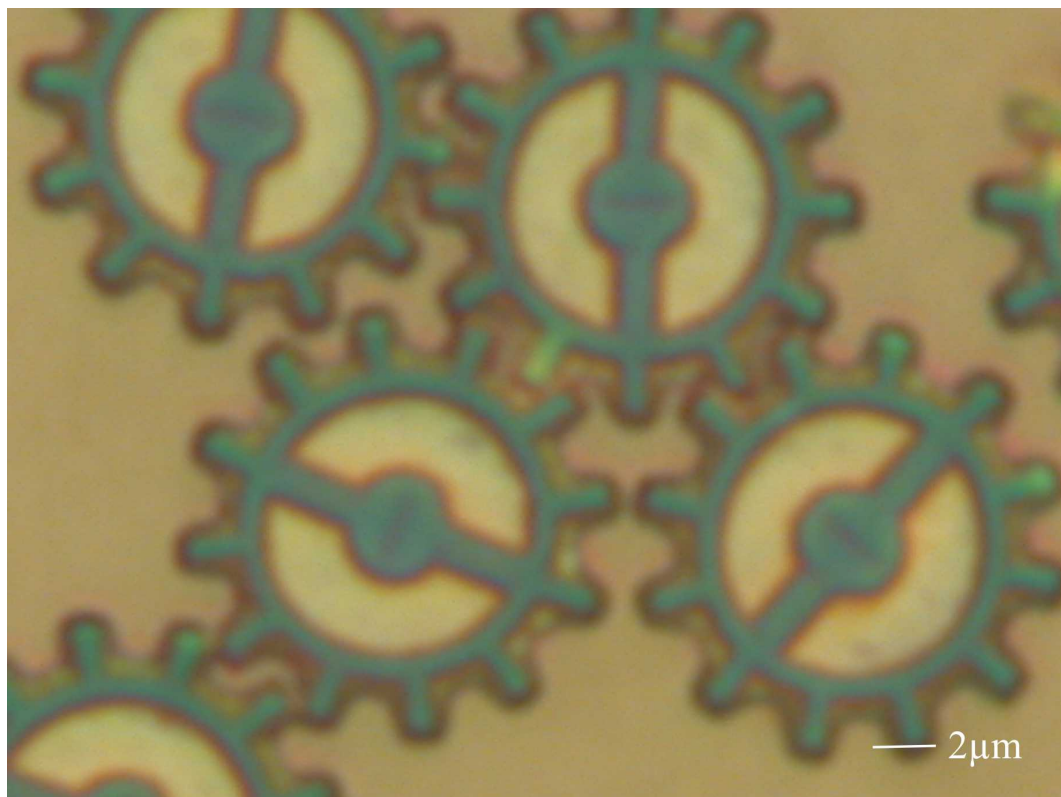


Figure 2.13: SU8 microgears. The best microgears fabricated by exposing the SU8 with EBL were slightly overexposed. This can be seen by the rounding of features and the presence of material in the areas inside the microgear that should be clear.

## 2.4. FABRICATION

---

### 2.4.3.3 Using FOx-12 as a hard etch mask

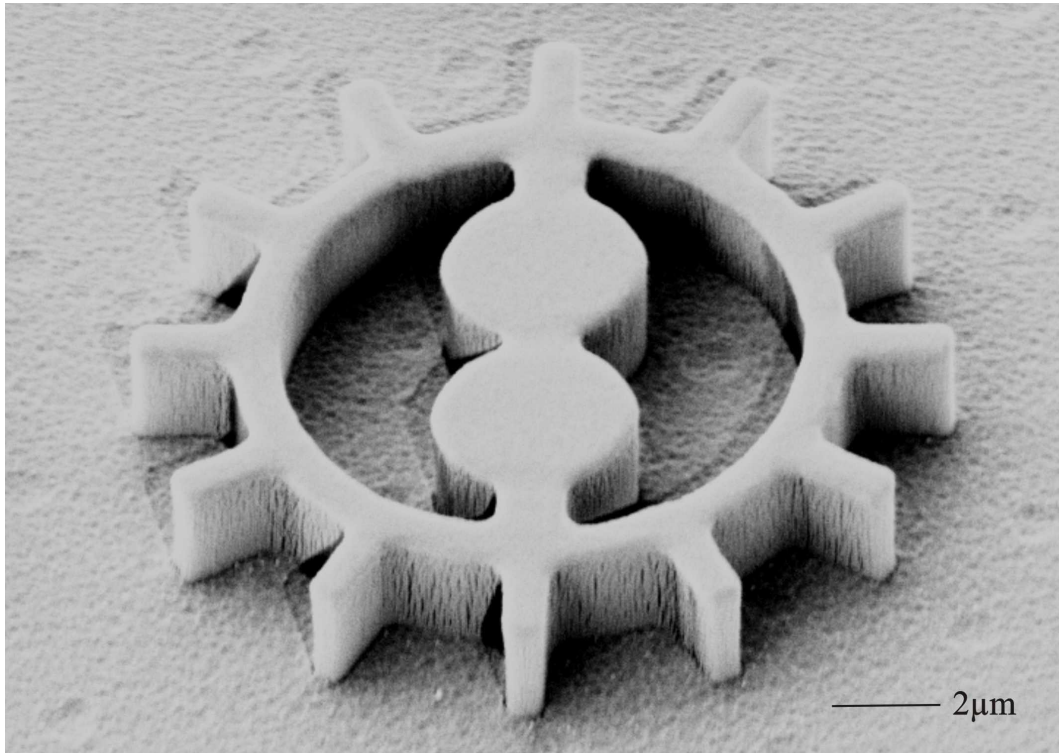


Figure 2.14: An SU8 microgear. Microgears were created that closely resemble the desired design by patterning FOX12 then using this as an etch mask to pattern the SU-8.

Hydrogen Silsesquioxane (FOx-12, Dow Corning, FOx stands for Flowable Oxide) also acts as a negative resist for EBL and as such can be used in a two step masking process (see figure 2.11). This resist takes around one thousand times the dose necessary to expose SU-8 (depending on thickness) and hence is more easily controlled. The FOx-12 is spun onto the previous structure (figure 2.11, 2(a)) then patterned by EBL (figure 2.11, 2(b)) and this is used as an etch mask to pattern the SU-8 (figure 2.11, 2(c)) before the microgear can be released by removing the release layer (figure 2.11, 2(d)). As it was desired to

## 2.4. FABRICATION

---

make the microgear thicker than can be achieved just with SU-8 type 2000.5 a mixture of type 2000.5 and type 2050, that can be spun on between 15 and 100  $\mu\text{m}$  thick, was used. The mixture used was 10:1 2000.5:2050 and it was spun at 1000rpm for 60s to give a  $1\mu\text{m}$  thick layer. It was exposed to UV radiation to cure it and baked at  $100^\circ\text{C}$  60s then  $240^\circ\text{C}$  60s (SU-8 does not need to be baked at this high a temperature to cure it but FOx-12 does and it is good practice to bake lower layers at the same temperature as higher layers so that no solvent is released in subsequent hotter bakes). However the FOx-12 did not spin on into a uniform layer on top of the SU-8, instead it formed droplets as water does on a hydrophobic surface. Various parameters in the treatment of the SU-8 layer were tried such as baking it for longer and exposing it for longer to see if its surface could be changed enough to allow the adhesion of the FOx-12. It was found to be necessary to expose the SU-8 to a oxygen plasma for 30s to roughen the surface before a good film of FOx-12 could be spun on. The spinning parameters used were 5000 rpm for 60s then baked for 2 min at  $100^\circ\text{C}$  then 2 min at  $240^\circ\text{C}$ . The FOx-12 was then patterned by EBL using the an acceleration voltage of 20kV, 30 micrometer diameter aperture, area step size 20nm, area settling time 0.05. It was developed in MF319 (Shipley) for 60s, washed in 10:1 water:MF319 for 15s followed by water for 15s. This creates a hard mask of 60 to 70nm thick that can subsequently be used as an etch mask for the SU-8 underneath using RIE with an oxygen plasma. The etching parameters were oxygen at 0.027 mbarr, power 30W, ring at position 30mm for 3 minutes (for a discussion of how these parameters effect RIE see section 2.7.1). The FOx-12 is very tough against this attack giving a very high selectivity so that SU-8 layers as thick as 2  $\mu\text{m}$  could be processed with 60-70 nm of FOx-12. Using this recipe microgears were produced as shown in figure 2.14.

## 2.4. FABRICATION

---

### 2.4.4 Photonic Crystal MicroGears (PCMG)

A more elegant rotation method would be to use birefringence. As naturally birefringent materials are difficult to pattern we thought of the possibility of creating the birefringence artificially using form birefringence. Here birefringence is created by shaping the centers of the microgears into a series of slots with a period similar to the wavelength of light (a 1D photonic crystal). As the light passes through the slots it sees different refractive indices depending on whether it is polarised along or across the slots (see section 2.2).

Photonic crystals are usually created by etching a lattice of holes into a semiconductor and used amongst other things to guide light via a photonic band gap [14]. For form birefringence we do not use the photonic band gap which is only evident in the horizontal plane of the crystal but instead illuminate the crystal from above akin to a Photonic Crystal Fibre (PCF). When constructing the photonic crystal the fill factor and pitch are critical for this application. The pitch can be chosen and accurately written by EBL but the fill factor can vary with the dose. As writing in FOx-12 was more tolerant to changes in the dose this method was used to create Photonic Crystal Micro-Gears (PCMG).

Process 2 in figure 2.11 was used but even with this more dose tolerant approach the optimal dose for the same pattern changed from run to run (see figure 2.17).

To understand how to increase the consistency it is necessary to look at how the electrons interact with the resist. Figure 2.16 shows a resist layer being exposed to an electron beam. The electrons accelerated by a higher voltage are deflected by a smaller angle exposing a smaller area of resist. They also penetrate deeper into the substrate before being scattered so that less secondary electrons reach the resist. This is important as secondary electrons caused

## 2.4. FABRICATION

---

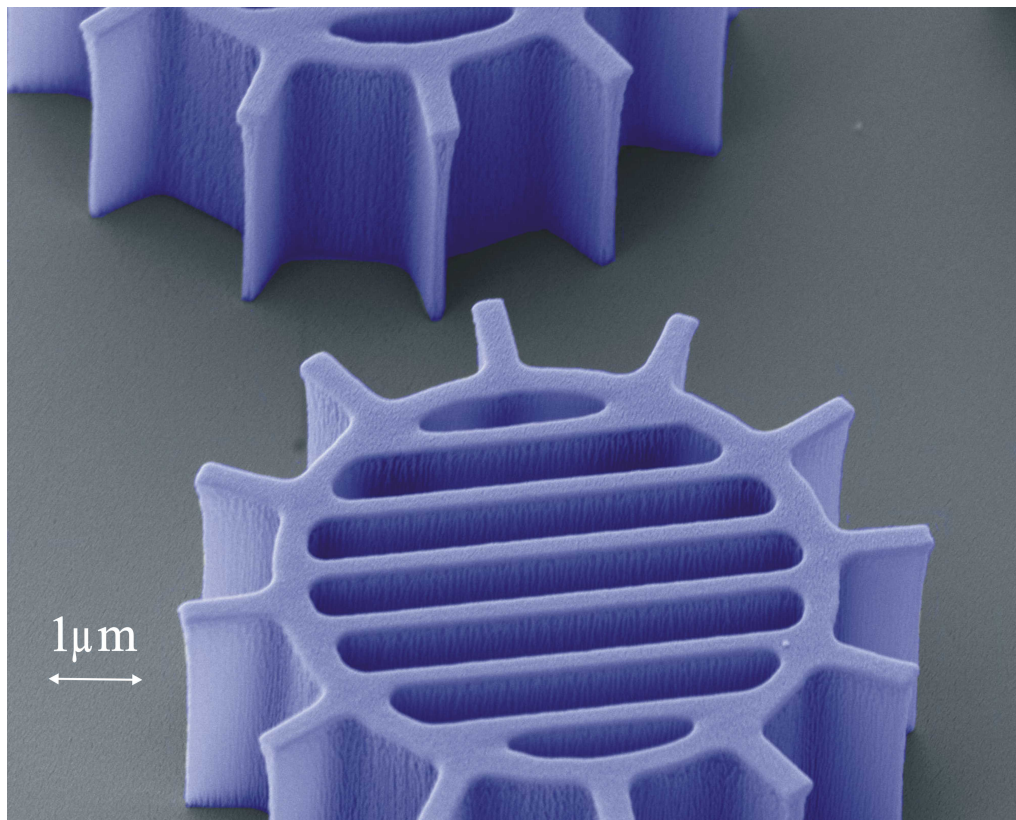


Figure 2.15: This coloured electron micrograph shows a microgear that has been created by patterning FOX12 by EBL then transferring the pattern into the SU-8 by RIE with oxygen.

by forward scattering events are responsible for most of the resists exposure. Thus increasing the acceleration voltage from 20 to 30kV reduces the angle the electrons are scattered at in the resist giving the writing higher resolution. The electrons also penetrate deeper into the substrate before scattering so less back scattered electrons reach the resist again confining the exposure to a smaller area and increasing the dose needed. The acceleration voltage was therefore changed from 20kV to 30kV which resulted in much better dose consistency (see figure 2.18).

## 2.4. FABRICATION

---

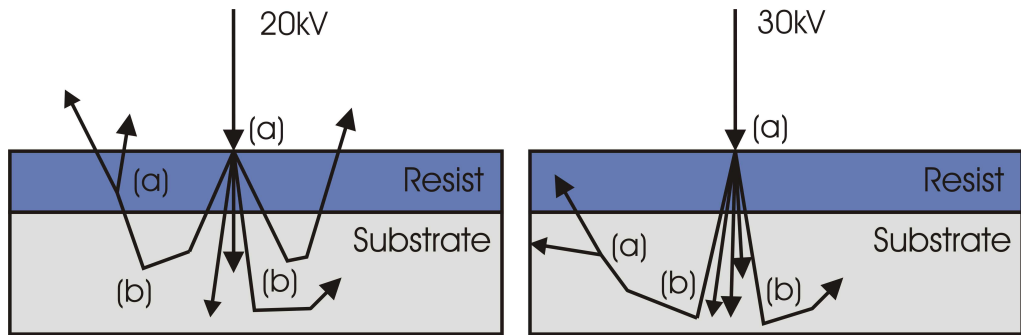


Figure 2.16: This diagram shows a layer of resist being exposed to an electron beam of 20 or 30kV. The electrons represented by arrows are both forward scattered by a small angle (a) and back scattered by a large angle (b).

This improvement in consistency was necessary as many microgears were required to account for the wastage resulting from the process of releasing the microgears and transferring them into the optical set up. After the microgears were released in NMP the sample was washed in water and then repeatedly dipped into a drop of water placed onto a microscope slide causing a few of the microgears to go with the water onto the slide. Since most of the microgears stay near to the substrate after release, only about one percent of the microgears made can be tested. If this process could be made more efficient then a varying dose would not be a problem as enough microgears of different doses could be written in a short enough time. The small variation in dose allowed the creation of microgears good enough to test (see figure 2.15) so these microgears were released from the substrate and tested (see section 2.5).

One way to make this process more efficient would be to fabricate the microgears on a transparent but conductive substrate so that they would not

## 2.4. FABRICATION

---

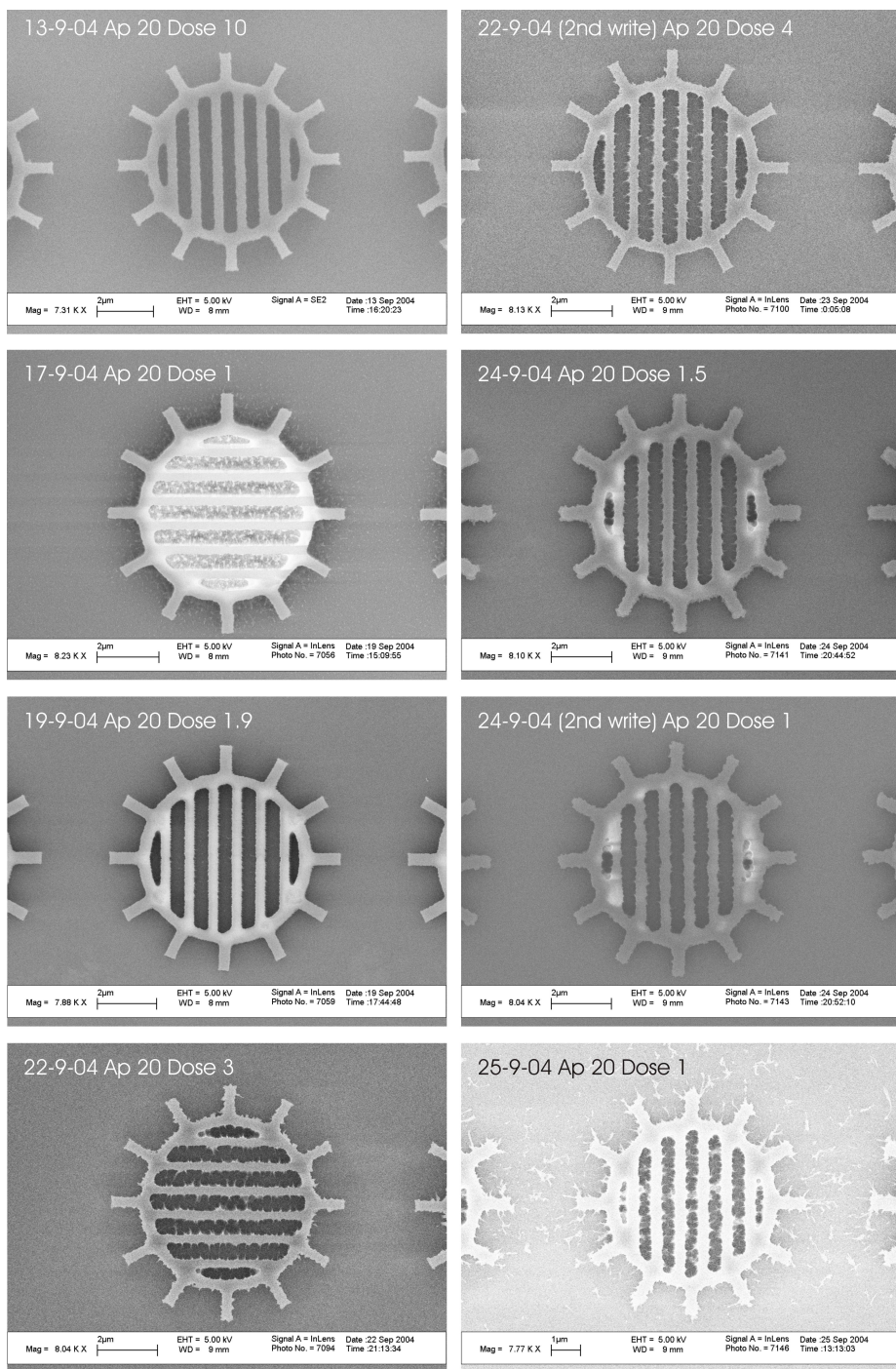


Figure 2.17: Each picture is the optimal dose factor (dose = dose factor x 100) from a dose test using the same pattern. It is clear that the optimal dose varies from one run to the next.

## 2.4. FABRICATION

---

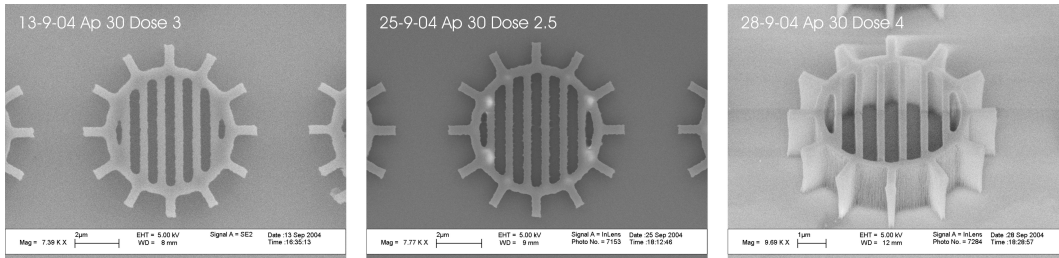


Figure 2.18: Each picture is the optimal dose from a dose test using the same pattern with the aperture changed to 30 micrometers diameter. The dose is now more consistent.

need to be transported onto a microscope slide before testing. Another way to improve the writing may be to fully cure the FOx-12 layer and instead pattern a PMMA layer on top of it and use this as an etch mask to etch through the PMMA layer. This would help if the writing is more consistent in PMMA than FOx-12 but it does have the drawback of adding another step to the fabrication process. Another disadvantage is that PMMA is a positive resist so the area around the microgear would have to be written instead of the microgear increasing write times.

Only one pitch and fill factor of microgear was fabricated and tested with a pitch of 0.8 micrometers and a fill factor of 0.3 giving ribs of 240nm width. To fully test if the birefringence acts as the simulation suggests a range of periods and fill factors should be tested. This would mean producing features close together and hence the proximity effect would become important. The proximity effect is when electrons back scattered from the substrate along with other back scattered electrons from near by exposed areas add up and reach the exposure dose. This can be corrected for by varying the dose across the pattern depending on how close a feature is to other features (see figure 2.19).

## 2.4. FABRICATION

---

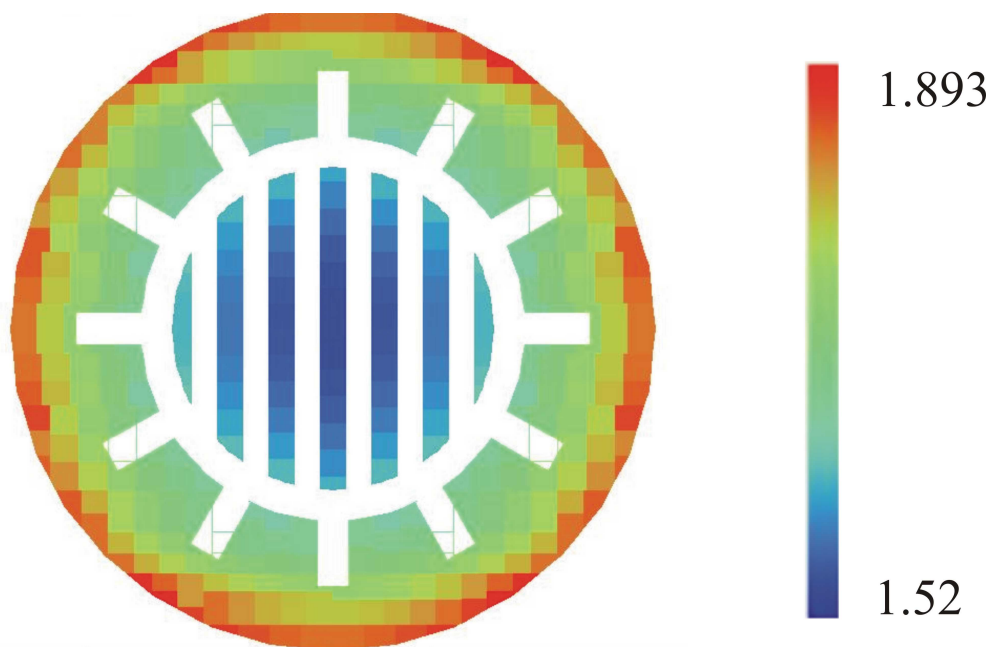


Figure 2.19: This figure shows a microgear pattern for a positive resist that has been corrected for the proximity effect. The variation in relative dose is shown as a variation in colour as shown by the key.

## 2.5. RESULTS

---

### 2.5 Results

#### 2.5.1 Circularly polarised light

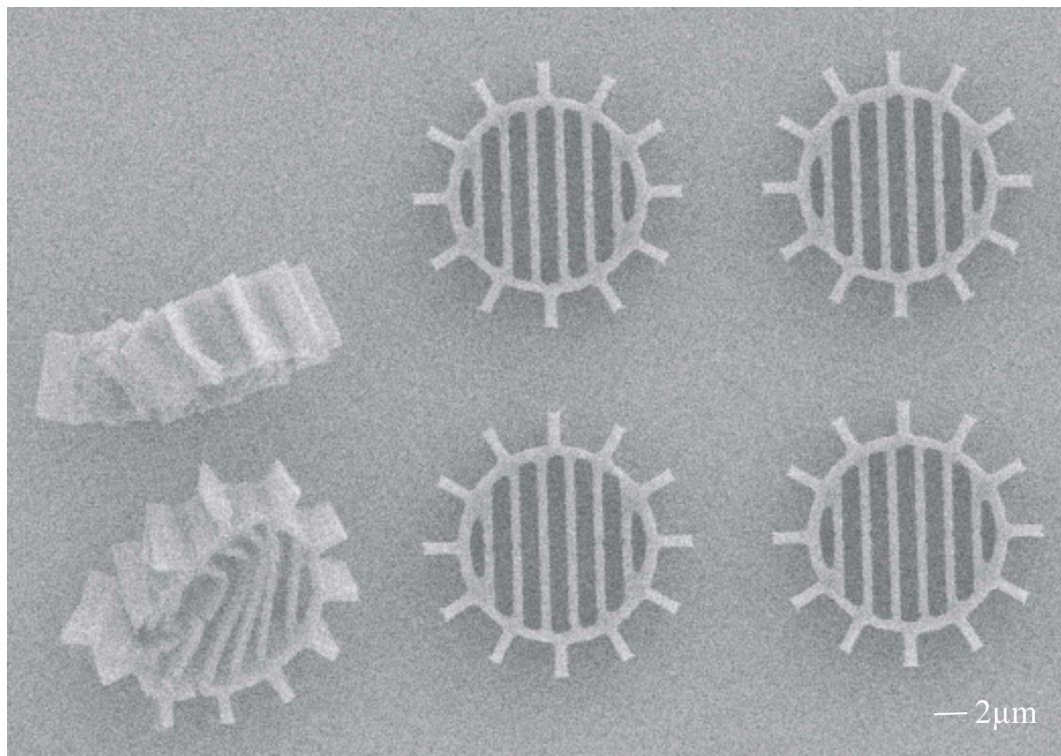


Figure 2.20: These microgears have been damaged by the stylus profiler showing that they hold together well when a force is applied and also shows their depth.

Microgears were fabricated as described and when placed into a surface profiler (Dektak 3) to check the depth of the etching some gears were damaged (see figure 2.20). This showed that the microgears would hold together when force was applied to them. The microgears were then released from the substrate and placed into the optical setup. When illuminated with circularly polarised light they were found to rotate at a constant rate that was proportional to the

## 2.5. RESULTS

---

laser power (figure 2.21,a). When illuminated with a linearly polarised laser beam the microgears aligned themselves with the direction of polarisation and followed the polarisation direction upon rotation. As the half wave plate is rotated in the beam path the polarisation is rotated through twice the angle which means the microgears rotate at twice the frequency of the half wave plate. The maximum rotation rate achievable before the microgears could not follow the direction of polarisation due to frictional forces was proportional to the laser power. At powers of higher than one Watt, the microgears were pressed down onto the surface of the sample cell. This introduces another source of friction and prevents the free rotation of the microgears.

The magnitude of the variation of the transmitted light was compared to the absolute magnitude of the light giving the birefringence (see figure 2.21,b). This was measured as  $\Delta n_{eff} = 0.015 \pm 0.001$  for a microgear with a lattice of pitch  $0.8 \mu\text{m}$  and fill factor 0.3. For the same lattice the simulated birefringence is  $\Delta n_{eff} = 0.018 \pm 0.001$ , which agrees well with the measured result.

As the microgears were trapped in the xy plane, they could be moved close to one another. When two microgears were close to the laser spot they were both attracted to the center of the beam and also both experienced a force trying to rotate them in the same direction. As the interlocking teeth of the gears prevented them both rotating in the same direction the microgear with the strongest interaction with the beam (here the one on the left) forced the other gear to rotate in the opposite direction (see figure 2.22).

## 2.5. RESULTS

---

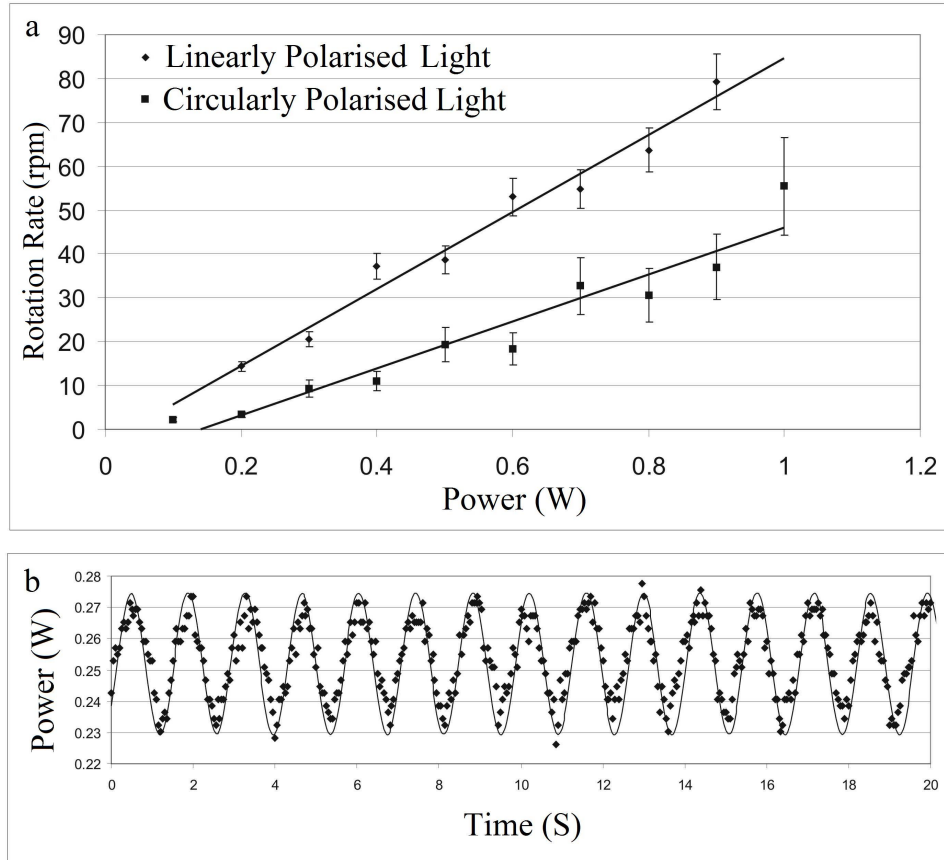


Figure 2.21: Rotation rates. (a) Maximum rotation rates for both circularly and linearly polarised light at increasing powers. The error bars show the deviation of the rotation rate from the average rotation rate after averaging over several revolutions. (b) Light transmitted through the microgears is then passed through a polariser to give a magnitude variation that shows the polarisation variation. The magnitude of the variation gives the magnitude of the birefringence and the rotation rate can be gained from its period.

## 2.5. RESULTS

---

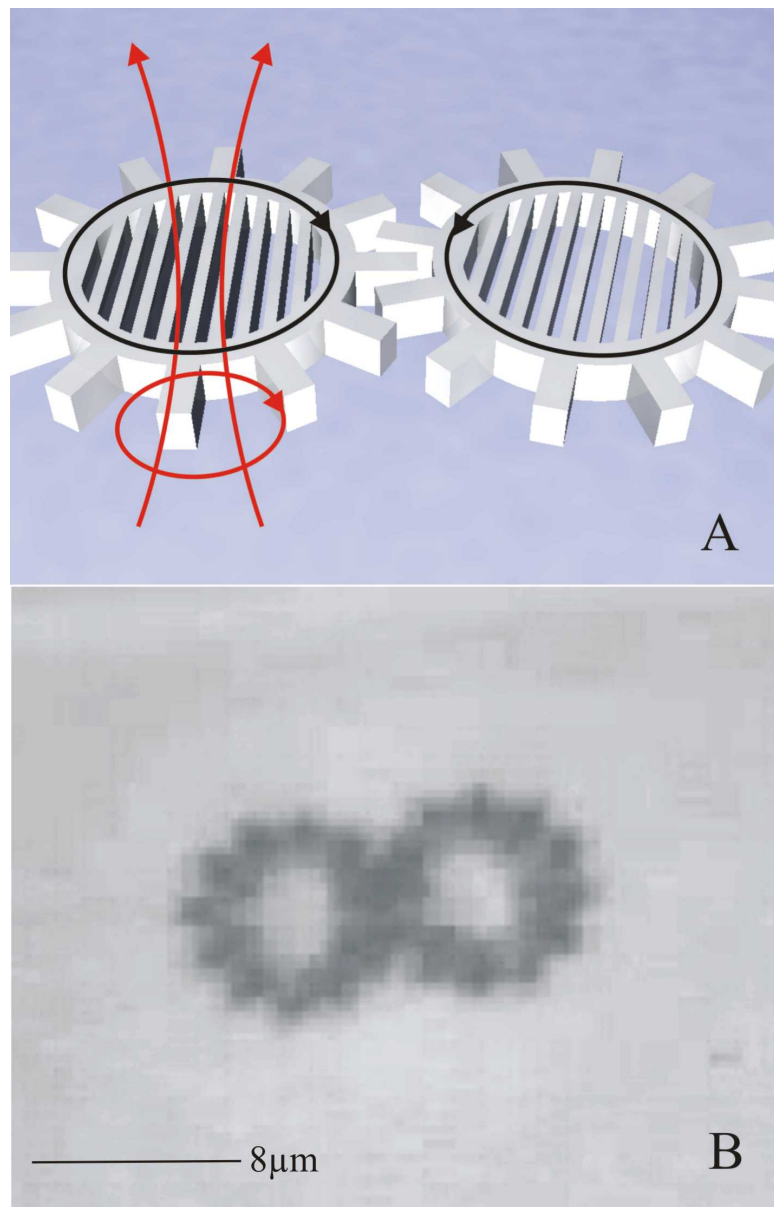


Figure 2.22: A) Diagram of two microgears attracted to the center of the laser beam (red arrows). They both experience a force pushing them to rotate them in the same direction but the interlocking teeth prevent this and the microgear with the strongest interaction, the one closest to the center of the beam, forces the other microgear to rotate in the opposite direction. B) Frame of video of one microgear rotating the other.

## 2.6. SUMMARY AND OUTLOOK

---

# 2.6 Summary and Outlook

We have shown that Spin Angular Momentum (SAM) can be transferred from circularly polarised light to a form birefringent microgear causing the micro-gear to rotate. The microgears readily align themselves with the direction of polarisation of linearly polarised light allowing them to be precisely orientated or rotated by rotating the direction of polarisation of the light. As the shape and birefringence of the microgear can be controlled, they may find applications in microrheology experiments. For applications in the Lab-on-a-Chip area the angular momentum transferred from the photon to the microgear will have to be increased. This could be done by increasing the birefringence (see section 2.6.1) or by making each photon pass through the microgear many times (see section 2.6.2).

## 2.6.1 Increasing the birefringence

From equation 2.1 we can see the optimal condition for getting torque from the light is for the microgears to have  $\Delta n_{eff}d = \frac{\lambda}{2}$ . The fabricated microgears have a  $\Delta n_{eff}d$  of less than one tenth of this value. Figure 2.23 shows how the torque varies with  $\Delta n_{eff}d$  taken from equation 2.1. This shows that although the present  $\Delta n_{eff}d$  is one tenth of the optimal value the torque could be increased by 100 times.  $\Delta n_{eff}d$  can be increased by either increasing the thickness of the microgear, which is technologically difficult as it requires higher aspect ratio etching, or by increasing the birefringence. The birefringence comes from the refractive index difference between the higher refractive index microgear material and the lower refractive index medium. Increasing this refractive index difference increases the possible birefringence with models suggesting that a birefringence of 0.5 (much higher than that even of calcite 0.16) could

## 2.6. SUMMARY AND OUTLOOK

---

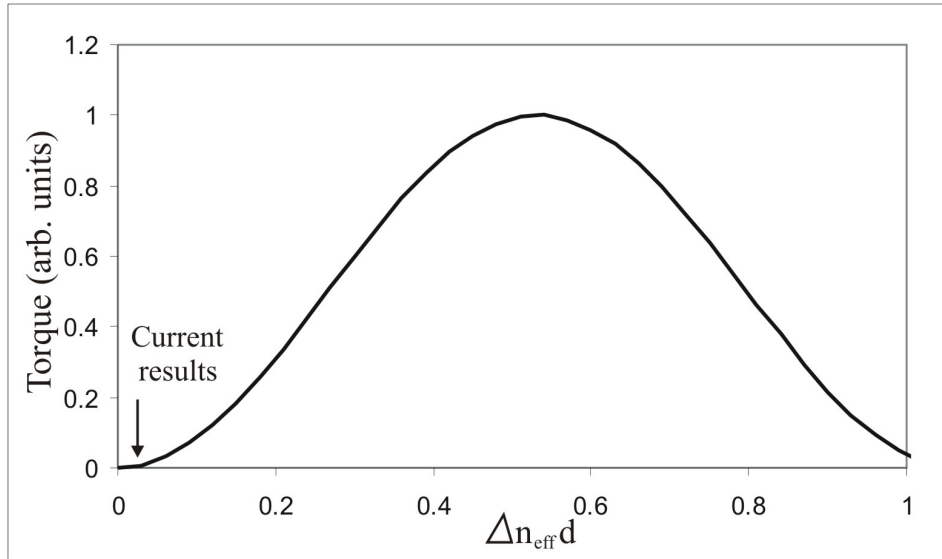


Figure 2.23: The torque on a microgear of different  $\Delta n_{eff} d$ .

be achieved by increasing the refractive index of the microgear material to that of silicon, 3.5. However there is a problem, as increasing the refractive index increases the scattering forces due to reflections so that the particle is no longer held in the 2D optical trap (see section 2.4.2). One possible solution to this problem is using an antireflection layer to reduce the reflections from the silicon.

Figure 2.24 shows the benefits that increasing the refractive index of the microgear material and how an antireflection coating would work. Figure 2.24A shows how the scattering forces due to reflections compare with the optical gradient forces and how they change with refractive index. The scattering and gradient forces are dependent on the geometry of the particle and so have to be experimentally observed. As microgears made from SU-8 were observed to be attracted to the light this tells us the gradient force is larger than the scattering forces for this refractive index. As the gradient force is proportional

## 2.6. SUMMARY AND OUTLOOK

---

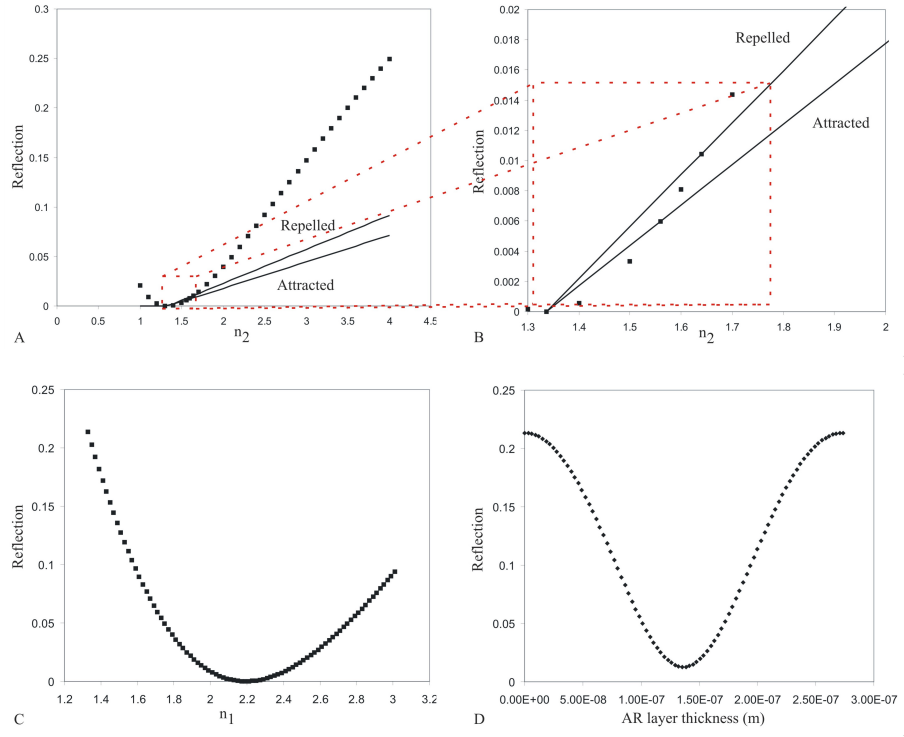


Figure 2.24: A The dotted line represents the reflection from a water/  $n_2$  interface. The solid lines show the amount of reflection that will cause attraction or repulsion. B shows a close up of the refractive indices that will cause attraction. C shows the reflection from a water silicon interface if an AR coating of  $\frac{\lambda}{4}$  thickness and refractive index  $n_1$  is used. D shows the reflection from a OptiNDEX A14 coating of different thicknesses.

to the refractive index of the particle being trapped a line can be plotted through the point at SU-8's refractive index and anything below this will be attracted by the light. Microgears were made from OptiNDEX B38 ( $n=1.64$ ) but were observed to be repelled by the light. This tells us that the scattering forces are larger at this refractive index and a line can be plotted through

## 2.6. SUMMARY AND OUTLOOK

---

this point and anything above this line will be repelled by the light. More experiments would be needed to find if a refractive index between these lines causes attraction or repulsion. The dotted line shows the fresnel reflections from a water  $n_2$  interface. This tells us that unless we reduce the reflections from the silicon microgears from their 20 percent value given by Fresnel's law to below 7.5 percent, they will not be attracted and if we reduce them to less than 6 percent they will be. Figure 2.24B shows a close up section figure 2.24A so that the small ranges of refractive indices that cause attraction above the reflection line can be seen.

Figure 2.24C shows the amount of light that would be reflected from a water silicon interface if an antireflection (AR) coating  $\frac{\lambda}{4}$  thick of refractive index  $n_1$  was used. This was calculated using the fresnel reflection formula and shows that to get zero reflection an AR coating of refractive index 2.2 should be used. It also shows that if OptiNDEX A14 was used (refractive index 1.95) a reflection of just 1.4 percent could be achieved.

Figure 2.24D shows how much reflection would be given from an OptiNDEX A14 AR coating of various thickness. Again it is calculated using the Fresnel reflection formula and tells us how tolerant the AR coating is to thickness variation. It shows us that if the coating is between 100 and 175 nm the reflections will be less than 6 percent. This should be achievable by a spin coating process.

### 2.6.2 Multiple pass systems

To increase the torque on the microgears per incident photon they could be placed into a cavity that forces each photon to travel through the microgear many times. For this to work, the polarisation state of the light has to be carefully controlled with wave plates that cause a  $3\pi/4$  phase change above

## 2.6. SUMMARY AND OUTLOOK

---

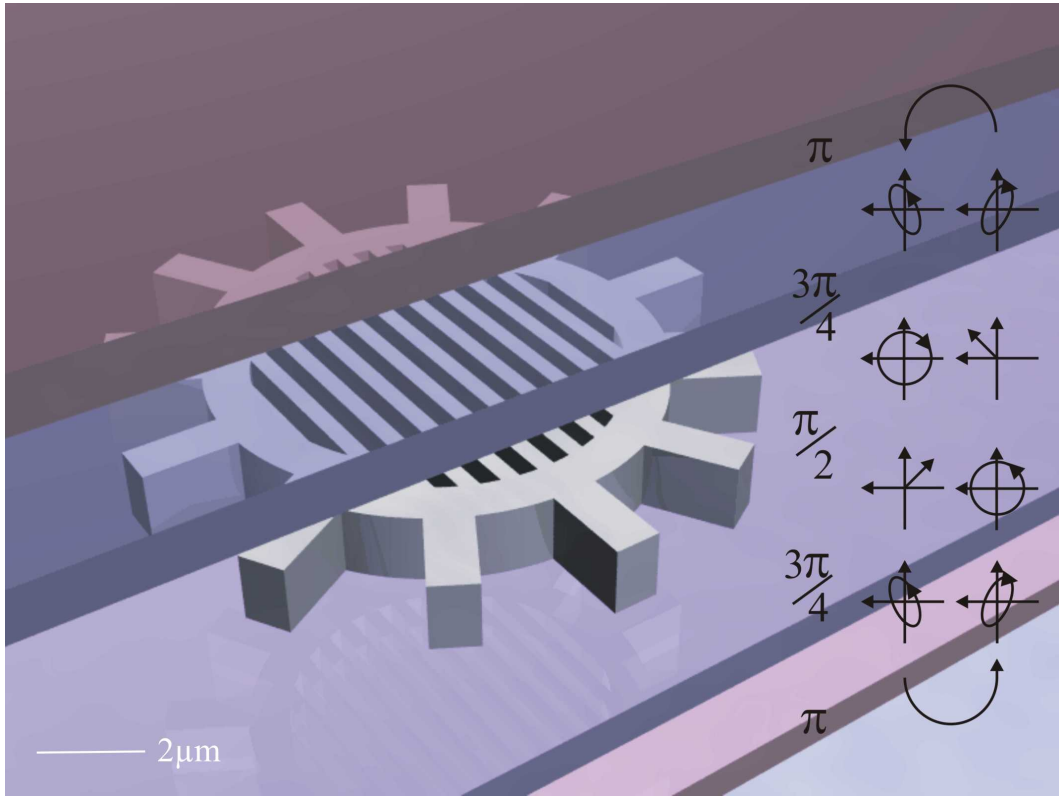


Figure 2.25: A microgear in a cavity. This diagram shows a microgear in a cavity formed by two mirrors that give  $\pi$  phase change on reflection and includes two phase plates that give  $3\pi/4$  phase change to correct the polarisation state of the light.

and below the microgear (see figure 2.25). The incident light would have to be elliptically polarised so that when it passes through the top wave plate above the gear it will become circularly polarised before passing through the microgear. In the ideal case of the microgear being a quarter wave plate this will convert the light to linearly polarised light. The light would then pass through the lower wave plate making it elliptically polarised before being reflected thus going through a  $\pi$  phase change. When the light returns through

## 2.6. SUMMARY AND OUTLOOK

---

the lower phase plate it is converted back to circularly polarised light but with the handedness changed so that it pushes in the same direction as the light going down. The cycle then continues for as long as the light stays in the cavity. As it is possible to create cavities with large Q values it could be possible to increase the momentum transferred from the light by several orders of magnitude.

### 2.6.3 A new way to make the world go 'round?

Sections 2.6.1 and 2.6.2 show ways to increase the amount of power that is transferred from the light beam to the microgear. This section will look at how much these techniques can increase the power given to the microgear, could this be a new way to harvest power from light?

At first appearance this technique seems very poorly suited to the generation of power as we have only demonstrated the rotation of a microscopic gear and it requires 1W (a lot of power) to induce a fairly pedestrian rotation rate of 60rpm. However as we have seen, there are several things we could do to improve this and as power harvesting is such an important area of research, it is interesting to consider angular momentum transfer as a source of power. The momentum transferred from the light to the microgear depends on the microgear's birefringence (see equation 2.1) and is a maximum of  $2\hbar$  per photon when  $\Delta n_{eff}d = \frac{\lambda}{2}$ . This represents the maximum amount of energy that can be passed from the light to the microgear as the light passes through it. However it is possible to send the light through the microgear more than once by putting it in a optical cavity. Here the light would pass through the microgear many times giving up to  $2\hbar$  per photon momentum each time. Comparing this with a solar cell that can capture up to around 25 percent of the photon energy  $h\nu$  which is a factor of around  $\nu = 5 \times 10^{14} Hz$  higher. This means that

## 2.6. SUMMARY AND OUTLOOK

---

a cavity with a Q of around  $10^{14}$  would be needed to match solar cells and then the power would still need to be converted into electrical energy. Although no light is absorbed as it passes through the microgear, there will be a practical limit to the Q value due to the scattering from the microgear and this is sure to be below  $10^{14}$ . This shows that power harvesting is not a good application for this technology.

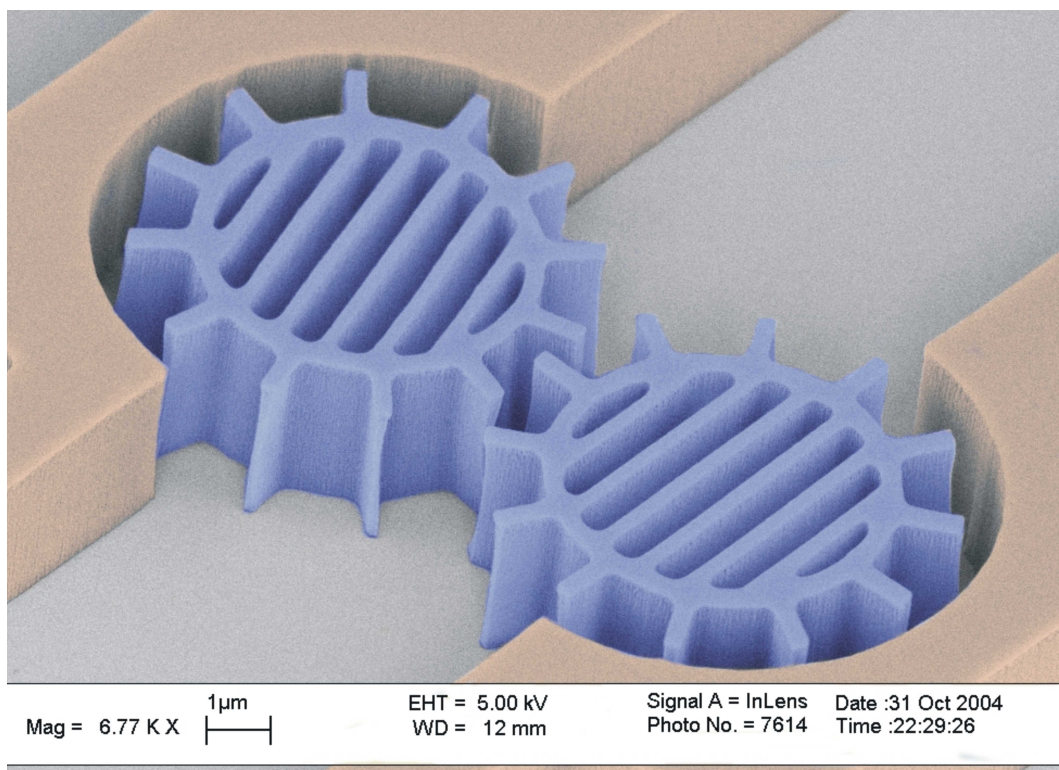


Figure 2.26: This coloured micrograph shows a microgear pump that was constructed from SU-8 using a FOx-12 mask. The microgears would be illuminated with circularly polarised light of different handedness making them spin in opposite directions driving liquid around the edges of the channel.

## 2.6. SUMMARY AND OUTLOOK

---

### 2.6.4 Conclusion

This work clearly shows that form birefringence has potential applications for actuating micromachines such as a micropump (see figure 2.26) or to create tools to use in biological experiments even though very little power is transferred from the beam to the microgear. Future work should focus on;

- Varying the pitch and fill factor of the photonic crystal to check the birefringence changes as the simulations suggest.
- Increasing the birefringence of the microgears by using higher refractive index material.
- Increasing the torque per incident photon by creating a cavity.

The success of these techniques will depend on our ability to increase the force provided whilst keeping the fabrication process simple so that it is easily applied to other experiments.

## 2.7. APPENDIX

---

### 2.7 Appendix

#### 2.7.1 Reactive Ion Etching

To fabricate microgears from silicon on insulator (SOI) it is necessary to etch through 330 nm of silicon. First we tried a 130 nm layer of PMMA as the etch mask, so a selectivity of roughly 3 was required. To find how the different etching parameters affected this selectivity, a series of experiments was carried out with photoresist S1818 as an initial mask. In each case the photoresist was prepared to the same recipe, spun at 5000rpm for one minute, baked at 100°C for 1 min, exposed for 3 minutes and developed for 3-5 minutes. The first parameters tried were SF6 at 3 Pa (0.03 mbar), gas ring at position 0 (the position where the gas ring is furthest from the sample) and powers from 7 to 50W for one minute (see figure 2.27).

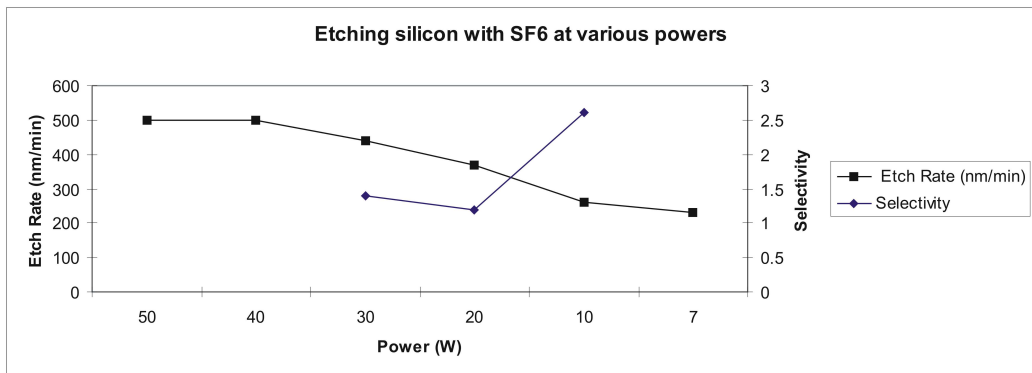


Figure 2.27: This graph shows how the etching rate and selectivity vary with etching power for SF6 and silicon.

As expected the etch rate declined as the power was reduced although the selectivity increased. The selectivity at powers higher than 30W could not be measured as the photoresist had become hardened and could not be removed.

## 2.7. APPENDIX

---

Using this information, a sample of PMMA on SOI was etched at the same conditions as above but low power (10W). The selectivity was found to be 1.2, not enough for our etching. The next parameter to be investigated was pressure. SF<sub>6</sub> was used with 20 W power, ring at position 0, pressures from 3 to 1.6 Pa (0.03 to 0.016 mbar) for 2 minutes (see figure 2.28).

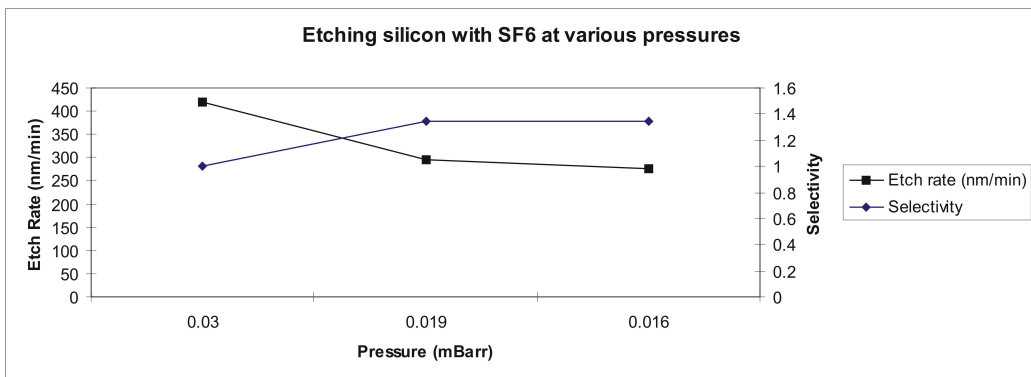


Figure 2.28: This graph shows how the etching rate and selectivity vary with etch pressure for SF<sub>6</sub> and silicon.

From this it can be seen that decreasing pressure increases selectivity but only by about one third. For pressures below 1.6 Pa (0.016 mbar), a stable plasma could not be achieved. Silicon is often etched with a mixture of SF<sub>6</sub> and CHF<sub>3</sub> as the CHF<sub>3</sub> pacifies the side walls of the etch, improving directionality. To see if this increased the selectivity at all, samples were prepared as before and etched with different mixtures of SF<sub>6</sub> and CHF<sub>3</sub>. The etch parameters used were 20 W of power, etch pressure 3 Pa (0.03 mbar), ring height 0, a mixture of SF<sub>6</sub> and CHF so that the SF<sub>6</sub> varied from 10 to 100 percent and a time of 2 minutes (see figure 2.29).

This shows that adding CHF<sub>3</sub> does not increase selectivity if anything it decreases it slightly. It was suggested that adding an inert gas such as Argon

## 2.7. APPENDIX

---

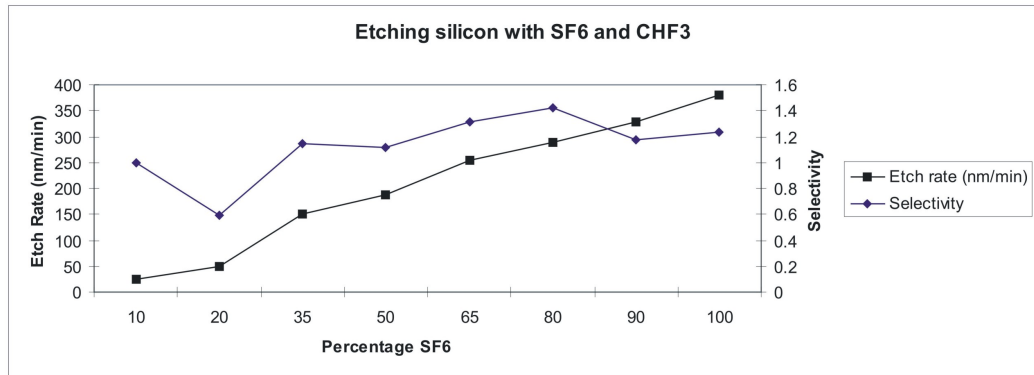


Figure 2.29: This graph shows how the etching rate and selectivity vary with the amount of SF6 in the SF6/CHF3 mix.

would reduced the photoresist etch rate. However as Argon was not available Nitrogen was used instead. Etching was performed with 10W power, at 3 Pa (0.03 mbar), ring at position 0 for 2 minutes with gas composition from 10 to 90 percent SF6 (see figure 2.30).

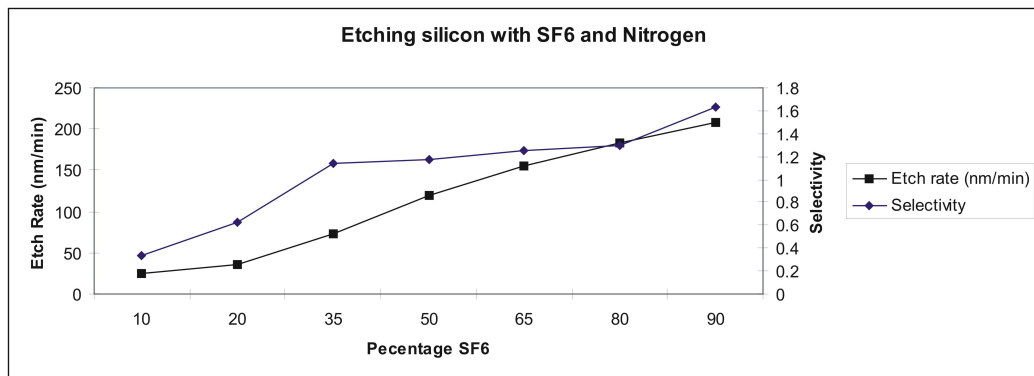


Figure 2.30: This graph shows how the etching rate and selectivity vary with the amount of SF6 in the SF6/N2 mix.

## 2.7. APPENDIX

---

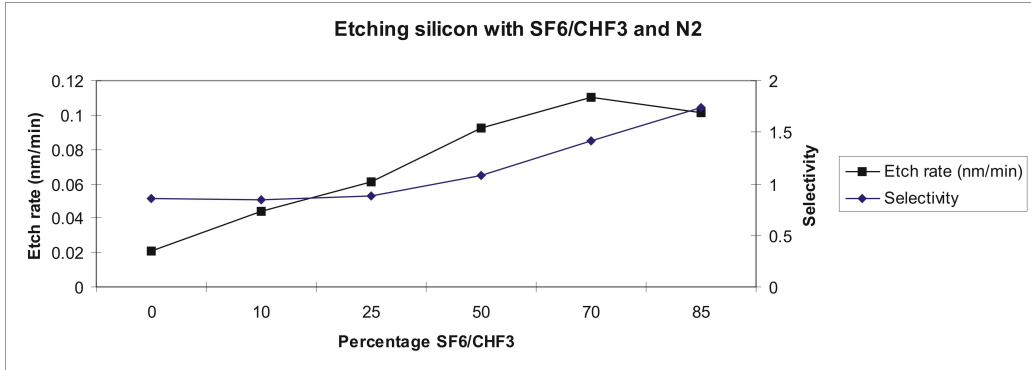


Figure 2.31: This graph shows how the etching rate and selectivity vary with concentration of SF6/CHF3 and N2.

This shows that although adding nitrogen did decrease the photoresist etch rate the end result was a decrease in selectivity. To check that the same trend would be evident for a mixture of SF6/CHF3 and nitrogen, a set of samples were etched with the same amount of CHF3 to SF6 but different amounts of nitrogen. The conditions used were 10 W power, 3 Pa (0.03 mbar), ring at position 0, and gas compositions of 10 to 90 percent SF6/CHF3 (see figure 2.31). The samples were etched for 6 minutes to increase the amount etched and increase the accuracy of the measurements.

From this it can be seen that again the addition of nitrogen only decreases the selectivity. As the addition of nitrogen had disappointing results the ability to use argon was added to the etching setup to see if it would have a more beneficial effect. A set of samples were etched at 10 W, 3 Pa (0.03 mbar), ring at position 0, with from 10 to 90 percent SF6/CHF3 in the SF6/CHF3/Ar mix (see figure 2.32).

This shows a peak in selectivity at 90 percent argon so these etching conditions were tried on a PMMA and SOI sample. The result was an etch depth

## 2.7. APPENDIX

---

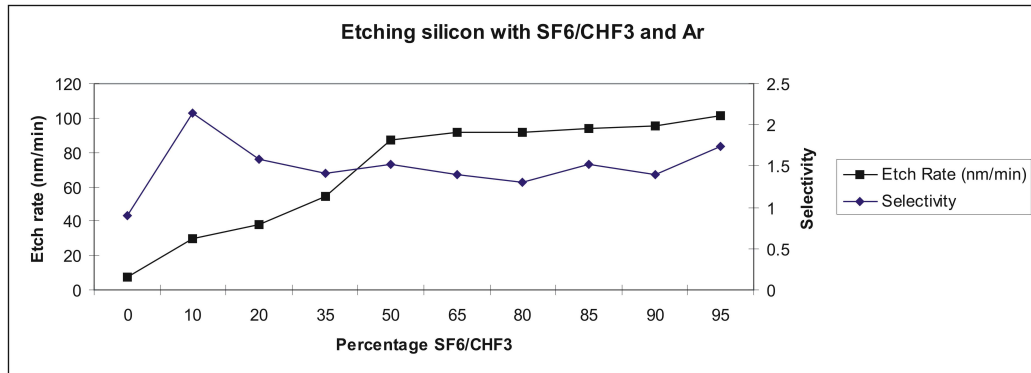


Figure 2.32: This graph shows how the etching rate and selectivity vary with concentration of SF6/CHF3 and Ar.

of 120nm with a 120nm layer of PMMA giving a selectivity of 1 which is not as good as before just using SF6. One more parameter was available to vary, the height of the gas ring. A set of samples were etched with SF6 and CHF3 at 10 W, 3 Pa (0.03 mbar), with ring ring lowered from 0 to 40 mm towards the sample for 6 minutes (see figure 2.33).

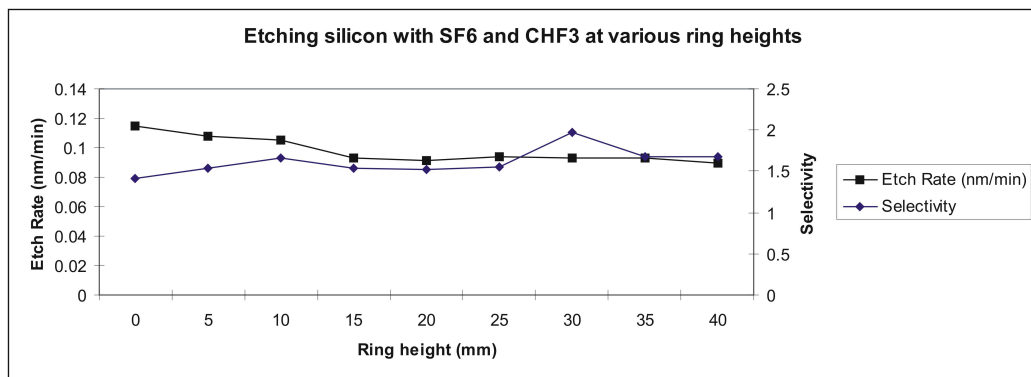


Figure 2.33: This graph shows how the etching rate and selectivity vary with the height of the gas ring.

## **2.7. APPENDIX**

---

This shows that the height of the ring does not significantly effect the selectivity of the etching. Hard baking the PMMA before etching was also tried. A sample was baked at 90°C for 30 minutes before etching but no increased selectivity was observed. From this it was concluded that 330nm of silicon could not be etched with a 130nm PMMA layer and either increasing the thickness of the resist or moving to a a 2 step approach would be necessary.

In summary, the best conditions for good selectivity were found to be low power (10W) and low pressure (1.6 Pa, 0.016 mbar). It was found that the selectivity was not increased by adding CHF<sub>3</sub>, N<sub>2</sub> or Ar, or by changing the height of the ring.

---

## BIBLIOGRAPHY

- [1] Ashkin A, Optics Letters 11 288 (1986).
- [2] Bishop AI, Nieminen TA, Heckenberg NR, Rubinsztein-Dunlop H, Physical Review Letters, Vol. 92, No. 19 198104-1 (2004).
- [3] Maruo S, Ikuta K, Korogi H. Journal of Microelectromechanical Systems, Vol. 12, No. 5, 533 (2003).
- [4] Galajda P, Ormos P. Applied Physics Letters Vol. 78 No. 2 249 (2001).
- [5] Higurashi E, Ohguchi O, Tamamura T, Ukita H, Sawada R. Journal of Applied Physics, Vol. 82, No. 6, 2773 (1997).
- [6] Gauthier RC, Tait RN, Ubriaco M. Applied Optics Vol. 41 No. 12 2361 (2002).
- [7] Higurashi E, Sawada R, Ito T. Journal of Micromechanics and Microengineering, Vol. 11, 140 (2001).
- [8] Friese MEJ, Rubinsztein-Dunlop H, Gold J, Hagberg P, Hanstorp D. Applied Physics Letters Vol. 78, No. 4, 547 (2001).

## BIBLIOGRAPHY

---

- [9] Nieminen TA, Heckenberg NR, Rubinsztein-Dunlop H. Journal of Modern Optics, Vol. 48, No. 3, 405-413 (2001).
- [10] Friese MEJ, Nieminen TA, Heckenberg NR, Rubinsztein-Dunlop H, Nature 394, 348-350 (1998).
- [11] Ng JMK, Fuerstman MJ, Grzybowski BA, Stone HA, Whitesides GM. J. AM. CHEM. SOC. Vol. 125, No. 26, 7948 (2003).
- [12] McCord MA, Introduction to Electron-Beam Lithography, Short Course Notes Microlithography, SPIE's International Symposium on Microlithography, p63, 14-19 March, (1999)
- [13] Rai-Choudhury P. Handbook of Microlithography, Micromachining, and Microfabrication: Volume 1. SPIE.
- [14] Krauss TF, Physics World, 19 (2), 32-36, (2006).
- [15] Neale SL, MacDonald MP, Dholakia K, Krauss TF. Nature Materials Vol. 4, 530-533 (2005).

---

---

# CHAPTER 3

---

## Optical Sorting

### 3.1 Introduction

The controlled manipulation of colloid is critically important not just for the study of the physics of colloidal suspensions, but also for medical science, where we can replicate a biological suspension with a colloidal one. One important device in the control of colloidal suspensions is a sorter. A sorter allows the purification of a sample and could be used, for example, to separate a pure population of stem cells from all the other species of cell found in a blood sample. A sorter could also be used to sort one cell type from another so that they may be counted. This may help with tests such as a Complete Blood Count (CBC), which is a count of the different types of cells in a blood sample, and is a vital piece of information in monitoring a patients health.

Conventional methods of cell separation and concentration are passive methods such as filtration, centrifugation and Magnetically Activated Cell

### 3.1. INTRODUCTION

---

Sorting (MACS), or active sorting methods such as Fluorescence Activated Cell Sorting (FACS). Of these, the state of the art technique is FACS, so we will look into the mechanism of this technique in more detail.

#### 3.1.1 State of the art, Fluorescence-Activated Cell Sorting FACS

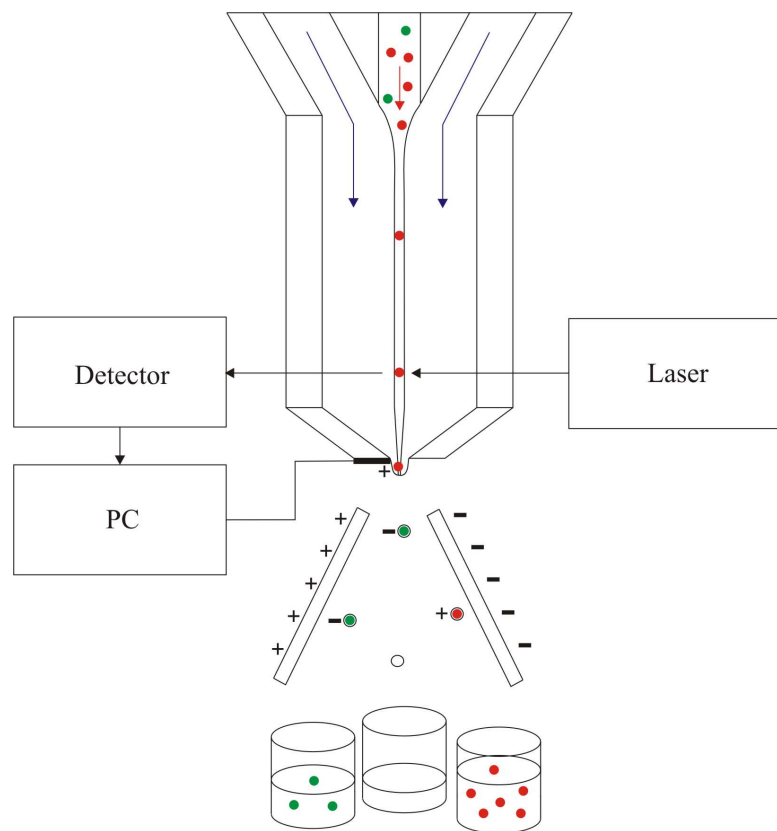


Figure 3.1: Diagram of a FACS machine. This shows a population of fluorescence labeled cells (green circles) and non labeled cells (red circles) being hydrodynamically focused, interrogated, charged then electrostatically deflected.

Figure 3.1 shows the processes involved in FACS. First a mixture of fluorescence tagged and non tagged cells is hydrodynamically focused into a stream

### **3.1. INTRODUCTION**

---

only one cell wide. The cells then pass through a laser beam that excites fluorescence if the cell is tagged, which is then picked up by the detector. The stream is then split into droplets, with just one cell in each droplet. A PC connected to the detector charges each droplet depending on whether the detector has detected a fluorescent cell, a non fluorescent cell or no cell. The droplets are then electrostatically deflected by charged plates into one of three tubes depending on their charge. Although this is a serial process with only one cell at once being sorted, the state of the art machines can process up to 50,000 cells per second. However the instruments are complicated, expensive and require trained dedicated staff and as such can only be found in hospitals and research institutes [1]. There is an increasing interest in miniaturizing these technologies onto an 'Lab-on-A-Chip' (LOC) platform [1][2][3][4]. This would allow the creation of a point of care device that could be used in a doctors surgery or even at home.

In this chapter I will present an optical sorting approach that uses the different optical properties of particles to sort them with an optically induced force. This has advantages of being able to sort particles over the area of a channel instead of one at a time and is elegant, using the optical properties of the particles to differentiate them and move them. An example is separating red and white blood cells that due to their different shape and size exhibit different optical responses. Sorting techniques such as these will be essential in ensuring LOC products such as Agilent's Bioanalyzer reach their full potential [5].

It has previously been shown that an array of optical traps can divert colloid from its original trajectory by a lattice of optical traps [6], however the demonstrated angle of diversion was limited. By creating an optical lattice with an interference pattern, it was shown that interlinking the trap sites (see

### 3.1. INTRODUCTION

---

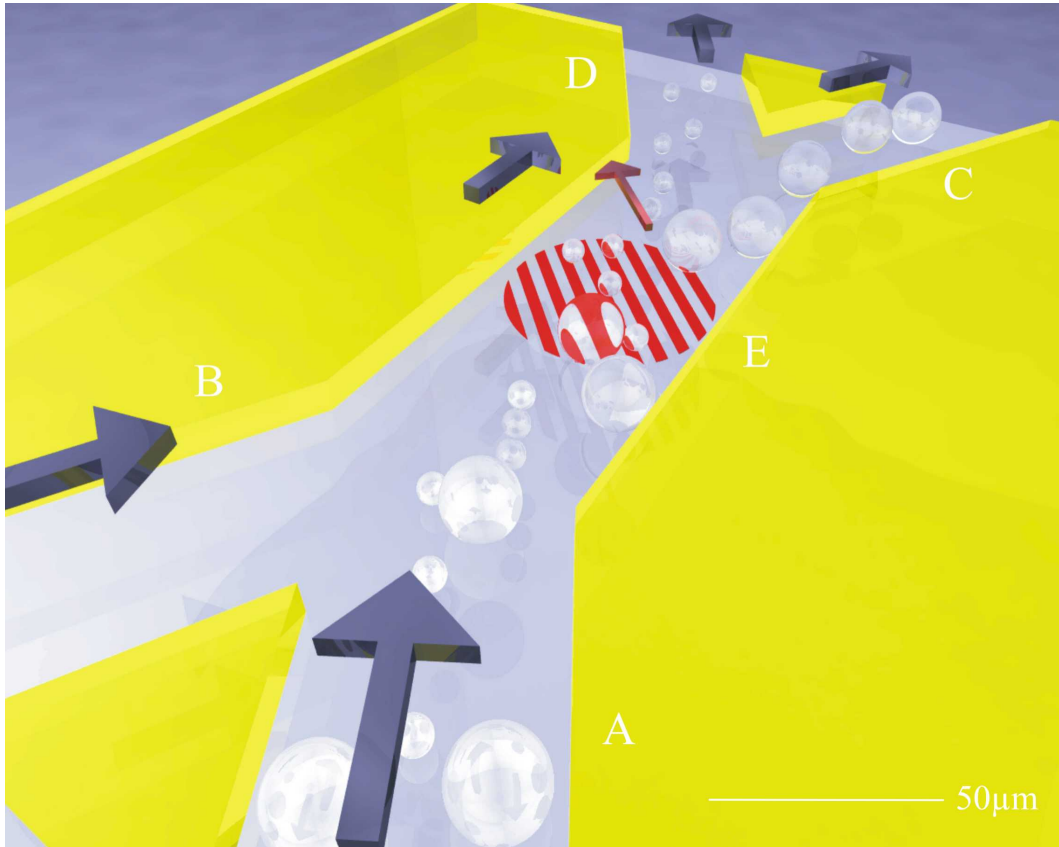


Figure 3.2: Optical Sorting. The blue arrows show the direction of fluid flow and the red arrow indicates optical forces. The mixed colloid enters by channel A and water by channel B. The smaller colloid experiences forces from the optical pattern E moving it into channel D whilst the larger colloid goes straight through the optical pattern and out channel C.

section 3.3) allowed the diversion of colloid at a much greater angle [7]. Here it was also shown that by choosing the parameters of the optical lattice one species of colloid could be diverted whilst another was appropriately unaffected (see figure 3.2). However the flow in these experiments is simulated by moving the stage, which gives an imperfect approximation of real flow (see section

### **3.1. INTRODUCTION**

---

3.4). In this chapter, I will show the fabrication and testing of microfluidic flow chambers designed to show optical sorting in a real flow. I will discuss different fabrication techniques and show the results of sorting experiments in the finished channels.

## **3.2. FABRICATION OF A MICROFLUIDIC FLOW CHAMBER**

---

### **3.2 Fabrication of a microfluidic flow chamber**

To help demonstrate the fractionation of colloid using an optical lattice I developed a fabrication process for creating microfluidic flow chambers. I tested two methods of fabrication. The first method involved constructing channels in SU-8 on a substrate by photolithography. These were then sealed by gluing them to a cover slip (see section 3.2.2). The second method involved casting channels of Poly(dimethylsiloxane) (PDMS, Dow Corning) using a soft lithography method and then bonding the PDMS to a glass cover slip (see section 3.2.3). Both methods rely on photolithography so it is necessary to discuss this technique.

#### **3.2.1 Photolithography**

Photolithography is a well developed technique that is widely used to pattern material on the micron scale for applications ranging from microprocessor fabrication and micro optics to microfluidics and Lab-on-a Chip systems. It involves projecting light through a mask onto a piece of material that has been coated with a photosensitive resist called photoresist (see figure 3.3). The masks are usually patterned by electron beam lithography (see section 2.4.1.1) and consist of a layer of metal in the pattern desired on a glass plate. The pattern in the mask blocks light from reaching parts of the resist. For a positive resist the illuminated areas are rendered more soluble whilst the unilluminated area remain non-soluble. The sample is then developed and the more soluble areas are washed away. There are also negative resists that become less soluble on exposure so that only the exposed areas are left after development. Either way, the end result is a pattern in resist that can be transferred into the material by an etching technique. In St Andrews, photolithography is carried

### 3.2. FABRICATION OF A MICROFLUIDIC FLOW CHAMBER

---

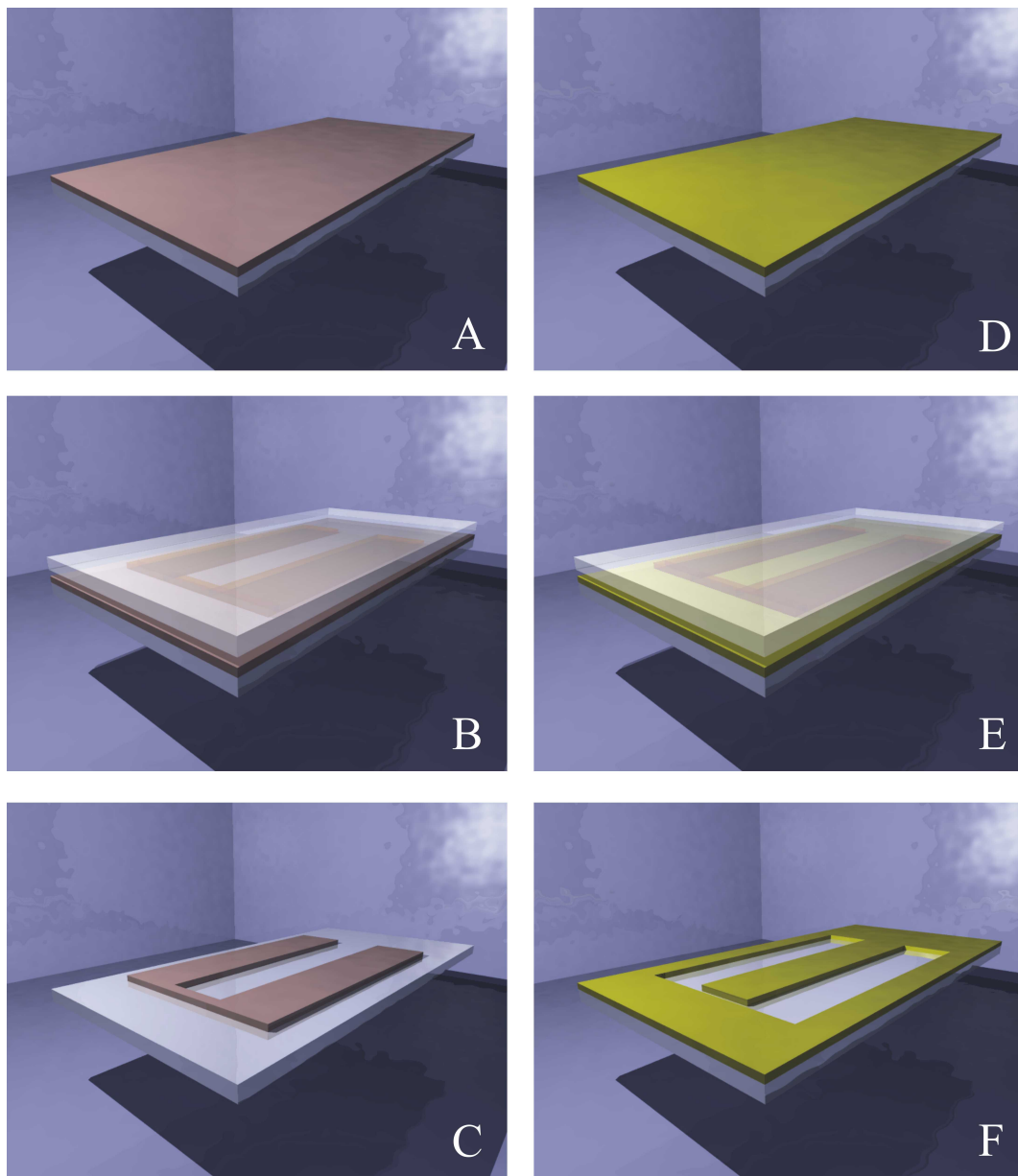


Figure 3.3: Photolithography. A substrate is coated in positive (A) or negative resist (D) then exposed to UV radiation through a mask (B,E). Developing causes the exposed areas of the positive resist to be removed (C) and the non exposed areas of the negative resist (F).

## **3.2. FABRICATION OF A MICROFLUIDIC FLOW CHAMBER**

---

out on a Karl Suss MJB-3 mask aligner that operates at 405 nm (Hg H-line) and 365 nm (I-line). This machine is used to align the pattern on the mask to any feature that may already be on the sample and to ensure the correct pressure is applied between the mask and the sample. This is called contact lithography as the mask comes into contact with the photoresist. The correct pressure ensures that there is no gap between the mask and the resist, that could cause a broadening of the features, without causing damage to either the sample or the mask. This is an important parameter for good reproducible photolithography. Another possible cause for a gap between the mask and the resist comes from a non-uniform resist layer. The resist is typically spun onto the material which can cause a build up of resist at the edges of the sample called an edge bead. This is a particular problem for high viscosity photoresists that give thick films and the edge bead must be removed for a good result. I have found that the easiest way to remove edge beads from a positive resist is to expose the edges and develop the resist around the edges away. I have found no similarly neat technique for dealing with a negative resist (SU-8) but this is rarely a problem as it is typically used for microfluidic channels where the critical dimensions are large. The exposure times and doses used are discussed later in the different fabrication recipes.

### **3.2.2 SU-8 microfluidic channels**

SU-8 2050 (MicroChem) was spun onto a cover slip at 1250 rpm for 60 s to give the desired thickness of  $100 \mu m$ . This was then patterned by photolithography to produce the channels. Norland optical adhesive was spun onto a cover slip and the channels were placed onto this. The speed at which the adhesive is spun at is critical. If spun too fast, there is not enough glue left and the channels will not be sealed. If spun too slowly, there will be too much glue and

### 3.2. FABRICATION OF A MICROFLUIDIC FLOW CHAMBER

---

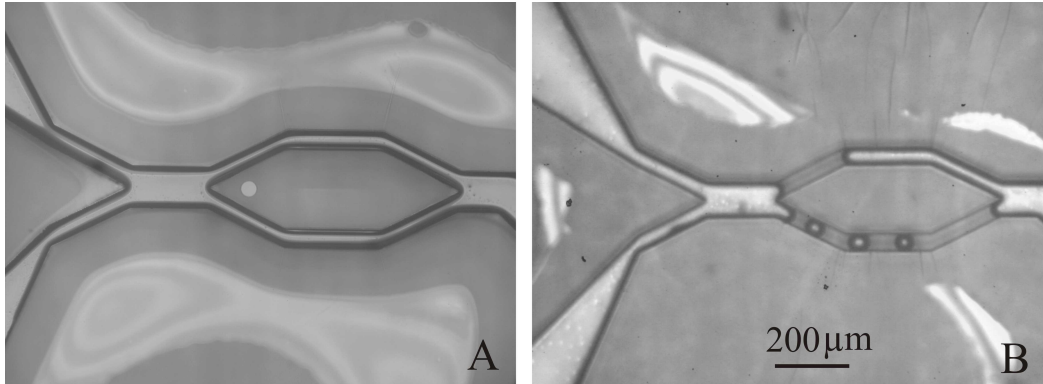


Figure 3.4: Channels fabricated using the gluing method. A) A good continuous channel. B) A channel blocked with glue.

it will fill the channels. The adhesive was then exposed to UV radiation to cure it. The resulting channels can be seen in figure 3.4. This method proved to be unreliable with no spin speed found to produce an amount of glue that would work every time.

#### 3.2.3 PDMS microfluidic channels

The second method involved constructing channels in Poly(dimethylsiloxane) (PDMS, Dow Corning) and then bonding the PDMS to a glass cover slip. This method is widely used [10, 11, 12, 13, 14] and was found to be reliable. As PDMS is not photosensitive it is first necessary to make a mould of an inverted channel. This is then used to pattern the PDMS in a method known as soft lithography. To create an inverted channel, it is necessary to have the inverse of the mask used for the SU-8 channel method. This was created using the previous mask and a lift off technique, see section 3.2.3.1

## 3.2. FABRICATION OF A MICROFLUIDIC FLOW CHAMBER

---

### 3.2.3.1 Lift-off

To create a negative of the mask, a lift-off technique was used. The simplest form of lift-off involves creating a pattern in photoresist onto which a metal is evaporated. When the resist is then dissolved, the gold is left in the areas where there was no resist so that the pattern is a negative of the original mask (see figure 3.5). However, as the edge of the resist tends to form a slight curve instead of a vertical wall, there can often be a continuous layer of gold from the substrate onto the top of the resist. If this occurs, the gold will tear when the resist is removed, thus leaving a jagged edge to the pattern. To prevent this, a Lift-Off Resist (LOR, Shipley) is used.

This is spun on before the photoresist and is baked so that it is slightly more soluble than the photoresist. The photoresist is then patterned as usual and when it is developed, some of the LOR is removed from under the photoresist leaving an overhang. This ensures that there can be no continuous layer of gold giving a crisp edge to the pattern. The critical dimension when using LOR is the size of the overhang. If there is no overhang in the resist it will give a rough edge to the gold, if however there is too much overhang, the resist will collapse onto the substrate and allow the gold to form a continuous layer, resulting again in a rough edge. It was found that an overhang of 0.5 to 1  $\mu\text{m}$  was optimal. To achieve this reliably, bake temperatures and times as well as development times were varied. It was found that the critical parameter was bake temperature with  $190^\circ\text{C}$  rather than the manufacturers guideline  $180^\circ\text{C}$  giving the best results.

### 3.2.3.2 Soft Lithography

The inverted mask was used to create a mould for soft lithography. The process of soft lithography is described in figure 3.7.

### 3.2. FABRICATION OF A MICROFLUIDIC FLOW CHAMBER

---

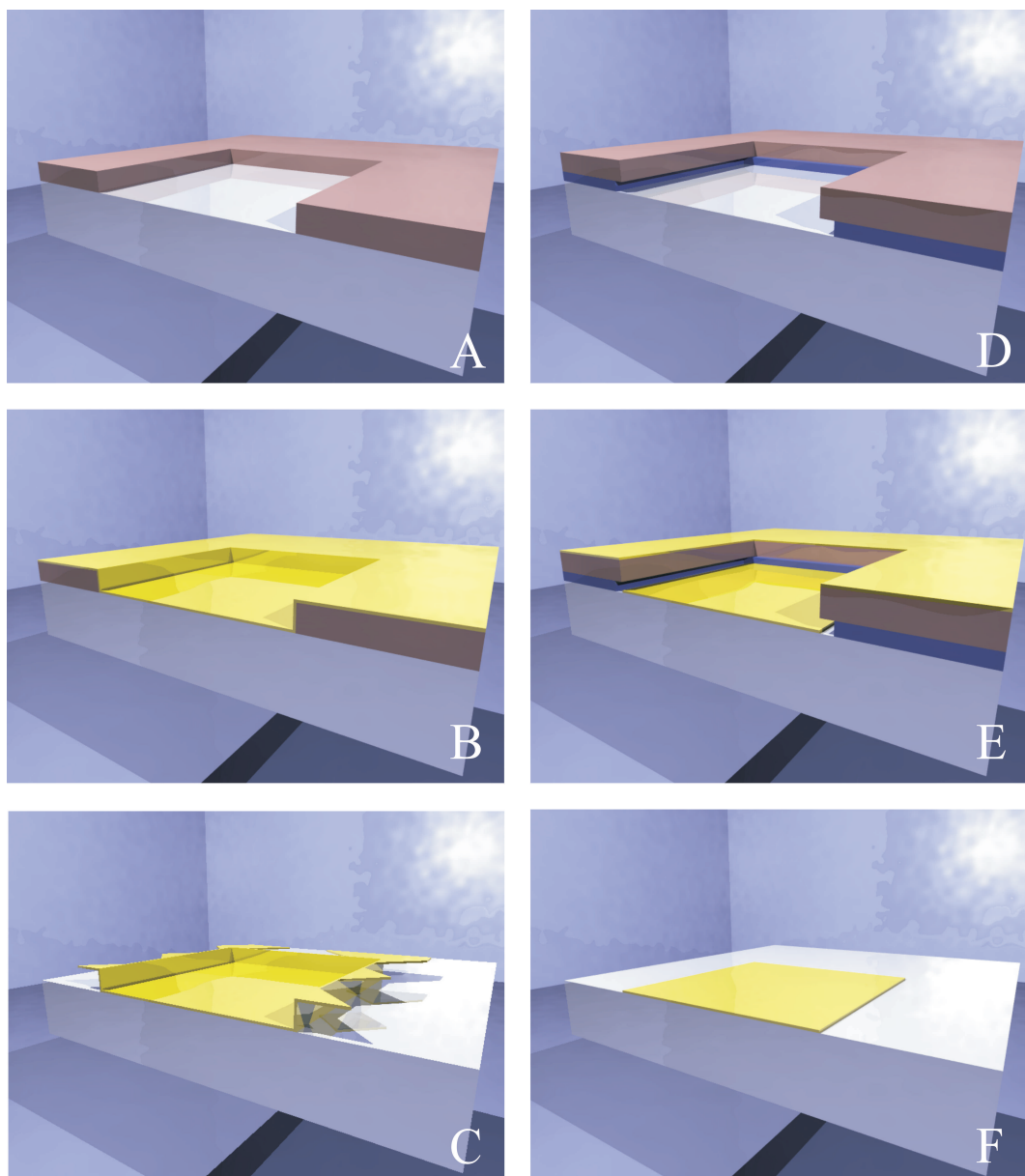


Figure 3.5: Lift-off. A pattern is made in either photoresist (A) or Lift-Off Resist (LOR) and photoresist (D). The gold is evaporated on leaving a continuous layer on the photoresist (B) and a clear break on the LOR (E). The photoresist and LOR are removed leaving excess gold (C) or a neat pattern (F). The process D-F is therefore much more reliable and results in a neater pattern.

### 3.2. FABRICATION OF A MICROFLUIDIC FLOW CHAMBER

---

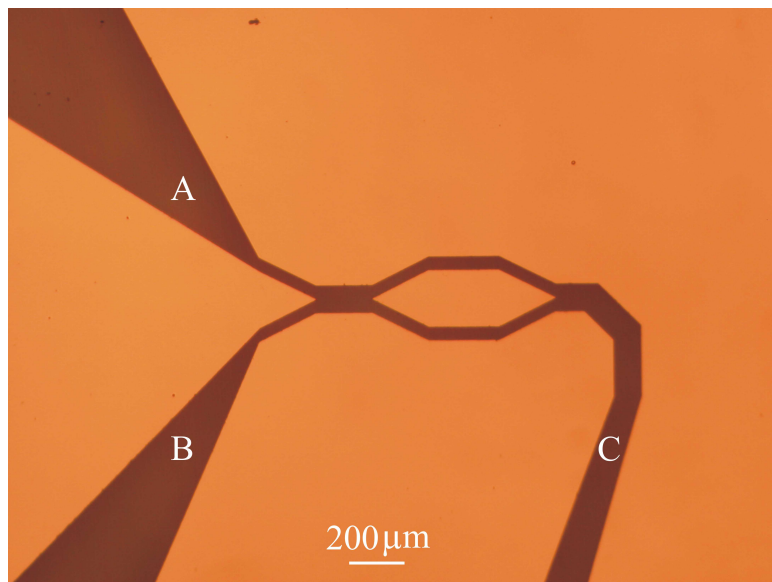


Figure 3.6: The inverted mask. LOR has been used leaving a crisp edge to the pattern. Features A and B will form inlet channels and feature C an outlet.

The mould was created in SU-8 on a glass substrate using the following recipe; SU-8 was spin coated onto a large cover slide at 1250 rpm giving a  $100\mu\text{m}$  thick layer. The sample was then heated in a two stage pre exposure bake on a hotplate at  $65\text{ }^{\circ}\text{C}$  for 5 mins then  $95\text{ }^{\circ}\text{C}$  for 5 mins. The sample was exposed on the above mentioned mask aligner through a mask such as the one in figure 3.6 for 60s. It was then heated in a two stage post exposure bake with the same conditions as the pre exposure bake. The sample was developed in EC solvent for 9 mins and then developed again in a fresh beaker of EC solvent for 30s to finish the development. This produces a mould with the desired shape of the channels being mesas in the SU-8.

Liquid PDMS mixed in a ratio of 10:1 was then poured onto the mould and cured in an oven at  $180\text{ }^{\circ}\text{C}$  for 15 mins. When cured, the PDMS was

### 3.2. FABRICATION OF A MICROFLUIDIC FLOW CHAMBER

---

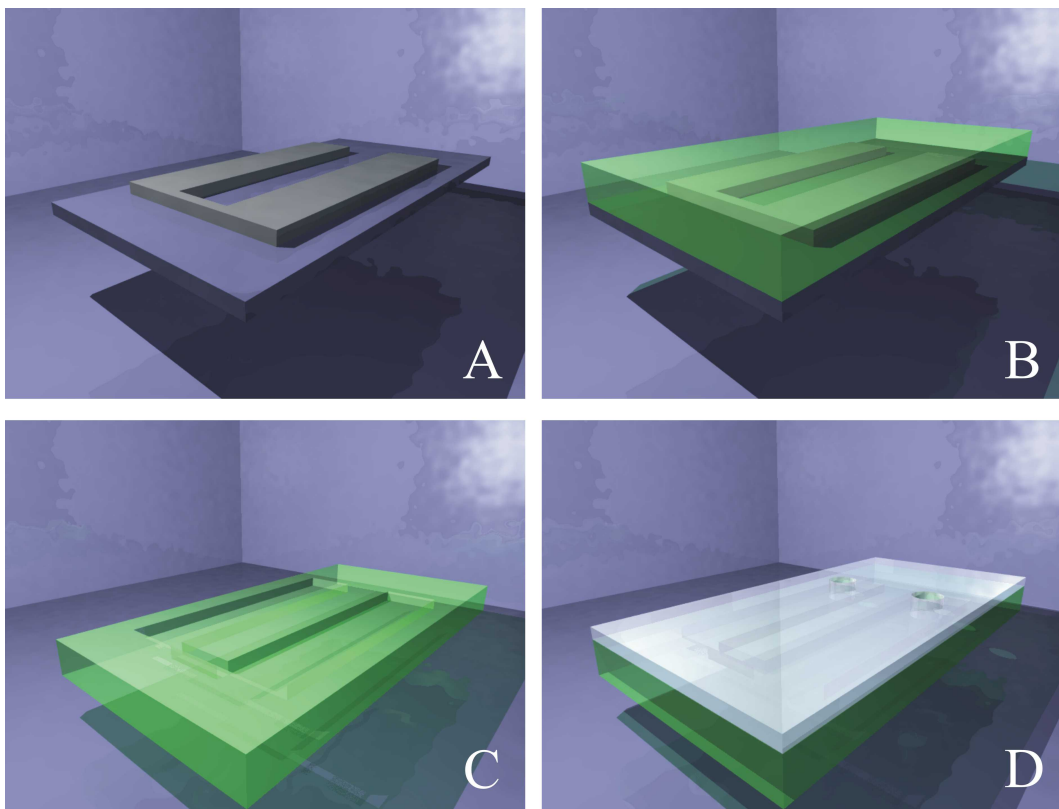


Figure 3.7: Soft lithography. A) A mould is made from SU-8 on a glass substrate. B) Liquid PDMS is poured onto the mold and cured. C) The hard PDMS is then peeled from the mould and inverted. This and a drilled coverslip are then exposed to an oxygen plasma. D) The exposed sides of the PDMS and cover slip are pressed together forming an irreversible bond.

peeled from the mould and placed inverted onto a coverslip for support. This and a cover slip with holes for inlets drilled into it were exposed to an oxygen plasma. The exposed sides of the PDMS and cover slip were then pressed together forming an irreversible bond. As the PDMS is completely removed the mould can be used several times. However, it was found that at weak

### **3.2. FABRICATION OF A MICROFLUIDIC FLOW CHAMBER**

---

points where the SU-8 had cracked the mould could break leaving some SU-8 in the channel thus destroying the mould (see figure 3.8).

Using a silicon substrate for the mould reduced the amount of cracking of the SU-8 and hence the mould lasted longer. The mould often looked better after first being used as any small cracks would fill with PDMS and not be removed from the mould when the rest of the PDMS was removed. Using this mould it was possible to create channels that were an exact replica of the mask (see figure 3.8(E)). To connect the channels to a pump, glass inlets were then glued to the drilled coverslip. Norland Optical Adhesive (NOA 71) was used as it is desirable to allow the glue to enfold the whole of the inlet but then be able to fix the glue before it enters the microchannels. This is possible with NOA as it is possible to fix it by exposing it to UV radiation. Figure 3.9 shows a completed flow chamber.

One inlet has been filled with rhodamine and the other with blue food colouring so that the liquid in each channel can be distinguished. The insert shows a close up of the flow through the channels when pressure is applied to the two inlets, the flow direction being from left to right. It can be seen that flow through the channels is laminar with no turbulent mixing and that a small amount of diffusion has occurred from one channel to the other as the boundary between the two liquids is sharper towards the left of the channel than the right. Flow cells made in this way were used in optical sorting experiments (see section 3.4). However there remains a few problems with the fabrication process. The first is the formation of bubbles in the PDMS (see figure 3.10).

This may be due to semi exposed SU-8 that can be seen next to the channels outgassing. The amount of semi exposed SU-8 increases as the exposure increases so the number of bubbles also does. It is desirable to expose the SU-8 as long as possible as it cuts down the number of cracks so that the best

### 3.2. FABRICATION OF A MICROFLUIDIC FLOW CHAMBER

---

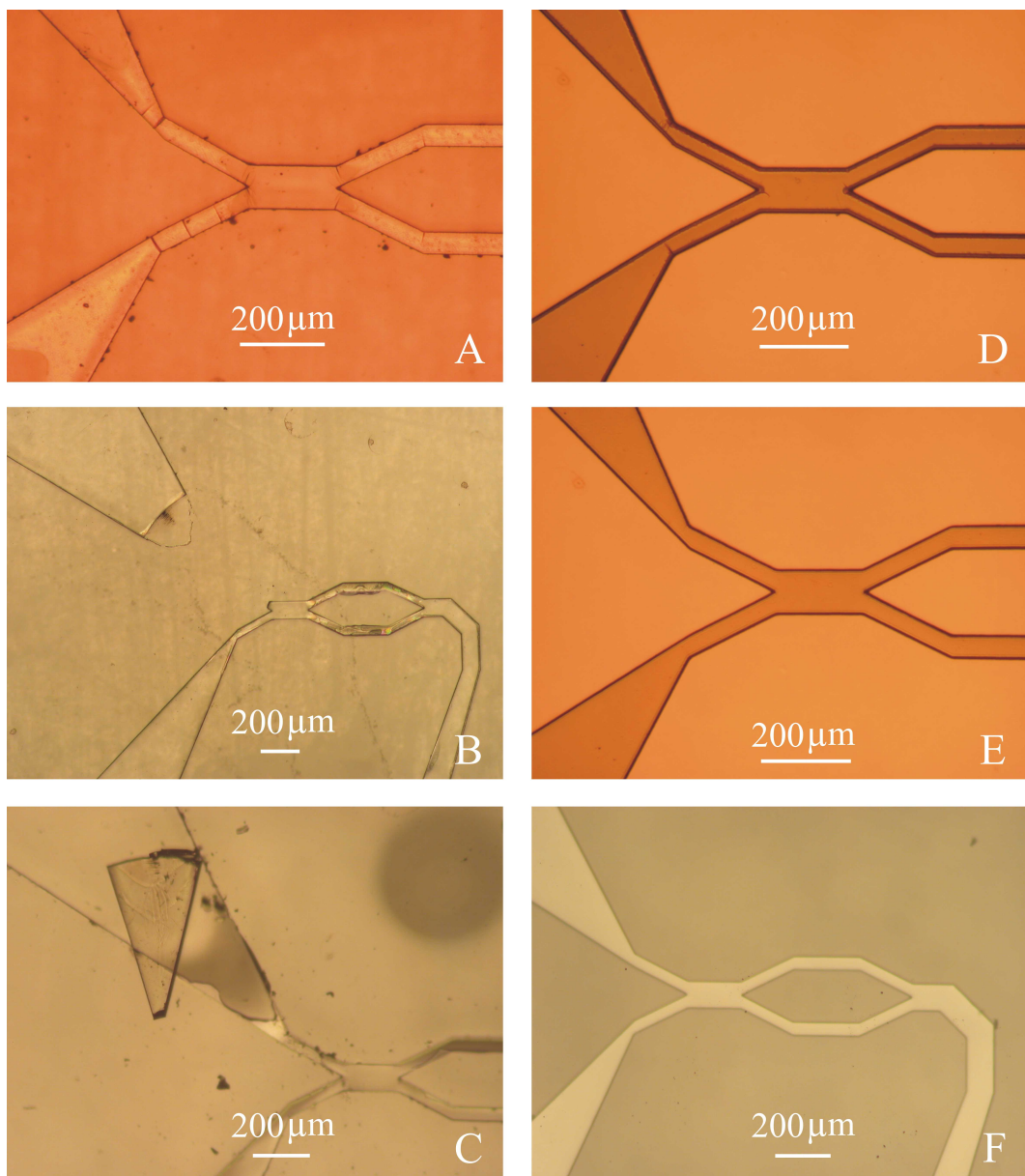


Figure 3.8: SU-8 moulds on glass and silicon. A) SU-8 moulds made on glass showed cracks. B) As the PDMS is peeled away the mould can break. C) The PDMS ends up with SU-8 in some of the channels. D) Moulds on silicon looked less cracked. E) They look even better after the PDMS has been peeled away. E) The PDMS channels bonded to a glass cover slip are not blocked.

### 3.2. FABRICATION OF A MICROFLUIDIC FLOW CHAMBER

---

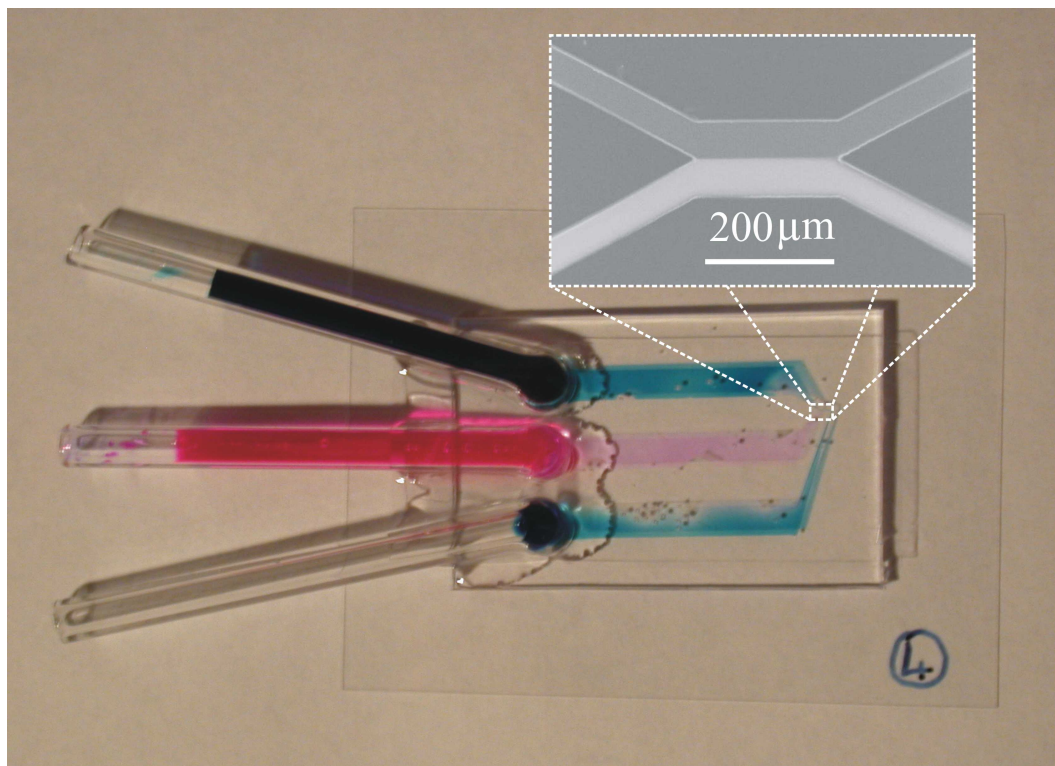


Figure 3.9: A completed flow chamber. One inlet has been filled with rhodamine and the other with blue food colouring. The inset shows a photograph taken through a microscope when there is flow through both inlets.

dose was found to be around 100s and this only caused typically one or two bubbles. The bubbles cause a problem if they are directly above the channel as they hinder imaging the channel so that some of the PDMS components made can not be used. This is not a big problem as it only takes 15 mins to make another one and PDMS is not expensive. Another limitation is the ease in which the channels become blocked (see figure 3.11).

It was thought that it would be advantageous to thoroughly clean the channels before use so that no dirt remained to act as a nucleation sight for more

### 3.2. FABRICATION OF A MICROFLUIDIC FLOW CHAMBER

---

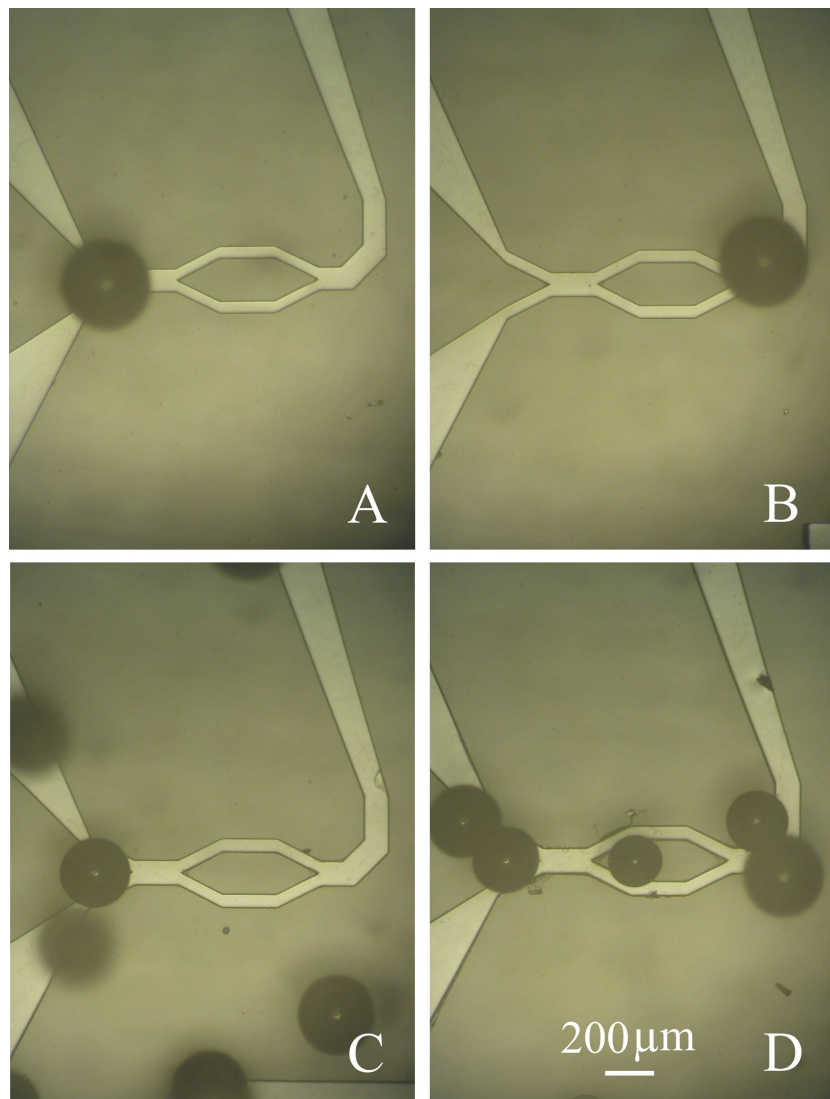


Figure 3.10: Bubbles in PDMS. The number of bubbles depends on the exposure time. A) Exposed 100s, B) 150s, C) 200s, D) 250s.

dirt. We found however, that when we passed nominally filtered and deionized water through the channels, they would fill up with dirt. The source of the dirt, whether in the water, the pipes or the channels themselves was never identified but I found that if experiments were carried out without cleaning

### 3.2. FABRICATION OF A MICROFLUIDIC FLOW CHAMBER

---

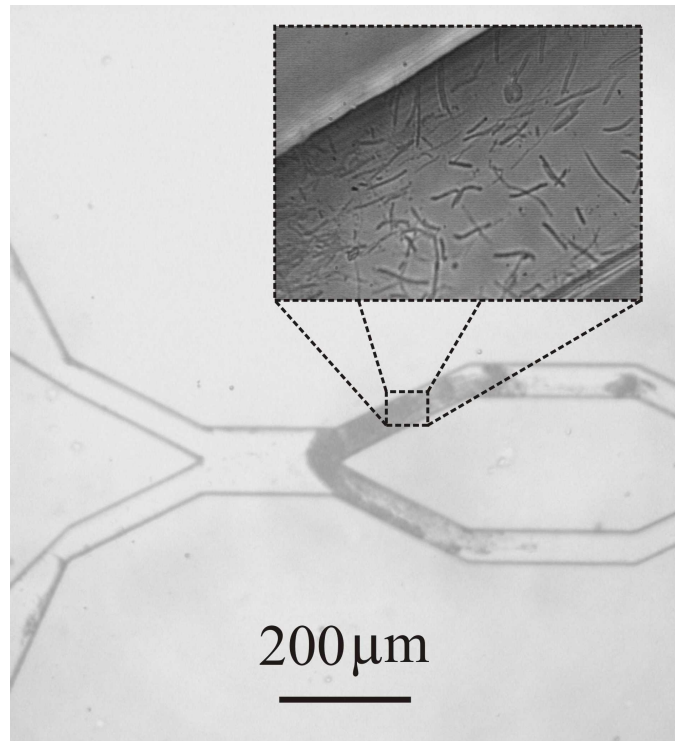


Figure 3.11: Blocked channels. These channels were blocked whilst trying to clean them with pure water.

the channels first, they would not foul up. Therefore the cleaning stage was omitted. In this way channels were created and used that were  $100 \mu\text{m}$  high with channels of width  $100$ ,  $200$  and  $500 \mu\text{m}$ . Another pattern included two  $50 \mu\text{m}$  channels that joined together into a  $100 \mu\text{m}$  channel to allow the demonstration of sorting and mixing experiments. The channels were robust to the pressure applied to the inlets from syringe pumps, although they were occasionally broken when setting up the experiment. It was therefore necessary to take care not to produce a strain across the separate inlets as this tends to crack the drilled coverslip.

### 3.3. OPTICAL SETUP

## 3.3 Optical setup

The optical sorting set-up was designed by Mike MacDonald around a Ytterbium fibre laser capable of emitting up to 10W of CW radiation at 1070nm. The laser beam is focused onto a Diffractive Optical Element (DOE) that splits the beam into 5 spots, four corners of a square and one central beam. The beams are brought together in the microfluidic chamber by an aspheric lens creating the desired interference pattern.

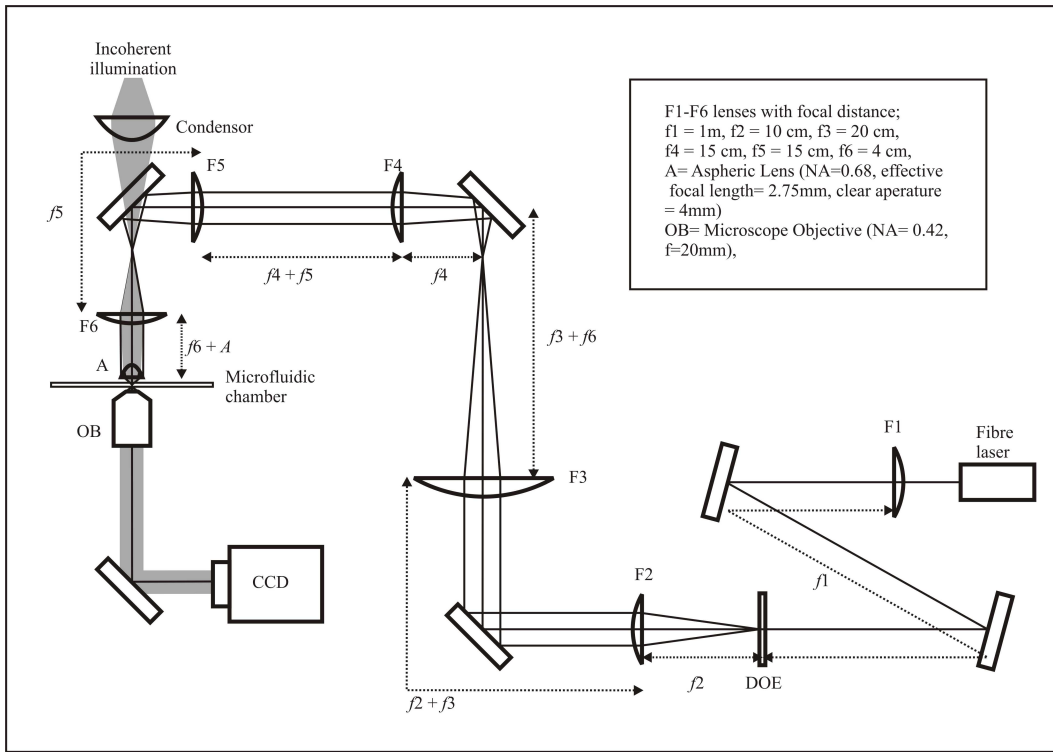


Figure 3.12: Optical sorting set-up. The beam from a ytterbium fibre laser (1070 nm) is focused onto a diffractive optical element (DOE) that creates 5 spots. These are then brought back together in the microfluidic chamber creating the desired interference pattern.

This differs from previous work in the field where many individual trap

### 3.3. OPTICAL SETUP

---

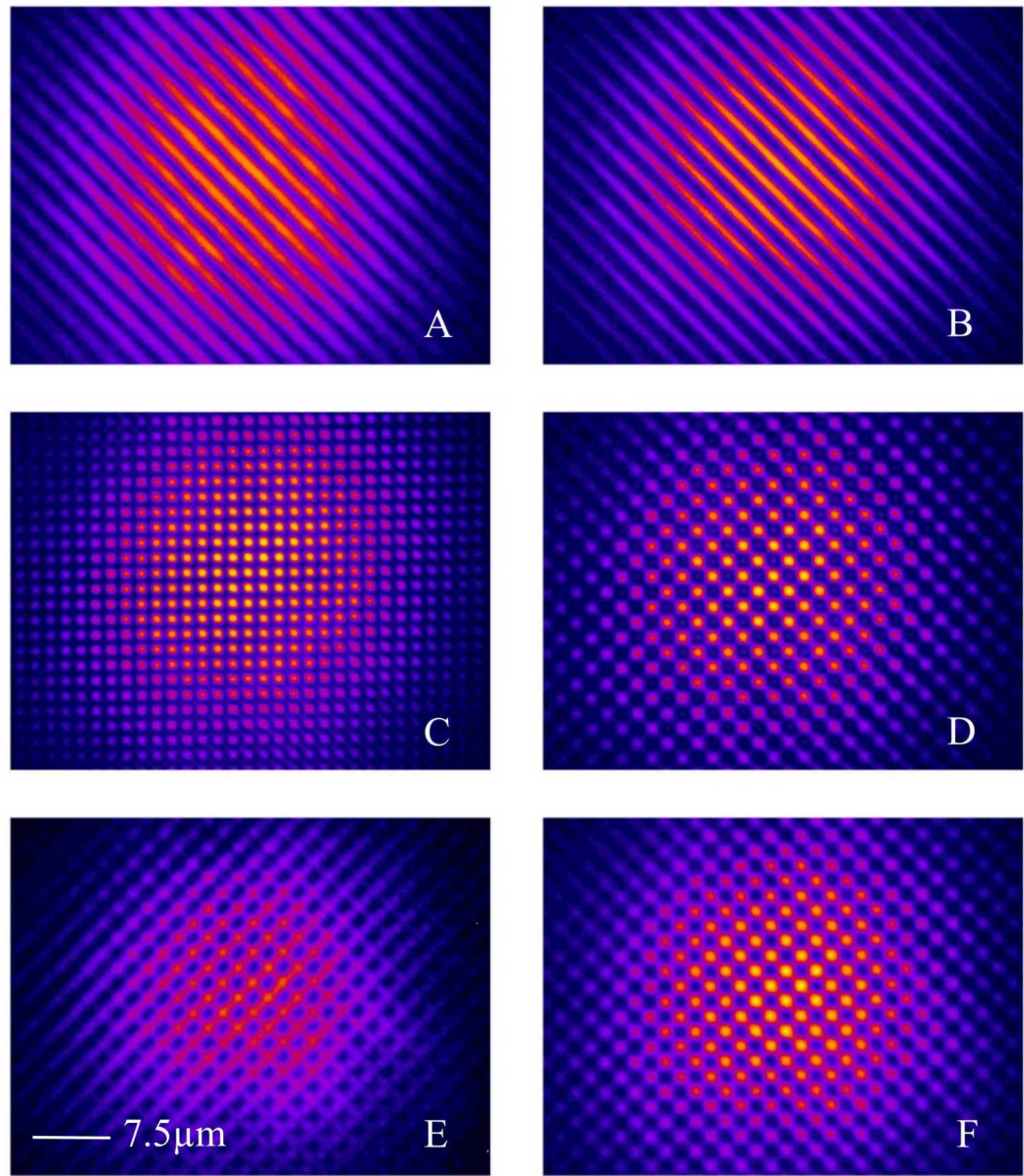


Figure 3.13: Interference patterns. These pictures are false colour images of the optical pattern with various numbers of beams of various strengths, see text. Areas of high optical intensity are shown as yellow.

### 3.3. OPTICAL SETUP

---

sites are created using a DOE [8] [6]. There are several advantages to this approach. First, by using an interference technique and varying the relative powers of each spot, the amount of linkage between each trap can be controlled. This allows us to create various patterns as shown in figure 3.13 [9]. If two beams are interfered, this gives an interference pattern as shown in 3.13A. With three beams the pattern becomes periodic in the vertical direction, similar to a log pile, and as can be seen from 3.13B, the lines of high intensity are better defined which increases the optical gradients increasing the optical forces. If four beams are interfered, we get the pattern shown in 3.13C which consists of rods of light that do not vary in the vertical direction. If 5 beams are interfered we get 3.13D which is also periodic in the vertical direction. If the path difference between the different beams is not correct to give us this pattern we may get different pattern as shown in 3.13E. This is controlled by changing the path difference of individual beam by introducing a cover slip into the beam and tilting it to slightly change the optical path. By changing the intensities of the individual beams it is possible to change the amount of interlinking between the spots of the pattern. Figure 3.13F shows a more interlinked pattern.

The level of interlinking is an important parameter for the guiding of colloid. Without interlinking, the maximum deflection angle that has been demonstrated is around  $10^\circ$  [6] whilst with an interlinking pattern an angle of greater than  $45^\circ$  is possible. A greater angle is important to sorting, as it allows the sorting over a channel of a given width with a smaller spot size, thus increasing the available intensity and hence the speed at which the particles can be moved through the optical pattern. The interference pattern also gives a sharper definition than other methods [6], increasing the optical force as this is proportional to optical gradients. Another advantage is the three

### **3.3. OPTICAL SETUP**

---

dimensional nature of the interference pattern. A 2D array of traps makes it difficult to ensure all the traps focus in the same plane as the colloid. A 3D interference pattern has vertical depth so that sorting can be done throughout the volume of a channel rather than just at the focal plane.

### 3.4. RESULTS

---

## 3.4 Results

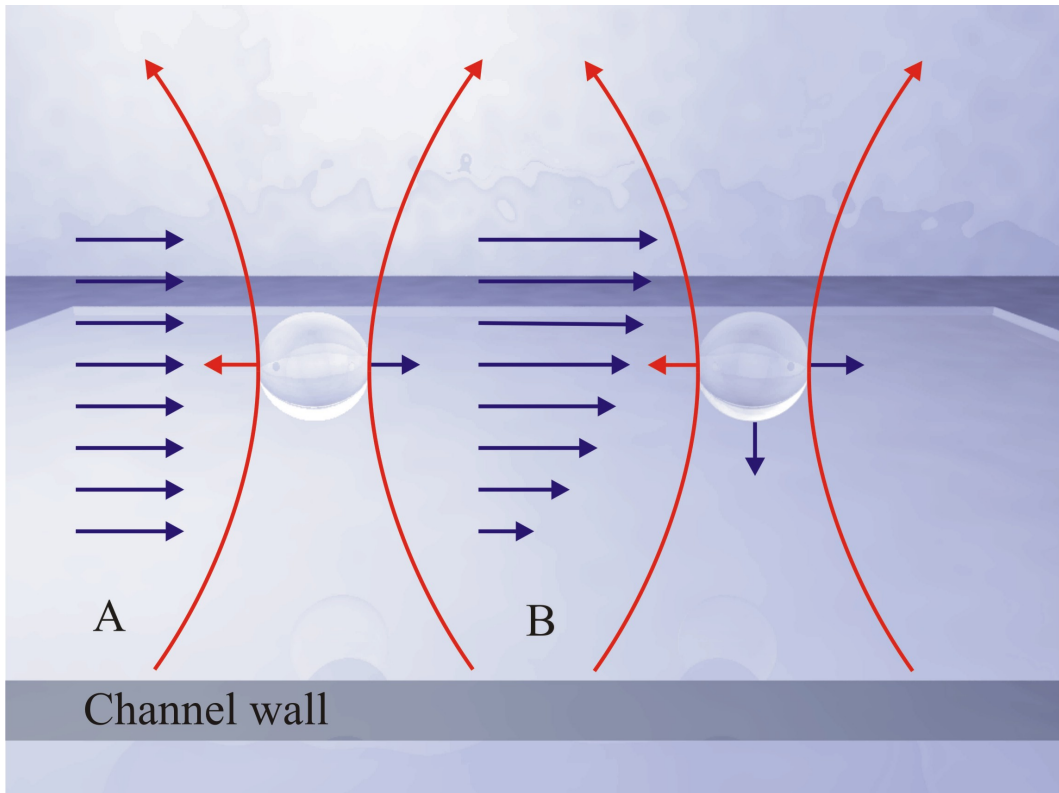


Figure 3.14: Different flow profiles. A) This is the case for forces induced by a moving stage. The particle has a force exerted on it from the optical trap (red arrow) that is countered by drag from the fluid (blue arrow). B) This is the case of a particle in a flow chamber. With pressure driven flow a parabolic Poiseuille flow profile is set up. This causes the force exerted on the particle by the flow to depend on the distance from the surface.

Previous optical sorting experiments have been carried out using simulated flow. Here a sample chamber, made from a microscope slide and cover slip separated by a vinyl spacer and filled with colloid, is moved with respect to

### 3.4. RESULTS

---

the optical pattern. This gives the impression of flow and is useful as it does not require microchannels or pumps. However the physics of the two situations are not the same as the induced flow profiles differ as shown in figure 3.14.

Case A is where the stage is moved with respect to the optical pattern. Here the particles and fluid move along with the same velocity except where the optical pattern puts a force on the particle which causes the particles to move through the fluid and is balanced by the drag force caused by this motion. The force due to drag is given by;

$$F = \beta\nu \quad (3.1)$$

Where  $F$  is the force due to drag,  $\beta$  is the drag coefficient and  $\nu$  is the fluid velocity [15]. The drag coefficient of a sphere of radius  $a$  is given by Stokes' Law;

$$\beta = 6\pi\eta a \quad (3.2)$$

Where  $\eta$  is the fluid viscosity. Case B shows when pressure driven flow though a channel is used. Here Poiseuille flow is set up which is a parabolic flow profile going to no flow at the sides of the channel and a maximum in the center. The faster flow away from the channel walls induces a force on the particle towards the sides of the channel. This puts the particle into slower moving fluid slowing it down. However when the particle comes close to a surface the drag force increases according to Faxen's Law;

$$\beta = \frac{6\pi\eta a}{1 - \frac{9}{16}(a/h) + \frac{1}{8}(a/h)^3 - \frac{45}{256}(a/h)^4 - \frac{1}{15}(a/h)^5} \quad (3.3)$$

Where  $a$  is the particles radius and  $h$  is its height above the channel wall. This will increase the force on the particle significantly when it approaches the side of a channel (see figure 4.26).

### 3.4. RESULTS

---

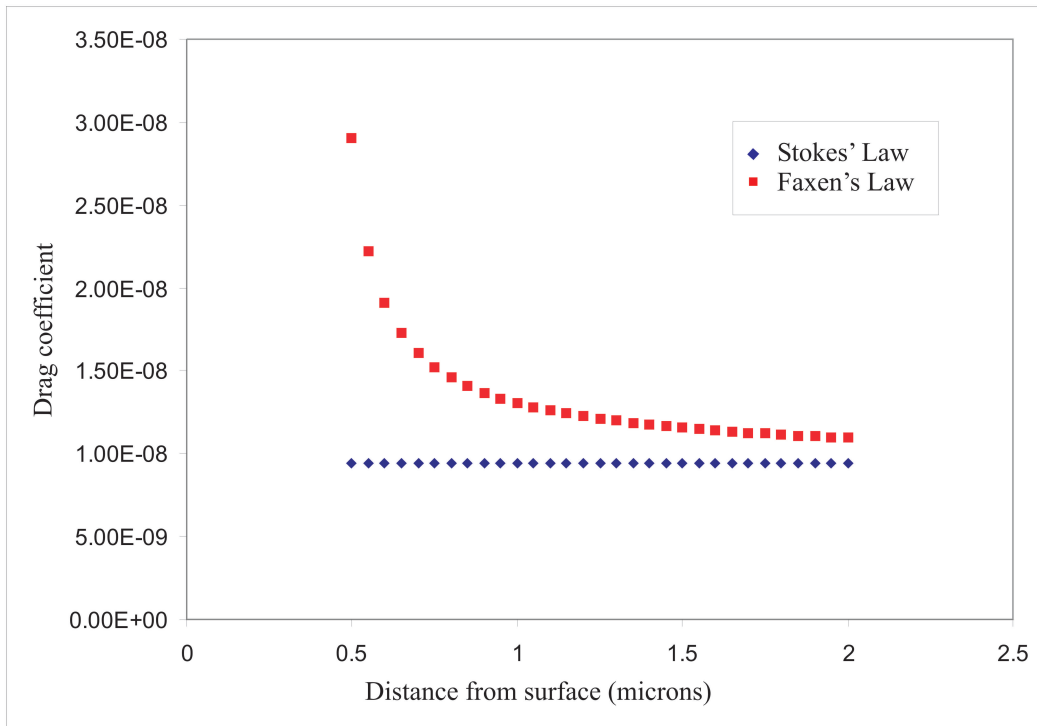


Figure 3.15: Comparison of the drag coefficient as calculated by Stokes' Law and Faxen's Law for a one micrometer diameter sphere in water. When the particle approaches the wall the difference become significant.

As the drag coefficient increases when the particle comes within a few microns of the surface, the force due to the fluid increases (see equation 3.2). This means that the particles going at the same velocity in the flow chamber are less likely to be guided than the particles on the moving stage, thus it is necessary not just to show that sorting can be done on a moving stage but in a flow chamber as it would have to be done in a medical application.

My first experiment was to show sorting of 2 and 5 micrometer diameter silica colloid in a microfluidic channel. Figures 3.16 A) and B) show frames

### 3.4. RESULTS

---

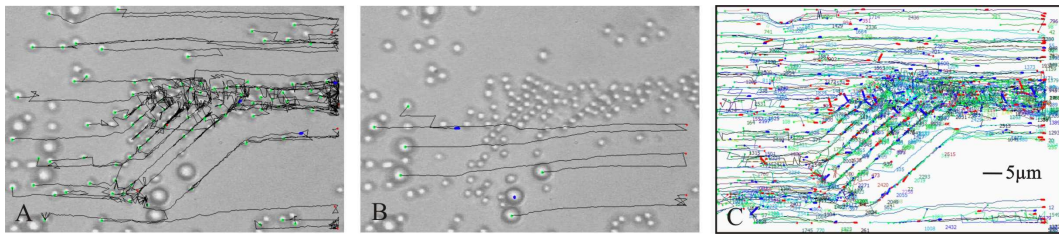


Figure 3.16: Optical sorting. Figures A and B are stills taken from a movie of optical sorting with lines overlayed by a particle tracking program. Figure A shows the paths of the 2 micrometer diameter colloid and figure B the 5 micrometer colloid. Figure C shows the tracks of the 2 micrometer colloid over a longer period of the movie, 1300 frames. It is clear the 2 micrometer colloid does not pass through a portion of the channel.

from a movie of the experiment overlayed with the tracks (drawn by a particle tracking program see section 1.2.1) of the 2 micrometer and 5 micrometer diameter colloid respectively from the first frame of the movie. Figure C shows just the tracks from a longer section of the movie, 1300 frames. It is clear that the 2 micrometer diameter colloid does not enter a section of the channel whilst the 5 micrometer colloid does showing sorting of the colloid over this area.

To find the limit of this process for sorting particles, it is not necessary to study both kinds of colloid but just to find the limits of guiding one type of colloid, whilst the other is not affected by the lattice. Using a simple straight through channel and a log pile optical pattern (similar to figure 3.13B), the percentage of particles guided by the optical lattice was recorded whilst varying the rate of flow for different angles between the lattice and the fluid flow (see figure 3.17).

I defined a particle as being guided if it was deflected by a vertical distance

### 3.4. RESULTS

---

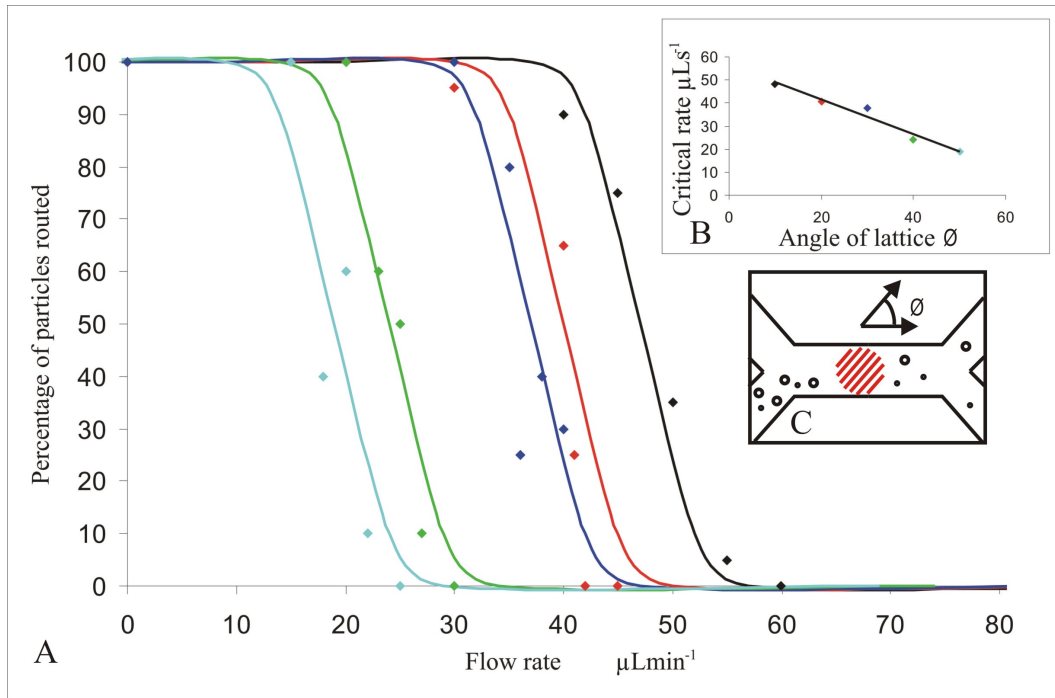


Figure 3.17: A) This graph shows the percentage of particles that are guided by the lattice for different flow rates and different lattice angles. B) Shows the critical flow rate at which 50 percent of particles are guided for the different lattice angles. C) Is a diagram of the channels that shows how the angle of the lattice is defined.

of  $10 \mu\text{m}$  over a certain horizontal distance defined by the field of view of the microscope  $100 \mu\text{m}$ . It can be seen that for a given angle of lattice the percentage of particles guided goes from 100 percent to zero as the fluid flow increases. As a measure of where this transition occurs, I defined the critical velocity as the velocity where 50 percent of the particles are guided. The critical flow rate for each angle is plotted in the insert. This shows that as the angle between the lattice and the flow increases, there is a roughly proportional decrease in the critical flow rate.

### 3.5. CONCLUSIONS

---

## 3.5 Conclusions

I have created a microfluidic flow chamber to demonstrate optical sorting in a real flow. I have looked at different fabrication techniques and found the most reliable to be a soft lithography approach where channels of PDMS are cast on a mold and then bonded to a glass slide.

I then demonstrated optical sorting in a microfluidic flow chamber and looked into the maximum velocity at which particles can be sorted and how it changes with the angle of the lattice. I have shown that sorting is possible in flow rates up to  $50\mu Lmin^{-1}$  with the lattice at  $10^\circ$  to the flow and that this flow rate decreases roughly proportionally as the angle of the lattice increases.

The main advantage of this technique, over the well established technique of flow cytometry, is that it does not need separate detection and manipulation mechanisms. Here the sorting is due to the cells inherent optical properties so no sample preparation is required. Although this method works well for small numbers of particles, it is limited by the interaction strength between the particles and light. Here we are using colloid; biological cells may be even less interactive and we still need several Watts of optical power to sort particles moving at relatively slow speeds. One solution to this may be to change to electrical forces. Using the technique of Light Induced Dielectrophoresis (LIDEP) (see section 4) a force similar to optical tweezing can be achieved with far less optical power. This may allow us to sort particles over a much larger area thus increasing the rate at which we can sort. Future work on optical cell sorting should focus two things. Firstly increasing the speed at which cells can be sorted with a given optical power. Secondly to use this sorting technique where only small populations of cells are required and where traditional methods are undesirable.

---

## BIBLIOGRAPHY

- [1] Holmes D., Morgan H., Green G.N. High throughput particle analysis: Combining dielectrophoretic particle focusing with confocal optical detection. *Biosensors and Bioelectronics*, 21 1621-1630 (2006).
- [2] Micro Total Analytical Systems, *μTAS* virtual journal, [www.elsevier.com](http://www.elsevier.com)
- [3] Lab-on-A-Chip website, [www.lab-on-a-chip.com](http://www.lab-on-a-chip.com)
- [4] David P. Schrum, Christopher T. Culbertson, Stephen C. Jacobson, and J. Michael Ramsey Microchip Flow Cytometry Using Electrokinetic Focusing. *Anal. Chem.*, 71 (19), 4173 -4177, 1999
- [5] Agilent, Lab-on-A-Chip products, [www.agilent.com](http://www.agilent.com)
- [6] Korda PT, Taylor MB, and Grier DG, Kinetically locked-in colloidal transport in an array of optical tweezers. *Physical Review Letters* 89, 128301 (2002).
- [7] MacDonald MP, Spalding GC, Dholakia K. Microfluidic sorting in an optical lattice. *Nature* Vol 426 p421-424.

## BIBLIOGRAPHY

---

- [8] Kosta L, Kasza K, Grier G. Sorting Mesoscopic Objects with Periodic Potential Landscapes: Optical Fractionation. *Physical Review E* 70, 010901(R) (2004).
- [9] MacDonald MP, Neale S, Paterson L, Richies A, Dholakia K, Spalding GC. Cell cytometry with a light touch: Sorting microscopic matter with an optical lattice. *Jouranl of Biological Regulators and Homeostatic Agents* 18 (2): 200-205 APR-JUN 2004.
- [10] Duffy DC, McDonald JC, Schueller OJA, Whitesides GM. Rapid prototyping of microfluidic systems in poly(dimethylsiloxane). *Analytical Chemistry*, 1998, 70 (23), 4974-4984.
- [11] Unger MA, Chou HP, Thorsen T, Scherer A, Quake SR. Monolithic Microfabricated Valves and pumps by Multilayer Soft Litography. *Science* Vol 288 7 April 2000 p113-116
- [12] Wheeler AR, Chah S, Whelan RJ, Zare RN. Poly(dimethylsiloxane) microfluidic flow cells for surface plasmon resonance spectroscopy. *Sensors and Actuators B* 98 (2004) 208-214.
- [13] Tung YC, Zhang M, Lin CT, Kurabayashi K, Skerlos SJ. PDMS-based opto-fluidic flow cytometer with two-color, multi-angle fluorescence detection capability using PIN photodiodes. *Sensors and Actuators B* 98 (2004) 356-367.
- [14] Studer V, Jameson R, Pellereau E, Pepin A, Chen Y. A microfluidic mammalian cell sorter based on fluorescence detection. *Microelectronic Engineering* 73-74 (2004) 852-857.
- [15] Svoboda, K, Block S.M., Biological Applications for Optical Forces. *Annual Review of Biophysical and Biomolecular Structure*, 23:247-85 (1994).

---

---

## CHAPTER 4

---

# Light Induced Dielectrophoresis (LIDEP)

## 4.1. INTRODUCTION

---

### 4.1 Introduction

An optical or electrical field gradient may induce forces in microscopic particles strong enough to move them. In optical tweezers, a focused laser beam is used to create a strong optical gradient that pushes the particle towards an area of high optical intensity. For neutral particles in a non-uniform electrical field the mechanism is termed dielectrophoresis with the electrical field gradients usually being created by microfabricated electrodes. Both research areas have proliferated in recent years [1, 2] giving physicists and biologists control over the micro world.

Recent work has shown a major step forward by using optical addressing of a photoconductive substrate to induce dielectrophoresis in a reconfigurable manner. This technique, termed light induced dielectrophoresis (LIDEP), allows us to create virtual electrodes controlled by the incident light pattern. The forces generated in this way may be up to five orders of magnitude greater than those generated directly by optical tweezers for the equivalent input power. This makes it possible to create vastly extended potential energy landscapes [3] and permit sorting over large areas.

#### 4.1.1 Dielectrophoresis (DEP)

The term dielectrophoresis (DEP) was first used by Pohl [4] in 1978 to describe the force felt by a neutral but polarisable particle when placed in a non-uniform electrical field. The force is due to the electrical dipole set up in the particle interacting with the electrical field that creates it. As the electrical field is non-uniform, the dipole across the particle experiences different forces on each side of the particle giving a net force in one direction (see figure 4.1).

The force due to dielectrophoresis is given by equation 4.1;

## 4.1. INTRODUCTION

---

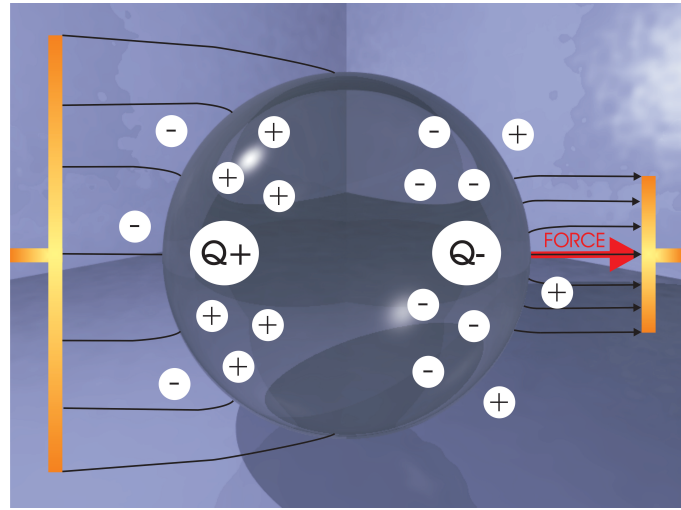


Figure 4.1: This diagram shows a particle in a non-uniform electrical field (black arrows) that is more polarisable than the medium it is in. The electrical field creates a larger dipole within the particle than in the medium resulting in a net dipole ( $Q_+$ ,  $Q_-$ ). As the field is not uniform different forces are exerted on each side of the particle resulting in a net force in one direction.

$$F_{DEP} = 2\pi r^3 \varepsilon_m \operatorname{Re}[K(\omega)] \nabla E^2 \quad (4.1)$$

Where  $F_{DEP}$  is the force due to dielectrophoresis,  $r$  is the radius of the particle,  $\varepsilon_m$  is the permittivity of the medium,  $\nabla E^2$  is the gradient of the square of the electrical field and  $\operatorname{Re}[K(\omega)]$  is the real part of the Clausius-Mossotti factor (see section 4.1.2).

## 4.1. INTRODUCTION

---

### 4.1.2 Clausius-Mossotti Factor

The Clausius-Mossotti factor is given by equation 4.2;

$$K(\omega) = \frac{\varepsilon_p^* - \varepsilon_m^*}{\varepsilon_p^* + 2\varepsilon_m^*} \quad (4.2)$$

Where  $\varepsilon_p^*$  and  $\varepsilon_m^*$  are the complex permittivities of the particle and medium respectively and are given by equation 4.3;

$$\varepsilon^* = \varepsilon - j\left(\frac{\sigma}{\omega}\right) \quad (4.3)$$

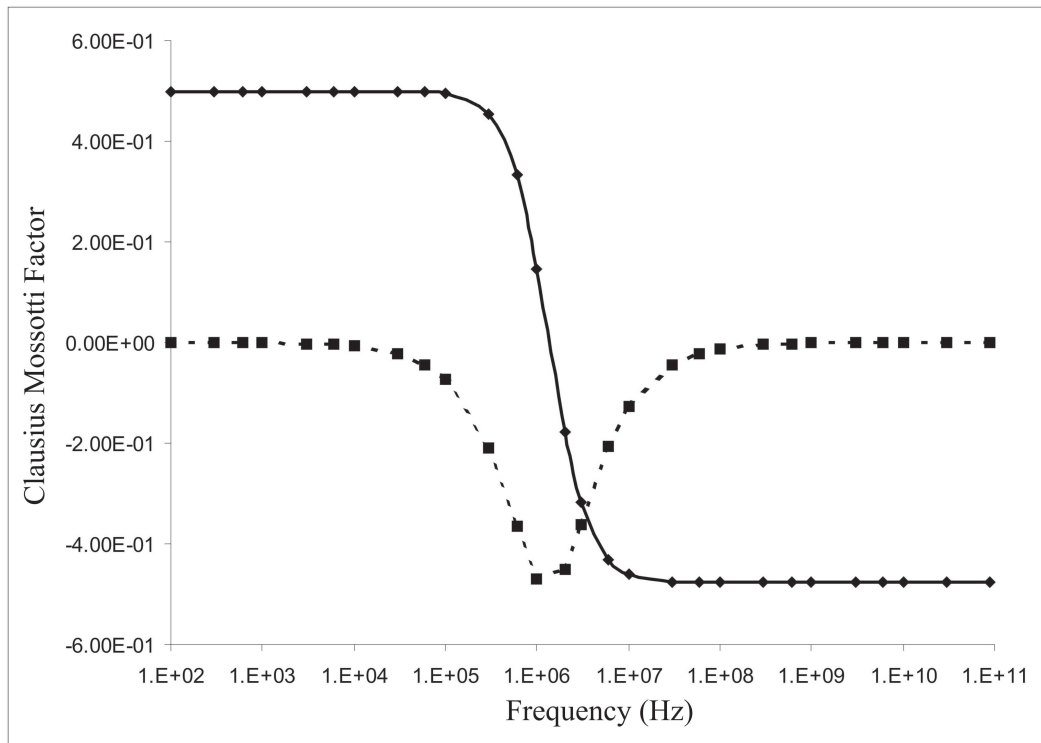


Figure 4.2: This graph shows the real (solid line) and imaginary (dashed line) parts of the Clausius-Mossotti factor for a 1 micrometer diameter latex sphere.

## 4.1. INTRODUCTION

---

Where  $\varepsilon$  is the permittivity,  $\sigma$  is the conductivity and  $\omega$  is the angular frequency of the applied AC. From this it is clear that the Clausius-Mossotti factor is frequency dependent and so is the force due to dielectrophoresis. Figure 4.2 shows the Clausius-Mossotti factor plotted for a one micrometer diameter latex sphere. It shows the characteristic positive force at low frequency turning into a negative force at high frequency for the case of a particle with lower permittivity than the medium surrounding it. The properties used for this graph were medium conductivity of  $2 \times 10^{-3} Sm^{-1}$  (a typical conductivity, see section 4.5.1) and relative permittivity 80 [5], particle relative permittivity 2.5 [7] and a conductivity calculated from equation 4.4;

$$\sigma_p = \sigma_{bulk} + \frac{2K_s}{r} \quad (4.4)$$

Where  $\sigma_{bulk}$  is the bulk conductivity of the particle material (here  $1 \times 10^{-16} Sm^{-1}$  [5]),  $K_s$  is the surface conductivity (here taken to be  $2 \times 10^{-9} S$  [8]) and  $r$  the particle radius. This formula shows that the particle conductivity is dominated by the surface conductivity in the case of small insulating particles.

### 4.1.3 Dielectrophoresis of cells

In optical tweezing, a latex colloid is a reasonable model for a biological cell as it is of higher refractive index than the medium, which is also the case for a cell. Therefore they may be expected to give similar dielectrophoretic responses. In reality, however, their actual dielectrophoretic responses are very different. Latex colloid experiences positive DEP at low frequency and negative DEP at high frequency while cells show the opposite, negative forces at low frequency and positive forces at high frequency. To simulate this response as before (see section 4.1.2) we would have to assume the cell has unrealistically high conductivity and permittivity. This contradiction is resolved when we

## 4.1. INTRODUCTION

---

consider the cell not as a homogeneous sphere as before, but more realistically as a shell of low conductivity material (the cell membrane) surrounding a higher conductivity medium (cytoplasm) as shown in figure 4.3. Cells are typically several microns across with the membrane being between 7 and 10 nanometers thick.

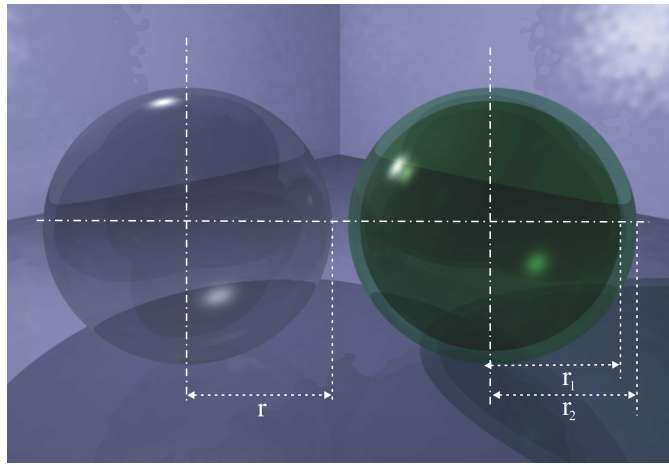


Figure 4.3: A latex colloid (left) can be thought of as a homogeneous sphere radius  $r$  but a cell (right) must be considered a shell of low conductive material, the membrane  $r_2$ , surrounding a higher conductivity medium, the cytoplasm  $r_1$ .

The Clausius-Mossotti factor can be modified for the single shell model by defining an effective permittivity for the shell calculated from the respective permittivities and radii of the cytoplasm and membrane (see equation 4.5)[9].

$$\varepsilon_{eff}^* = \varepsilon_2^* \frac{\left(\frac{r_2}{r_1}\right)^3 + 2\left(\frac{\varepsilon_1^* - \varepsilon_2^*}{\varepsilon_1^* + 2\varepsilon_2^*}\right)}{\left(\frac{r_2}{r_1}\right)^3 - \left(\frac{\varepsilon_1^* - \varepsilon_2^*}{\varepsilon_1^* + 2\varepsilon_2^*}\right)} \quad (4.5)$$

Where  $\varepsilon_{eff}$  represents the permittivity of the cell,  $\varepsilon_1$  and  $r_1$  the permittivity and radius of the cytoplasm,  $\varepsilon_2$  and  $r_2$  the permittivity and radius of the membrane. This effective permittivity can then be used instead of the particles

## 4.1. INTRODUCTION

---

permittivity in equation 4.2 to give the Clausius-Mossotti factor and hence the frequency response for the cell. Figure 4.4 shows the real part of the Clausius-Mossotti factor plotted against frequency for typical values for a red blood cell (these values come from reference [2] and as they vary over several orders of magnitude, to demonstrate the effect of different conductivities, some of the values are not realistic). The relative permittivities of the cytoplasm, shell and surrounding medium are taken as 60, 4.4 and 78 respectively. The radius of the cell is taken as 10 microns with a 10nm thick membrane. In graph A the conductivities of the core and medium are fixed as 1 and  $0.02 \text{ Sm}^{-1}$  and the conductivity of the membrane is varied from  $1 \times 10^{-8}$  to  $1 \times 10^{-5} \text{ Sm}^{-1}$ . This shows that for low membrane conductivities there is negative DEP at low frequencies and positive DEP at high frequencies compared to a higher conducting membrane that gives positive DEP for all frequencies. Graph B shows the conductivity of the membrane set as  $1 \times 10^{-8} \text{ Sm}^{-1}$ , the conductivity of the medium set as  $0.02 \text{ Sm}^{-1}$  and the conductivity of the cytoplasm varied from 0.01 to  $100 \text{ Sm}^{-1}$ . This shows that the size of the positive DEP peak is dependent on the conductivity of the cytoplasm with higher conductivity giving a larger peak. Graph C shows the conductivity of the cytoplasm set as  $1 \text{ Sm}^{-1}$ , the conductivity of the membrane set as  $10 \times 10^{-8} \text{ Sm}^{-1}$  and the conductivity of the medium varied from 0.001 to  $10 \text{ Sm}^{-1}$ . This shows that the frequency at which the dielectrophoretic force crosses from being negative to positive changes with medium conductivity with the crossover frequency being lower with lower medium conductivity.

These graphs clearly show that different cell types with different conductivities will feel different dielectrophoretic forces which can then be used to sort the cells. It is possible to sort very different cells such as red and white blood cells and it may be possible to sort even very similar cells such as red

## 4.1. INTRODUCTION

---

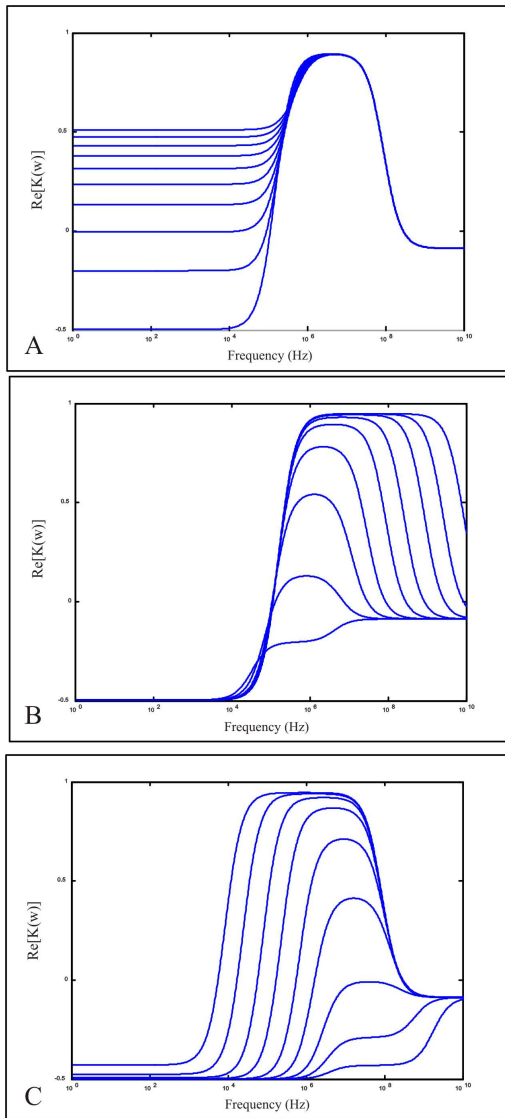


Figure 4.4: These graphs show the real part of the Clausis-Mossotti factor for a red blood cell (RBC) using a single shell model for various conductivities (see text).

blood cells of different type (O, A, B, etc).

## 4.1. INTRODUCTION

---

### 4.1.4 Light Induced Dielectrophoresis

From equation 4.1, we can see that the force due to dielectrophoresis is proportional to the gradient of the square of the electrical field. To give a large electrical field gradient we need an area of large electrical field next to an area of low electrical field. Usually the large electrical field is generated by dropping a voltage over a short distance. For example a voltage of just 10V can give an electrical field of  $1 \times 10^6 \text{ V/m}$  if dropped over a 10 micrometer gap. Such micron scale gaps are easily achievable by photolithographic techniques. A recent advance in the field, however, has shown that it is possible to create the electric field gradients without the need of patterned electrodes. Instead a photoconductive layer (here amorphous silicon, a-Si) is sandwiched between two conducting plates that have the AC voltage passed across them (see figure 4.5). The photoconductor is illuminated in the desired pattern, causing a pattern of higher conductivity that acts as a "virtual electrode" [3, 10]. Where the chamber is dark, and the a-Si is more resistive, a higher proportion of the voltage is dropped across the photoconductor than where it is light. This changes the electric field just above the insulator for the illuminated area, giving a horizontal electrical field gradient that can be used for dielectrophoresis.

This manipulation technique has the advantage over conventional dielectrophoresis that we can change the shape of the electrodes continuously just by changing the light pattern. This is also possible with optical tweezers, but LIDEP has the advantage of needing less optical power. Particle manipulation is achievable with micro Watts instead of the milli Watt power required for optical tweezing. This makes it possible to control many more particles at one time and over a much larger area with a given power [3].

## 4.1. INTRODUCTION

---

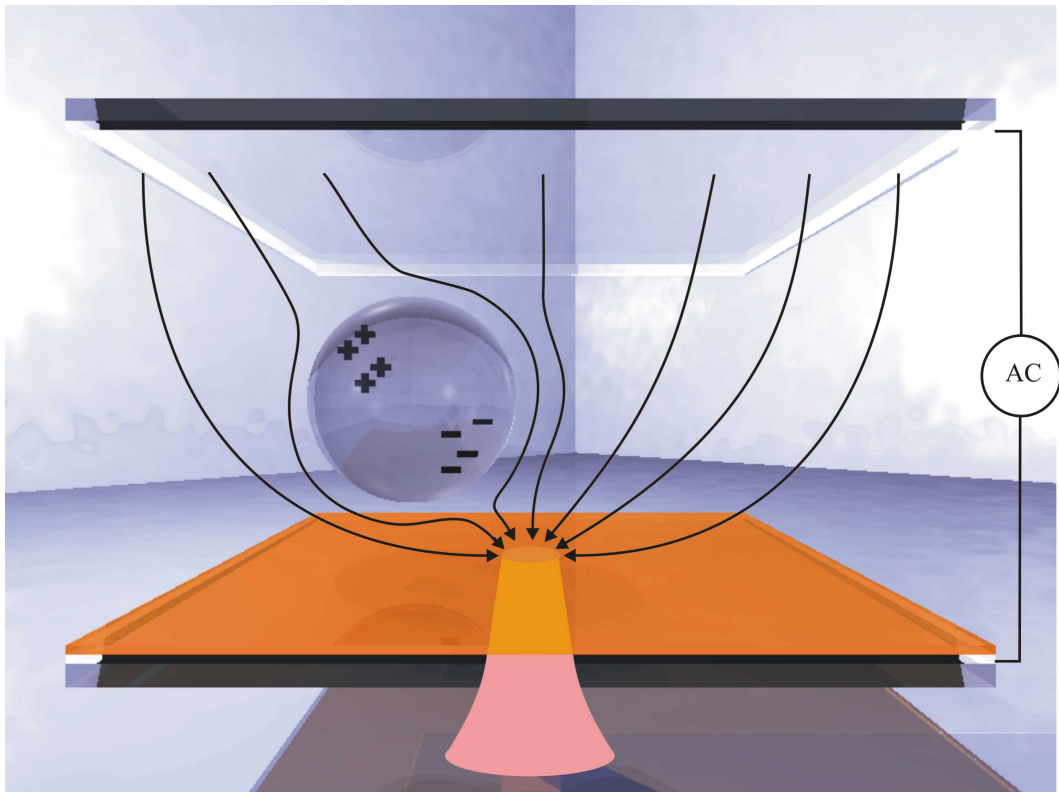


Figure 4.5: This figure shows a diagram of a LIDEP chamber. An AC voltage is placed across the wires that are attached to the ITO layers creating a vertical electric field in the chamber. This is then patterned horizontally by illuminating the a-Si creating a more conductive "virtual electrode". The resulting horizontal and vertical electric field gradients attract the particles to the illuminated spot by dielectrophoresis.

### 4.1.5 State of the art

The most common application for cell manipulation is cell sorting. At the present the most common cell sorting technique is Fluorescence-Activated Cell Sorting (FACS) as described in section 3.1.1. Although this is a fast and

## 4.1. INTRODUCTION

---

widespread technique there is considerable interest in finding ways to supplement it. Optical tweezers are one technique being researched as a method to sort cells (see section 3). As a laser can be focused to a spot in three dimensions this offers 3D control of the particles. Also the position the force is applied to can be changed by changing the input light pattern, thus offering continuous control. However optical tweezing requires high light intensities which increases the size and cost of the laser needed. As we have seen the dielectrophoretic force a particle experiences depends on its intrinsic properties and so can also be used for sorting. This has been shown (using metal electrode arrays to create the field gradients) to sort particles [17], cells [18, 19, 2, 20] and to characterise cells [21]. However, for the force to be very different, the intrinsic properties of the cells must be very different. By labeling the cells with polarisable labels the difference in force felt can be increased, allowing the fast separation of cells ( $1 \times 10^4$  cells per second [22]). Dielectrophoresis with metal electrodes does not offer some of the versatility of optical sorting as it lacks three dimensional control and continuous controllability. Cell sorting has also been shown with LIDEP [3, 16]. This gives the advantage of continuous control making the technique more versatile. The work in this chapter describes simulations and experiments designed to increase our understanding of LIDEP. They center on finding the size of electrical trap produced by an input light pattern, a piece of information essential in designing a LIDEP cell sorting device.

## 4.2. SIMULATION

---

### 4.2 Simulation

#### 4.2.1 COMSOL and the Finite Element Method

I performed numerical models in COMSOL to find the force felt by the colloid in the LIDEP chamber. From equation 4.1 it is clear that to find the force we need to know the gradient of the square of the electrical field caused by the optical spot on the photoconductive layer. COMSOL uses the Finite Element Method (FEM) to simulate the physical response of the body to be analysed.

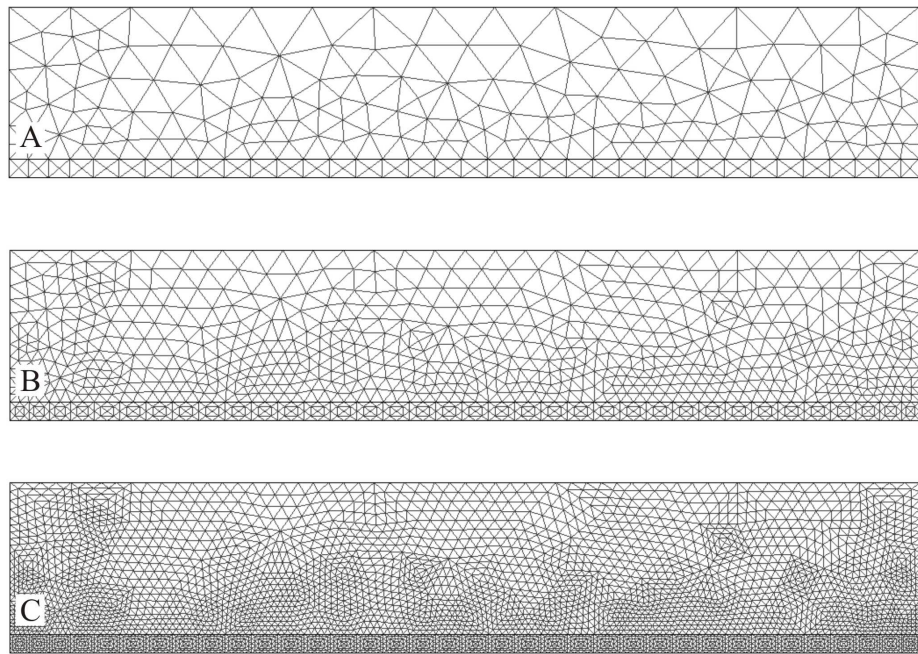


Figure 4.6: The mesh used in Finite Element Method calculations. The basic mesh created by COMSOL is shown in A with the mesh refined once shown in B and refined twice shown in C.

Here the body is split into small, usually non-Cartesian elements, each of

## 4.2. SIMULATION

---

which has a set of Partial Differential Equations (PDEs) attributed to it that describe its physical properties and boundary conditions. These equations are then solved simultaneously to predict the behavior of each element. The relative size of the elements compared to the body can be seen in figure 4.6. Figure 4.6 has no scale bar as it would be the result of any body of these proportions. The body is split into two subdomains which can represent two different materials. The finite elements are smaller in the smaller subdomain and vary in size in the larger subdomain. This is so they can match the small finite elements at the border with the smaller subdomain, where variations in the calculated fields are likely to happen over a smaller distance. This reduces the number of elements needed and hence the computational time. This is significant for LIDEP where the subdomains may vary from 20nm to 50 $\mu\text{m}$  in thickness.

### 4.2.2 Maxwell's equations and the The Quasi Static Approximation

COMSOL is split into different sections called "application modes" each of which solves a different set of PDEs depending on the application. The application mode chosen was the "In-Plane Electric Currents" mode from the "Quasi Statics, Electric" section of the "Electromagnetics Module". As in all the application modes in the Electromagnetics module, this solves Maxwell's equations along with boundary conditions to find the electromagnetic fields. Maxwell's equations are given by equations 4.6 to 4.9;

$$\nabla \times \overline{H} = \overline{J} + \frac{\partial \overline{D}}{\partial t} \quad (4.6)$$

## 4.2. SIMULATION

---

$$\nabla \times \bar{E} = -\frac{\partial \bar{B}}{\partial t} \quad (4.7)$$

$$\nabla \cdot \bar{D} = \rho \quad (4.8)$$

$$\nabla \cdot \bar{B} = 0 \quad (4.9)$$

Where  $\bar{E}$  and  $\bar{H}$  are the respective electric and magnetic field intensities,  $\bar{D}$  and  $\bar{B}$  are the respective electric and magnetic flux densities,  $\bar{J}$  is the current density and  $\rho$  is the electric charge density. Due to the quasi static approximation (that will be justified later, see section 4.2.3) we can put  $\frac{\partial D}{\partial t} = 0$  and  $\frac{\partial \bar{B}}{\partial t} = 0$ . These simplify equations 4.6 and 4.7 to;

$$\nabla \times \bar{H} = \bar{J} \quad (4.10)$$

$$\nabla \times \bar{E} = 0 \quad (4.11)$$

This means we can write the electric field in terms of the electric potential only  $\bar{E} = -\nabla V$ . Combining this with the constitutive relation  $\bar{D} = \epsilon_0 \epsilon_r \bar{E}$  and equation 4.8 gives  $-\nabla(\epsilon_0 \epsilon_r \nabla V) = \rho$ . Equation 4.12 is the time harmonic equation of continuity and using this to substitute out  $\rho$  we get equation 4.13.

$$\nabla \bar{J} = \nabla \cdot (\sigma \bar{E} + J^e) = -j\omega \rho \quad (4.12)$$

$$-\nabla((\epsilon_0 \epsilon_r j\omega + \sigma) \nabla V - J^e) = 0 \quad (4.13)$$

Where  $\omega$  is the angular frequency,  $\sigma$  is the conductivity and  $J^e$  is the external current density. Putting this equal to a current source term  $Q_j$  and

## 4.2. SIMULATION

---

multiplying both sides by a thickness  $d$  gives the general equation to be solved, equation 4.14.

$$-\nabla \cdot d((\varepsilon_0 \varepsilon_r j\omega + \sigma) \nabla V - J^e) = dQ_j \quad (4.14)$$

For LIDEP there are no internal source terms so  $Q_j = 0$ .

### 4.2.3 The quasi static approximation

The quasi static approximation neglects the fact that changes in electromagnetic fields do not vary in phase with changes in sources but lag behind them. Using this assumption it is possible to calculate the electromagnetic fields by considering stationary currents at every instant [6]. The crucial criterion for the quasi static approximation to be valid is that the currents and electromagnetic fields vary slowly. For this to be true the size of the structure must be small compared to the wavelength. The wavelength for a frequency of 2MHz (the largest frequency used) is given by equation 4.15;

$$\lambda = \frac{c}{\nu} = \frac{3 \times 10^8}{2 \times 10^6} = 150m \quad (4.15)$$

As this wavelength is much larger than our structure, we may use the quasi static approximation, which allows us to put  $\frac{\partial D}{\partial t} = 0$ .

Another assumption that may be made when considering electric currents in the quasi static approximation is that the coupling between the electrical and magnetic fields can be ignored. For this to be valid the skin depth must be much larger than the geometry. The skin depth is given by 4.16;

$$\delta = \frac{1}{\sqrt{\pi \mu_0}} \sqrt{\frac{\rho}{\mu_r \nu}} \quad (4.16)$$

## 4.2. SIMULATION

---

Where  $\delta$  is the skin depth,  $\mu_0$  is the permeability of free space,  $\rho$  is the resistivity,  $\mu_r$  is the relative permeability, and  $\nu$  is the frequency. At a frequency of  $2 \times 10^6$  Hz this gives the skin depths shown in table 4.1;

Table 4.1: Conductivities and Skin Depth

Material	Conductivity( $Sm^{-1}$ )	Skindepth(m)
ITO	$1 \times 10^5$	0.0011
a-Si (Light)	$1 \times 10^{-2}$	3.6
a-Si (Dark)	$1 \times 10^{-4}$	35.6
SiNx	$2.5 \times 10^{-10}$	$2.3 \times 10^4$
H2O	$1 \times 10^{-3}$	11

The smallest skin depth is 1.1mm which is still much larger than the geometry being considered. This shows this assumption is valid and so we can put  $\frac{\partial \overline{B}}{\partial t} = 0$ .

Once the application mode to be used has been selected the geometry can be defined. This is done by drawing boxes called subdomains to represent the different materials. Once the layers have been defined it is necessary to set the boundary conditions.

### 4.2.4 Boundary conditions

Of equal importance to the equations used are the boundary conditions that are set. In this model, the lowest boundary was set at an electric potential of 16V and the top boundary was set to ground. All of the vertical boundaries were set to electric insulation. This boundary condition sets the component of the electrical current normal to the boundary to zero. The model is made wide enough so that this imposed direction of the electrical fields does not

## 4.2. SIMULATION

---

effect the fields that we wish to study at the center of the simulation. This was checked by running a model with twice the width which gave no variation. After setting the boundary conditions we go on to set the physical properties of the materials.

### 4.2.5 Subdomain settings

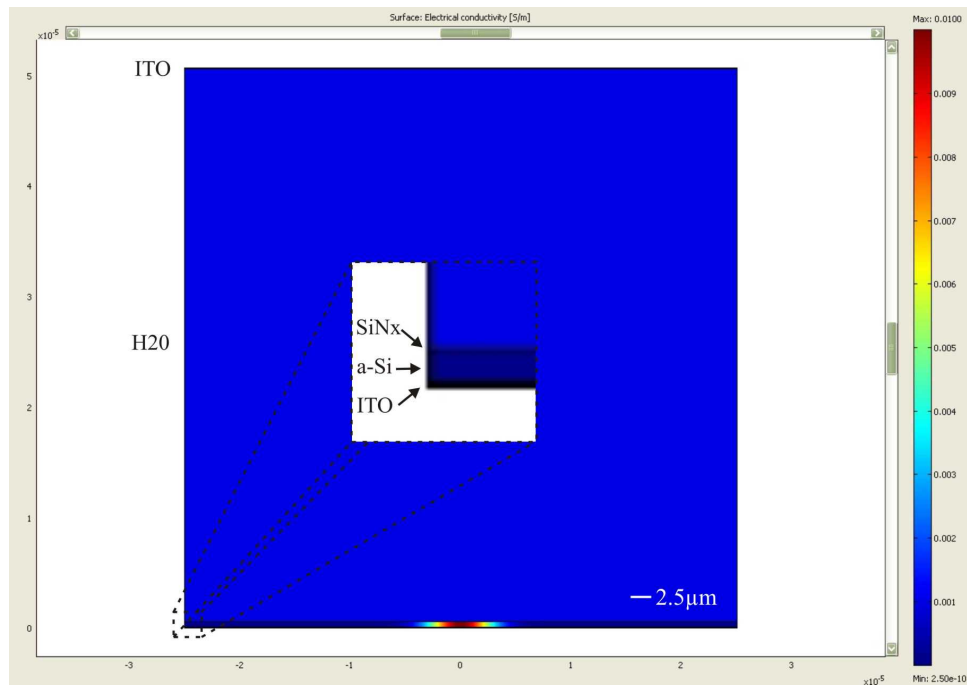


Figure 4.7: The conductivities are shown with the ITO layers suppressed as their conductivity is so high that plotting it would not allow us to see the other conductivities.

As we have used the constitutive relationship  $D = \varepsilon_0 \varepsilon_r E$  we need to enter the conductivity and the relative permittivity of each material. The values used are shown in table 4.2.

In these simulations I have modeled the photoconductive response of the

## 4.2. SIMULATION

---

Table 4.2: Conductivities and Permittivities

<i>Material</i>	<i>Conductivity(<math>Sm^{-1}</math>)</i>	<i>RelativePermittivity</i>
ITO	$1 \times 10^5$	3.84
a-Si (Light)	$1 \times 10^{-2}$	11.68
a-Si (Dark)	$1 \times 10^{-4}$	11.68
SiNx	$2.5 \times 10^{-10}$	7.5
H2O	$1 \times 10^{-3}$	80.2

a-Si as a gaussian change from its dark conductivity of  $1 \times 10^{-4} Sm^{-1}$  to its light conductivity  $1 \times 10^{-2} Sm^{-1}$  [10]. This gives the conductivities shown in figure 4.7. This simulation has a gaussian distribution in the conductivity of the a-Si with a sigma value of  $2.1\mu m$  which corresponds to a Full Width Half Maximum (FWHM) of  $5\mu m$ .

### 4.2.6 Checking the simulated potential drop against circuit analysis

In the quasi static application mode one of the scalar variables that can be set is the frequency of the applied potential. In this simulation it was set to  $2 \times 10^6$  Hz as this is the frequency used in the experiments detailed later (see section 4.5.3). The frequency is important as it can cause the reactance to dominate over the resistance for some of the layers, resulting in very different impedances than would be experienced at DC. The simulations took 25s to run and to check the outcome against expectation, the simulated electrical potential was compared to a circuit analysis. The simulated potentials are shown in figure 4.8.

## 4.2. SIMULATION

---

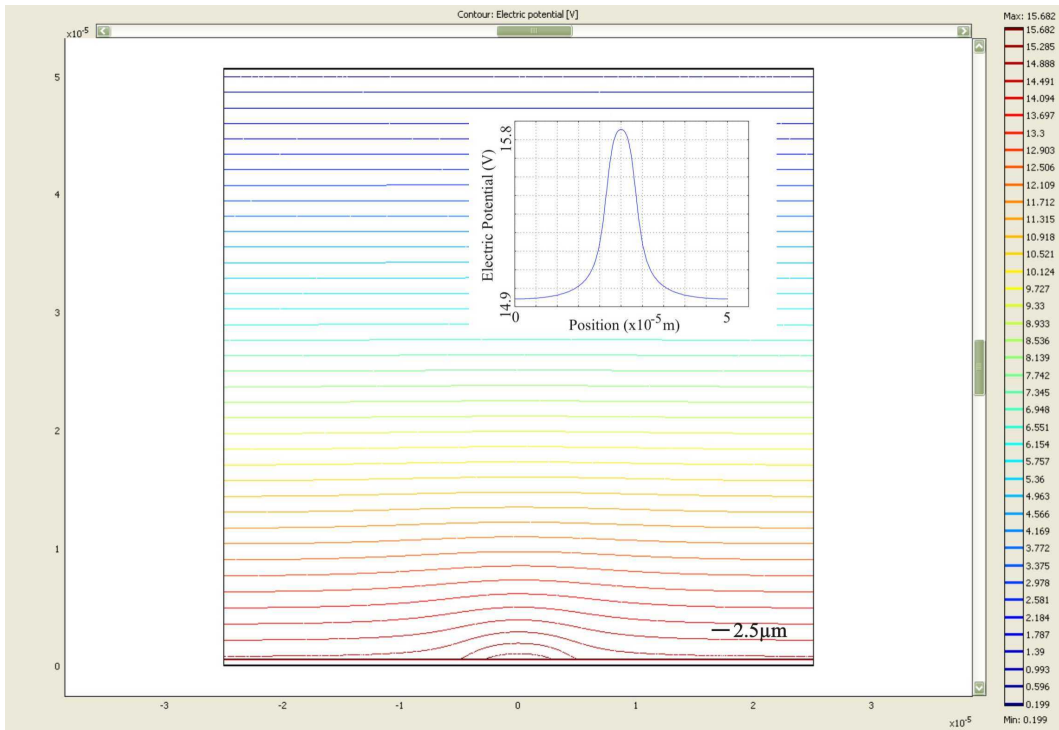


Figure 4.8: The contours of this figure plot lines of equal potential in the liquid. They show a higher potential drop in the center caused by the photoconductive spot. The inset graph shows the potential at the lower water boundary. This shows that 14.9 V are dropped over the liquid where the a-Si:H is dark and 15.8V are dropped over the liquid where the a-Si:H is illuminated.

Figure 4.8 shows the calculated electrical potential in the liquid. To show the exact potential drop across the liquid a cross section has been plotted that highlights the potential across a horizontal line at the lower boundary of the water. This figure shows that the potential drop across the liquid where the a-Si is in the dark is 14.9V and where it is fully illuminated it is 15.8V. A comparative circuit analysis was performed as shown in figure 4.9.

## 4.2. SIMULATION

---

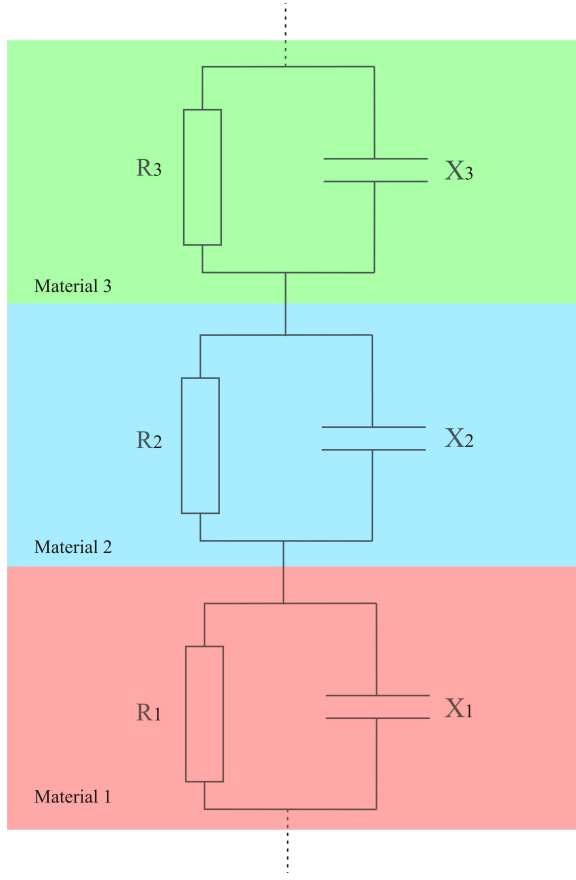


Figure 4.9: The electrical circuit for the LIDEP chamber consists of five layers of material each of which have a resistance and a capacitance that will act in parallel. When all five layers are considered in series the potential drop over each layer can be found.

Figure 4.9 shows the effective circuit. Each material has a resistance and a capacitance that act in parallel. When all five layers are considered in series the voltage drop over each layer can be found. A  $50\mu m$  square section is considered so that the resistance of each layer can be found from the formula  $R = \frac{\rho l}{A}$  where  $\rho$  is the resistivity,  $l$  the thickness of the layer and  $A$  the area. The reactance is found from  $X = \frac{1}{2\pi\nu C}$  where  $\nu$  is the frequency and  $C$  is the capacitance. The

## 4.2. SIMULATION

---

capacitance is given by  $C = \varepsilon_0 \varepsilon_r \frac{A}{d}$  where  $\varepsilon_0$  is the permittivity of free space,  $\varepsilon_r$  is the relative permittivity,  $A$  is the area and  $d$  is taken as the thickness of the layer. Using these equations the values in tables 4.3 and 4.4 were calculated.

Table 4.3: Impedance and potential drop across layers, no illumination

Material	Resistance ( $\Omega$ )	Reactance ( $\Omega$ )	Impedance ( $\Omega$ )	Potential (V)
ITO	$4 \times 10^{-4}$	$9.37 \times 10^4$	$4 \times 10^{-4}$	$2.95 \times 10^{-9}$
a-Si (dark)	$2 \times 10^6$	$1.54 \times 10^5$	$1.43 \times 10^5$	<b>1.05</b>
SiNx	$3.2 \times 10^{10}$	$9.59 \times 10^3$	$9.59 \times 10^3$	$7.08 \times 10^{-2}$
H20	$2 \times 10^7$	$2.24 \times 10^6$	$2.02 \times 10^6$	<b>14.9</b>
ITO	$4 \times 10^{-4}$	$9.37 \times 10^4$	$4 \times 10^{-4}$	$2.95 \times 10^{-9}$

Table 4.4: Impedance and potential drop across layers, with illumination

Material	Resistance ( $\Omega$ )	Reactance ( $\Omega$ )	Impedance ( $\Omega$ )	Potential (V)
ITO	$4 \times 10^{-4}$	$9.37 \times 10^4$	$4 \times 10^{-4}$	$3.13 \times 10^{-9}$
a-Si (light)	$2 \times 10^4$	$1.54 \times 10^5$	$1.77 \times 10^4$	<b><math>1.39 \times 10^{-1}</math></b>
SiNx	$3.2 \times 10^{10}$	$9.59 \times 10^3$	$9.59 \times 10^3$	$7.51 \times 10^{-2}$
H20	$2 \times 10^7$	$2.24 \times 10^6$	$2.02 \times 10^6$	<b>15.8</b>
ITO	$4 \times 10^{-4}$	$9.37 \times 10^4$	$4 \times 10^{-4}$	$3.13 \times 10^{-9}$

These tables show the potential drop across the H20 when the a-Si is not illuminated is 14.9V and when illuminated is 15.8V. This agrees with the simulated values shown in figure 4.8 and proves that the simulation is consistent with what we expect.

## 4.2. SIMULATION

---

### 4.2.7 Plotting the electrical fields

Once the simulation has calculated the potentials we can use post-processing to plot the electrical fields. We wish to find  $\nabla \overline{E^2}$  and how it varies throughout the liquid. However to understand why this varies as it does it is first necessary to consider the electrical fields in the a-Si:H. The electrical field is split into its two vector components  $\overline{E} = \overline{E}_x + \overline{E}_y$ . We have imposed a conductivity Gaussian on the a-Si:H varying between  $1 \times 10^{-4}$  to  $1 \times 10^{-2} Sm^{-1}$ . This creates a change in resistivity given by the inverse of a Gaussian as shown by the squares in figure 4.10.

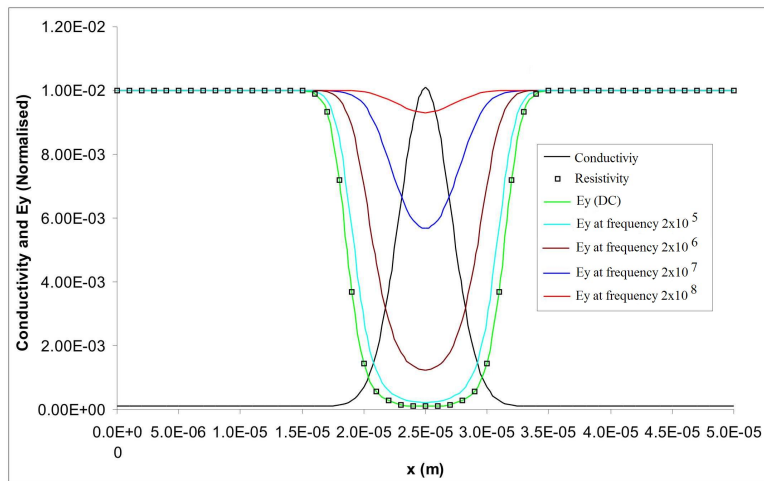


Figure 4.10: The conductivity of the a-Si:H is plotted against position in  $x$ . The resistivity and  $E_y$  at various frequencies are also plotted and normalised to compare them with the conductivity and each other. Note that the peak gradient of the resistivity (and hence the peak gradient of  $E_y$ ) is in a different position to the peak gradient of the conductivity.

## 4.2. SIMULATION

---

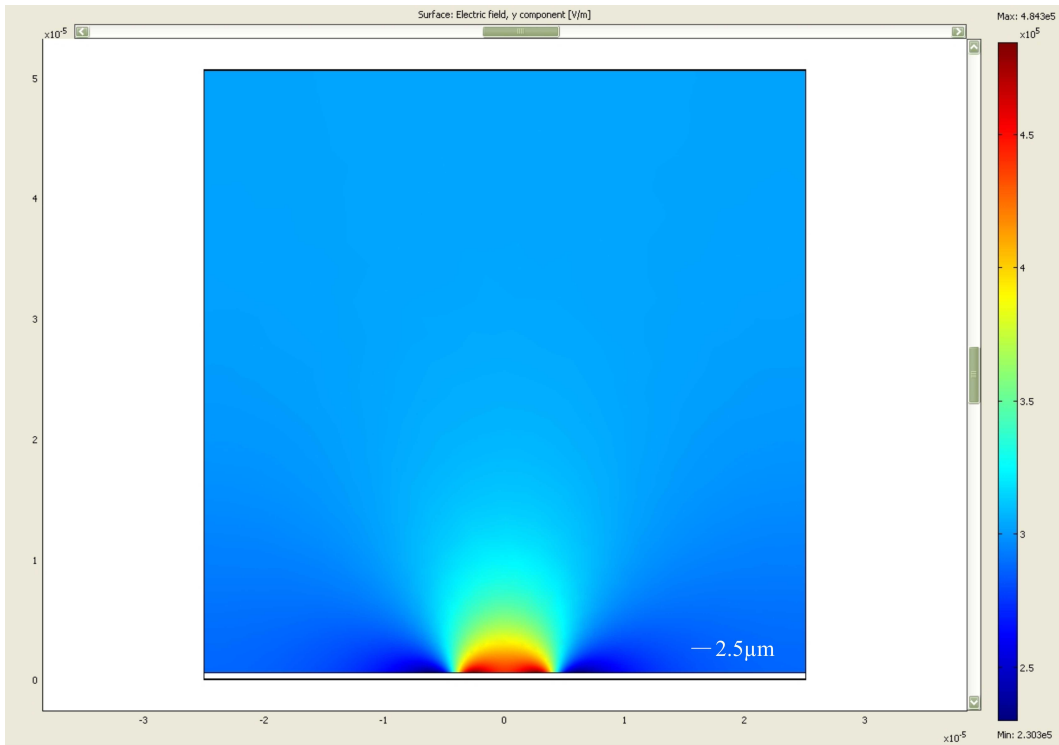


Figure 4.11: The y component of the electrical field ( $\bar{E}_y$ ).

At low frequencies the potential drop across the a-Si:H (and hence  $\bar{E}_y$  in it) is governed by the resistance and thus follows the form of the resistivity. At higher frequencies the reactance dominates and the gaussian in resistivity has less of an effect. This causes the peak gradients in  $\bar{E}_y$  to move closer to the center of the conductive spot.

Where the potential drop is greatest over the a-Si:H it is smallest over the liquid. Thus as  $\bar{E}_y$  is a minimum in the center of the conductive spot in the a-Si:H, it is a maximum in the liquid vertically above this spot (see figure 4.11). This also creates an electrical field in the x direction shown in figure 4.12.

## 4.2. SIMULATION

---

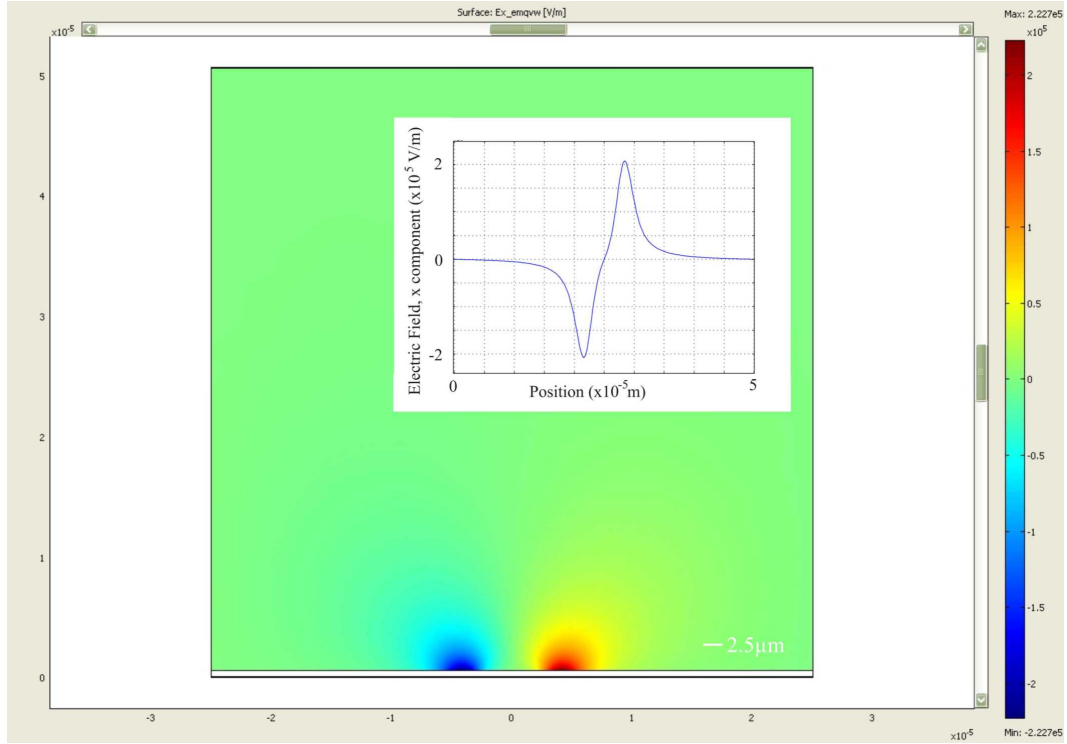


Figure 4.12: The x component of the electrical field ( $\overline{E}_x$ ). The inlaid graph shows  $\overline{E}_x$  plotted for a line at the lower boundary of the liquid.

The square of the electrical field is shown in figure 4.13. This is calculated as  $\overline{E}^2 = \overline{E}_x^2 + \overline{E}_y^2$  and is dominated by the y component as the maximum  $E_y$  is  $5 \times 10^5 \text{ V m}^{-1}$  where the maximum  $E_x$  is only  $2.2 \times 10^5 \text{ V m}^{-1}$ . However the  $E_x$  component does impose some structure on  $E^2$  giving two maxima close to the liquid to SiNx interface but only one maximum further from the interface. The units that are given in the title of this figure are  $m^2 kg^2 / (s^6 A^2)$  which is equivalent to  $V^2 / m^2$ .

## 4.2. SIMULATION

---

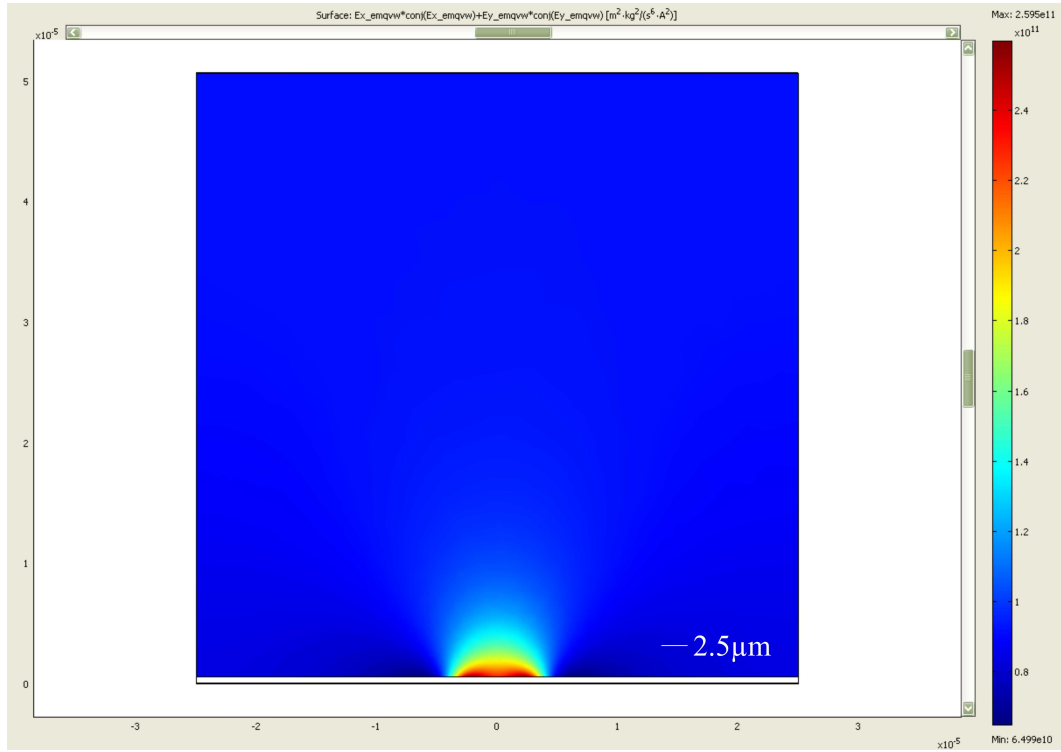


Figure 4.13: The square of the electrical field ( $\overline{E}^2$ ).

### 4.2.8 Plotting the gradient of the square of the electrical field

The gradient of the square of the electrical field is again split into x and y components so that we can see in which directions the gradients are in, and hence which direction the forces they cause act. The x component is shown as a colour map in figure 4.14 with arrows plotting both the x and y components. The length of the arrows is proportional to the magnitude of the gradient and hence to the DEP force a particle would experience.

This data can then be used to calculate the DEP force from equation 4.1. Cross sectional lines of the x component are plotted at heights of  $0.5\mu m$  (blue line) and  $2.5\mu m$  (green line) from the interface between the liquid and the SiNx. The units that are given in the title of this figure are  $mkg^2/(s^6A^2)$

## 4.2. SIMULATION

---

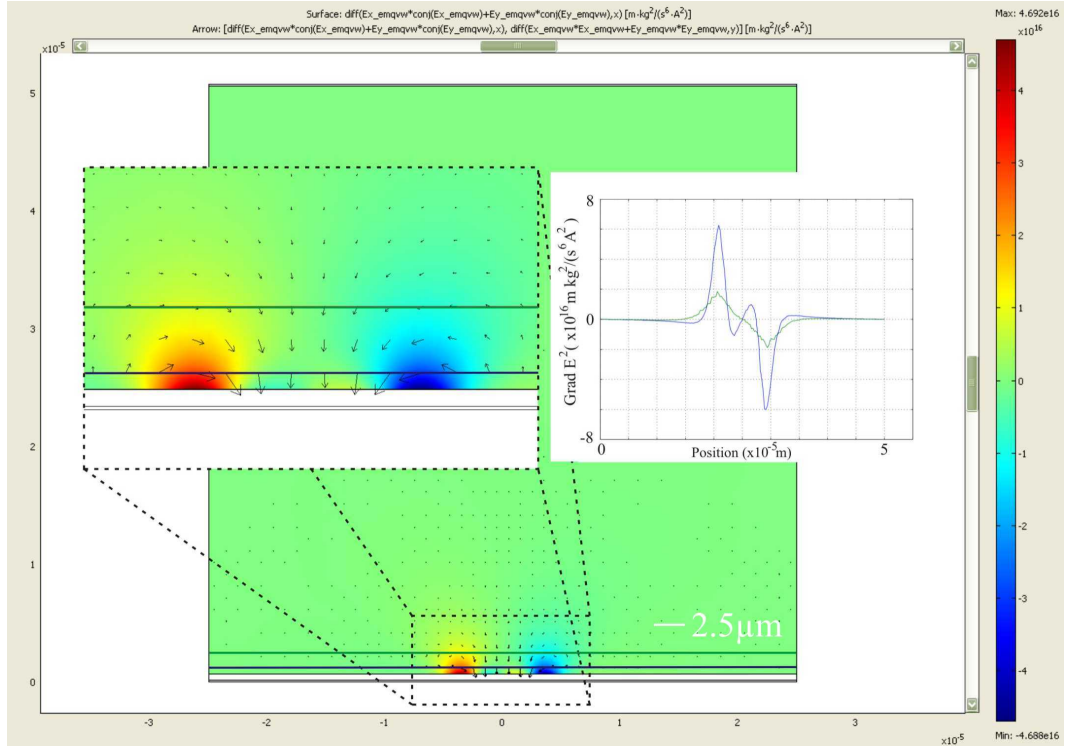


Figure 4.14: The gradient of the square of the electrical field in the x direction ( $\nabla \bar{E}^2, x$ ) plotted as a surface with arrows plotting both the x and y components.

which is equivalent to  $V^2/m^3$ . These lines are chosen as to represent the force on a  $5\mu m$  diameter colloid as discussed later in section 4.5.3. The resulting graphs are shown inlaid in figure 4.14 and show maximum and minimum peaks  $4\mu m$  from the center of the illuminated area. These correspond to peaks in force in different directions with a force in the positive x direction defined as a positive force. The green line representing the gradients  $2.5\mu m$  from the surface has a fairly linear section between its maximum and minimum peaks. However the blue line representing  $0.5\mu m$  from the surface has smaller negative peaks at  $1.5\mu m$  from the center of the illumination. These would correspond

## 4.2. SIMULATION

---

to a force away from the center of the illuminated spot and the formation of a ring trap (if working at a frequency that gives positive DEP). The position of the peak forces is a good measure of how large an area the physical force is felt over and what resolution (how close together we could put these peaks) could be achievable with LIDEP. As we have seen this is dominated by where the peak gradient in the resistivity (not the conductivity) is and it is this that must be considered when designing a LIDEP system. How this corresponds to experimental results will be discussed later (see section 4.5.3).

In summary this chapter has shown two things. Firstly that the numerical models and circuit analysis match. Secondly that the peak force corresponds to the peak gradient in resistance of the a-Si:H when the AC and DC components of the resistance are taken into account.

## 4.3. FABRICATION

---

### 4.3 Fabrication

#### 4.3.1 Dielectrophoresis chamber

To allow the comparison of Light Induced Dielectrophoresis (LIDEP) with conventional dielectrophoresis, a simple dielectrophoresis chamber was made. The shape of a cross with a gap in the center was chosen, a shape that is widely used in the literature as it clearly shows the difference between positive and negative dielectrophoresis.

The pattern was created in resist on an ITO coated glass cover slip using electron beam (e-beam) lift off lithography. Gold was subsequently evaporated onto the sample and the resist removed to leave the pattern in gold on the cover slip (see figure 4.15).

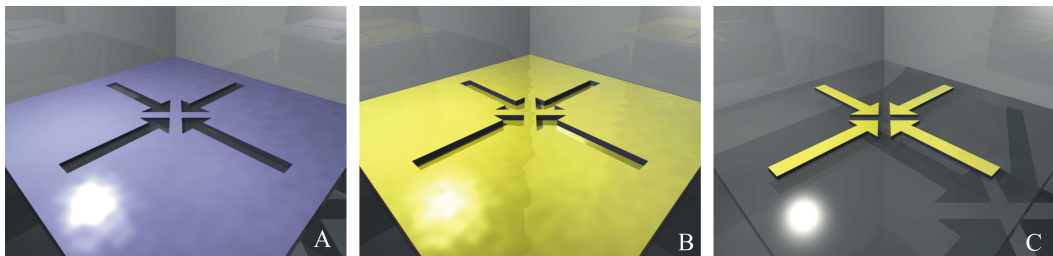


Figure 4.15: This diagram shows the process for creating a DEP chamber by e-beam lift off. The resist is first patterned by e-beam lithography (A) then a layer of gold is evaporated (B), finally the resist is removed just leaving gold in the previously opened windows(C).

Copies of this pattern were then created by lift off photolithography described in section 3.2.3.1. A complicated two stage lift-off procedure is not necessary with e-beam liftoff as the resist naturally give a negative profile (an overhang). This process creates a negative of the desired image which can

### 4.3. FABRICATION

---

then be used in the same way as a mask to create the final desired pattern (see figure 4.16).

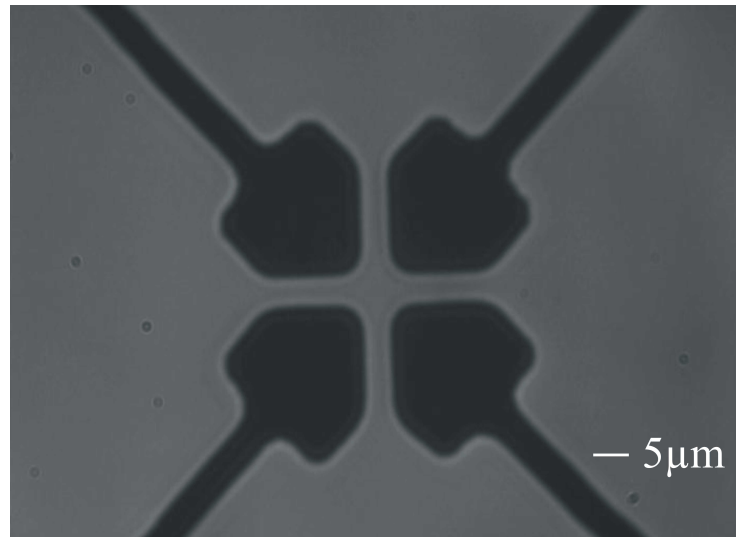


Figure 4.16: This diagram shows the completed DEP chamber. The dark areas are gold.

Finally wires are attached to the leads using silver conductive paint. The chamber is then placed into the optical setup (see section 4.4.1) before a  $10 \mu L$  drop of colloid is placed onto it and a cover slip is placed on top.

## 4.3. FABRICATION

---

### 4.3.2 Light Induced Dielectrophoresis (LIDEP) chamber

A simple chamber for LIDEP experiments was created. It consists of a top and bottom component with the photoconductive a-Si layer being part of the bottom component (see figure 4.17).

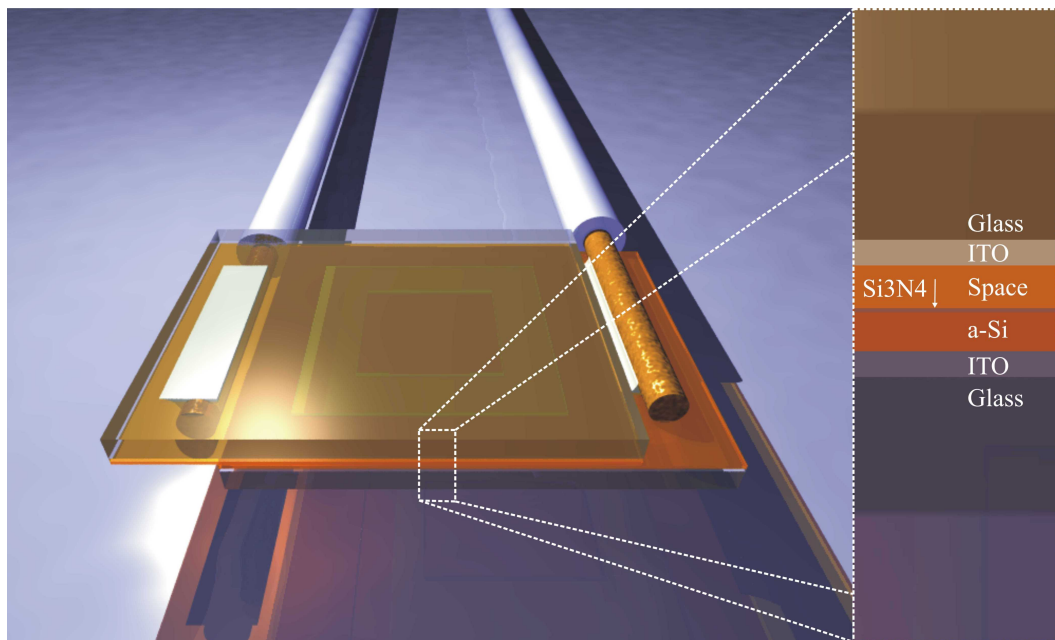


Figure 4.17: Diagram of a LIDEP chamber. It consists of a top component of ITO coated glass with an SU-8 spacer patterned onto it. The bottom component is a piece of ITO coated glass that has had a-Si then  $Si_3N_4$  coated onto it.

This layer was deposited from a silane/hydrogen mixture in a microwave plasma system by John Wilson at Heriot-Watt University onto ITO coated glass. I then evaporated an insulating layer of silicon nitride ( $Si_3N_4$ ) onto this and attached a wire to the ITO layer by removing part of the a-Si and  $Si_3N_4$  layers and using silver conductive paint. The top component consists

### 4.3. FABRICATION

---

of ITO coated glass with a spacer patterned onto it. I created the spacer by patterning SU-8 with photolithography. By mixing different amounts of SU-8 2000.5 (which usually spins on to about  $0.5 \mu m$  thick) and SU-8 2050 (which usually spins on to about  $50 \mu m$  thick) any thickness from  $0.5$  to  $50 \mu m$  can be achieved. I used spacers from  $25$  to  $5 \mu m$  thick with a typical recipe for a  $5 \mu m$  spacer being;

3:1, SU-8 2050:2000.5, spun at 5000rpm. Heated on a hotplate at  $65^\circ C$  for 5 mins, then  $95^\circ C$  for 5mins. Exposed to UV on a Karl Suss mask aligner for 60s and heated again as before before developing in EC solvent for 90s.

A wire was then attached to this component with silver conductive paint. The two components were put together in the optical setup (see section 4.4.1) with a  $2\mu L$  drop of colloid in the center and held together with a clamp. A layer of petroleum jelly was also smeared between the components to slow the rate of evaporation.

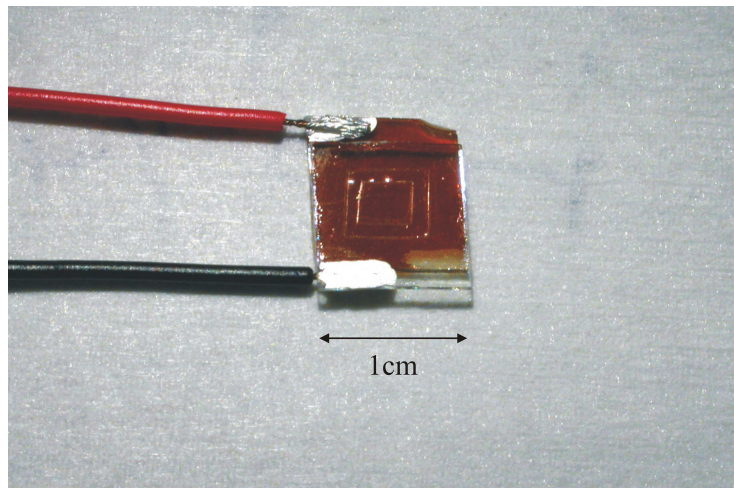


Figure 4.18: This figure shows the LIDEP cell with the two components placed on top of each other. The brown colour comes from the a-Si and the square in the center is the SU-8 spacer.

### **4.3. FABRICATION**

---

It is important to note the simplicity of the LIDEP chamber construction. No micrometer scale fabrication is necessary making the build much faster and cheaper than a classical dielectrophoresis chamber. This is possible as the spatial definition of the electrical fields is created by the light pattern rather than by lithography.

## 4.4. OPTICAL SETUP

---

### 4.4 Optical setup

#### 4.4.1 Light Induced Dielectrophoresis (LIDEP) with a laser

The basic optical setup used for the Light Induced Dielectrophoresis (LIDEP) experiments is shown in figure 4.19.

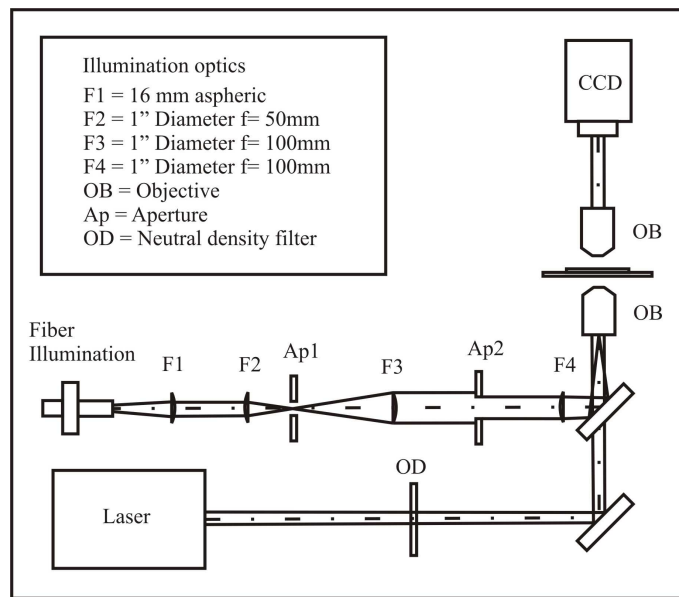


Figure 4.19: The optical setup for LIDEP experiments.

Classical dielectrophoresis experiments were also carried out on this setup but without using a laser. For LIDEP, the illumination of the sample is very important. As the laser and the illuminating light come through the same objective normally they would be focused in the same plane giving poor illumination at the focus of the laser. To control this, a Köhler illumination setup is used. Here the illuminating light is focused in the plane of a diaphragm called the condenser diaphragm which then controls the amount of light that reaches the sample. It is then collimated before passing through a second diaphragm

#### 4.4. OPTICAL SETUP

---

called the field diaphragm that controls the area of the sample illuminated. This second diaphragm is imaged onto the back of the objective so that now the illuminating light is focused at a different distance from the objective than the laser which is collimated as it enters the objective. In this way we have complete control over the amount of light that reaches the sample, the area it covers and where it is focused.

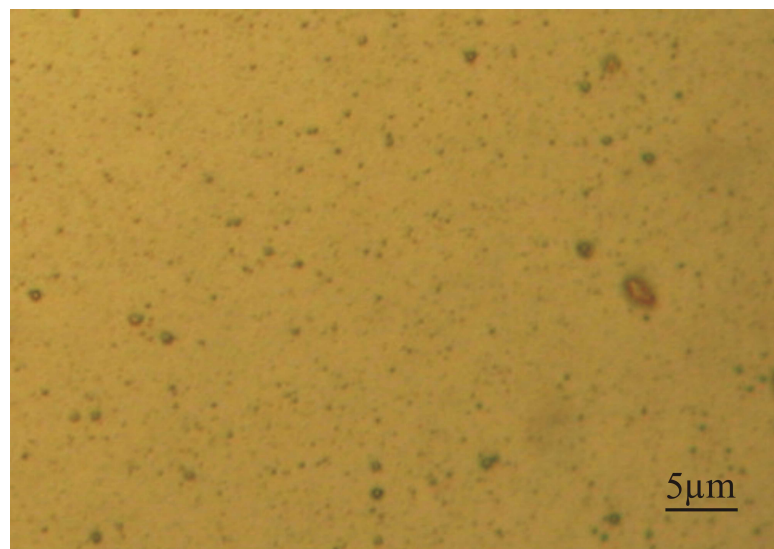


Figure 4.20: A good a-Si layer. Highlighting the inherent non-uniformity of the a-Si used here.

This is especially important as the amorphous silicon layers used here were very nonuniform. Although the layers have good electrical properties they appear quite rough under a microscope. The poor quality hinders the quality of the imaging (see figure 4.20).

## 4.4. OPTICAL SETUP

---

### 4.4.2 LIDEP with a data projector

The use of Spatial Light Modulators (SLMs) is widespread in optical tweezing allowing the creation of any optical pattern desired. These work by patterning a laser beam usually with a Liquid Crystal Display (LCD) onto which a hologram is displayed. However as LIDEP requires much less optical intensity than optical tweezing we can use a much cheaper light patterning device, a data projector [16]. The technology is very similar, with either an LCD or Digital Light Processing (DLP) chip patterning the light, but they only cost 1/10th of the price of an SLM and you do not need a laser. An optical setup reduces the image from the data projector onto the a-Si layer (see figure 4.21). Two telescopes are used, a 1/2 and then a 1/4, to reduce the image by a factor of 8 before it is passed through an objective that is chosen to give the desired image size.

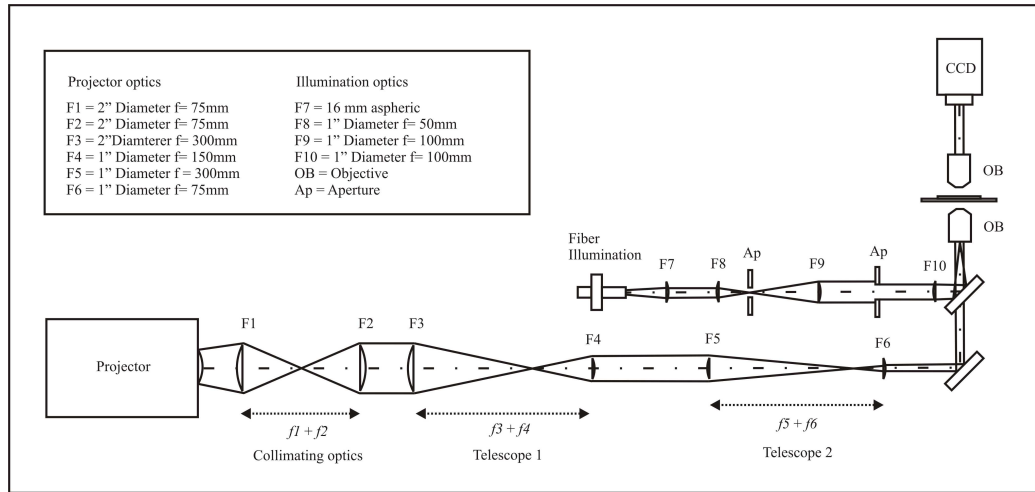


Figure 4.21: An optical setup designed to reduce the image from a data projector onto the a-Si layer.

Here the image is collimated before passing it through two reducing tele-

#### **4.4. OPTICAL SETUP**

---

scopes and into the back aperture of the objective. This setup has the potential to give real time control over a large area.

## 4.5. RESULTS

---

# 4.5 Results

## 4.5.1 Traditional dielectrophoresis (DEP)

A traditional dielectrophoresis (DEP) chamber was constructed as described in section 4.3.1 to help my understanding of DEP and provide a comparison to Light Induced Dielectrophoresis (LIDEP). One micrometer diameter latex spheres were used as the colloid and the chamber was placed into the optical setup including a laser explained in section 4.4.1. The conductivity of the water the colloid was suspended in was measured to be  $0.2\text{mSm}^{-1}$ . The signal generator used was a Thurlby Thander TG215 2MHz function generator capable of delivering up to 16V peak to peak at frequencies up to 2MHz. Figure 4.22A shows the pattern of applied voltages. The opposite electrodes have similar sign voltages while the adjacent electrodes are 180 degree out of phase so the voltage on an electrode is negative when the one next to it is positive.

This gives areas of high electric field gradient between adjacent electrodes (coloured red in figure 4.22, A) and an area of low electrical field gradient in the center of the electrodes (coloured blue in figure 4.22, A). When a low frequency AC voltage is applied, the particles experience a positive DEP force and are attracted to the areas of high electric field (figure 4.22, B). When a high frequency voltage is applied the particles experience a negative DEP force and collect in the center of the electrodes where the electric field gradient is less. This agrees well with theory as the Clausius-Mossotti factor for a latex sphere goes from positive at low frequency to negative at high frequency as shown in figure 4.22D. The frequency at which the force goes from positive to negative is called the crossover frequency and measuring this frequency can be useful in characterizing colloidal particles. In this case the crossover frequency was measured to be 1.1 MHz.

## 4.5. RESULTS

---

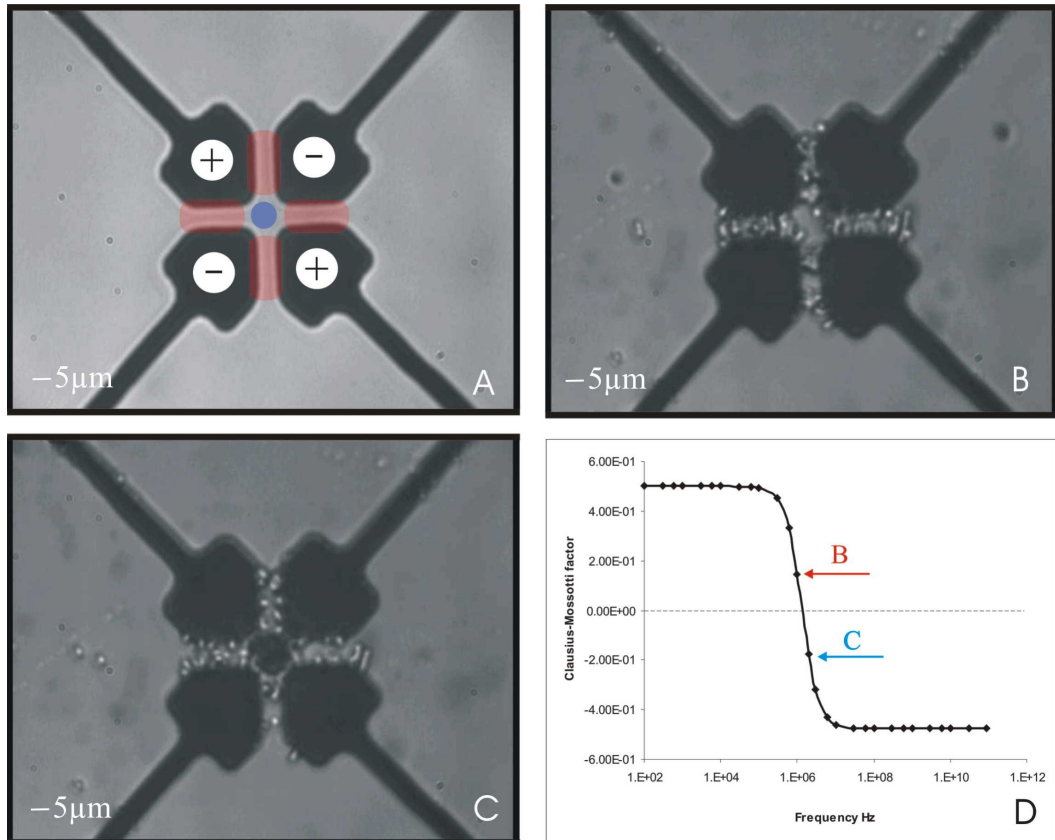


Figure 4.22: Traditional dielectrophoresis. A) The dielectrophoresis chamber. Areas of high and low electric field gradient are highlighted in red and blue respectively. B) A voltage of 16V peak to peak is applied at 1 MHz giving positive DEP. C) The same voltage is applied at 2 MHz giving negative DEP. This traps many of the particles in the center of the electrodes. D) The CM factor with the frequencies for B and C marked.

## 4.5. RESULTS

---

### 4.5.2 Dielectrophoresis (DEP) of red blood cells

To see how cells react to the dielectrophoretic (DEP) force an experiment was carried out using a traditional DEP chamber and red blood cells. Red blood cells were chosen for their interest in haematology and ease of harvesting. Due to the small nature of the DEP chamber only a small amount of blood was needed and a single pin pick gave enough for several experiments. The blood was taken by pricking an alcohol wiped area of skin with a sterile lance and collected in a heparin coated capillary to prevent coagulation. For the DEP effect the conductivity of the medium is important however for the cells to remain viable they need an isotonic buffer solution. Normal buffer solutions contain many dissolved salts and are very conductive, so a less conductive sugar solution was used. An 8.5% sucrose, 0.3% dextrose solution was used giving a conductivity around  $10mSm^{-1}$  [3]. When an AC voltage was applied, the cells were observed to be repelled (negative DEP) at low frequency and attracted (positive DEP) at high frequency (See figure 4.23).

This is the opposite to what was found with latex colloid however it agrees well with theory when the shell like nature of the cells are taken into account (see section 4.1.3). This experiment shows how it is possible to manipulate cells using the dielectrophoretic force.

## 4.5. RESULTS

---

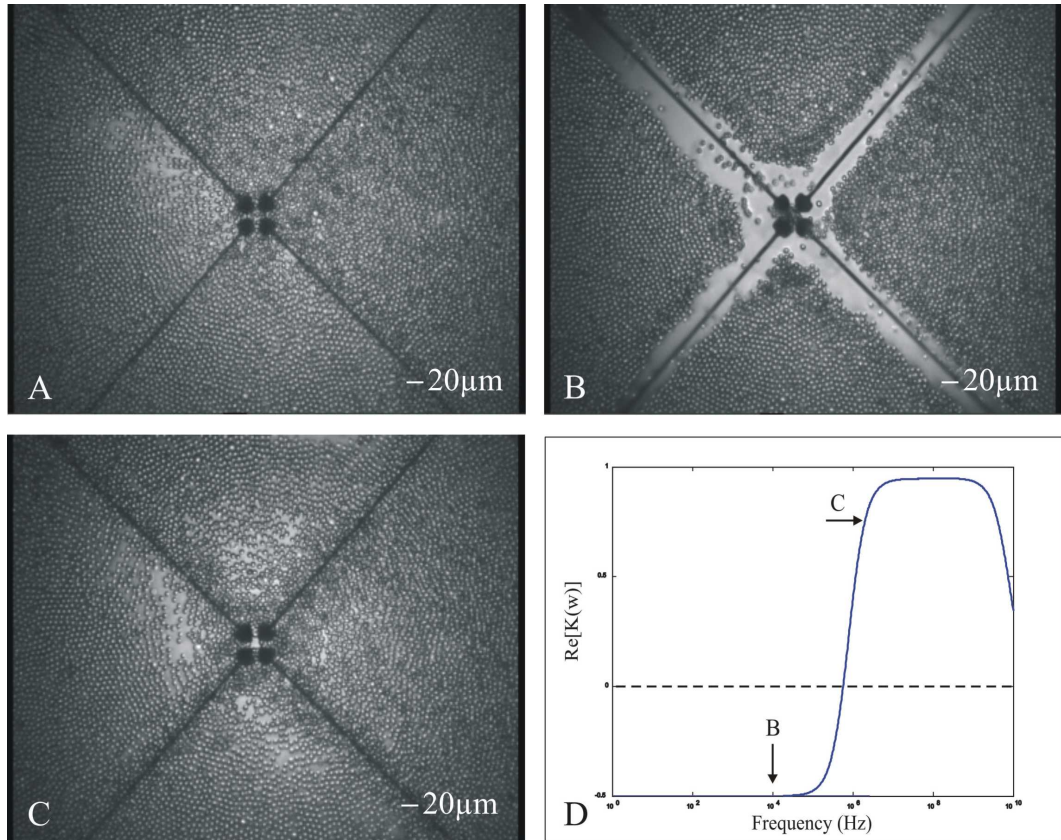


Figure 4.23: Red Blood Cell (RBC) dielectrophoresis (DEP). A) The DEP chamber. The RBC's are distributed evenly throughout the chamber. B) A voltage of 16V peak to peak is applied at 10 kHz giving negative DEP. C) The same voltage is applied at 1 MHz giving positive DEP. D) The Clausius-Mossotti factor for a RBC with the frequencies corresponding to B and C marked.

## 4.5. RESULTS

---

### 4.5.3 Light Induced Dielectrophoresis (LIDEP)

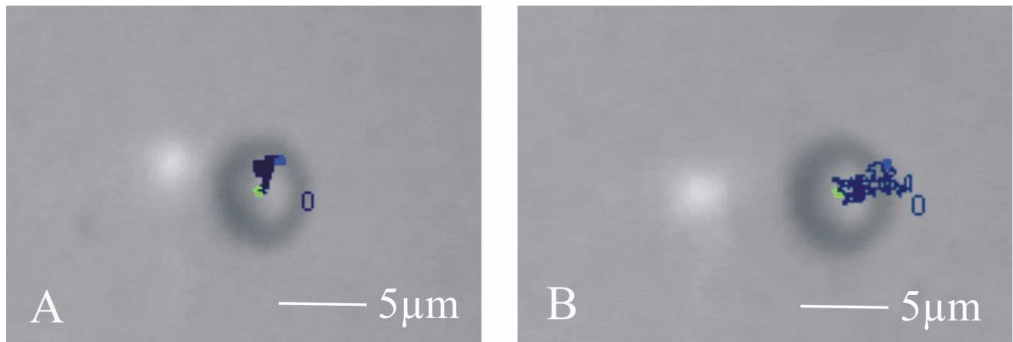


Figure 4.24: Plots of the trajectories of particles over 750 frames with the stage moving at A)  $0.2\mu ms^{-1}$  and B)  $1.6 \mu ms^{-1}$ . The trajectories are overlayed onto a still of first frame of the movie analysed.

A sample chamber was constructed as shown in section 4.3.2. SU-8 spacers of various thickness were tried and the thickness of the chamber was measured by focusing on the top then the bottom of the chamber and measuring how far the stage moves with a micrometer. It was found that the chamber height changed each time the chamber was set up even with the same spacer. This was probably due to colloid or some vaseline, which was used to stop the sample from drying out, getting between the spacer and the substrate. A more reliable way to control the height was to omit the SU-8 spacer and use two different size colloid. The larger colloid is trapped between the two plates thereby accurately fixing the chamber height. A height of  $50 \mu m$  was found to be most convenient; although a thinner chamber would give a larger force, it would dry out quicker, thereby not giving time for a quantitative experiment. At  $50 \mu m$  height, the sample lasted roughly 30 mins with the experiment running. A red laser pointer was used as the light source with an output of 2.9 mW (0.9 mW at the sample) at a wavelength between 630-680 nm.  $5 \mu m$  diameter polymer

## 4.5. RESULTS

---

colloid was used as the analyte and the suspending medium has a conductivity of  $0.2 \times 10^{-4} Sm^{-1}$ .

The stage holding the chamber was moved relative to the optical spot using a motorised stage. As the stage moves in relation to the spot, the particle is pushed towards the spot by the dielectrophoretic force but away from the spot by the drag force of the liquid. The particle rests at an equilibrium position where the dielectrophoretic force equals the drag force. By calculating the drag force, we can thus measure the dielectrophoretic force on the particle and by increasing the velocity we can measure the force at different distances from the optical spot. This measurement therefore yields a map of the potential landscape that the particle experiences. The velocity of the stage was increased until the particle was no longer trapped. The position of the particle just before it was not trapped is the position of the maximum force on the particle which we define as the size of the trap.

Figure 4.5.3 shows stills taken from videos of the stage moving at 0.2 and  $1.6 \mu ms^{-1}$  overlayed with plots of the trajectories of the particles over 750 frames. The trajectories were measured using particle tracking software described in section 1.2.1. Figure 4.5.3 shows that the faster the stage is moved the further from the optical spot the particle sits.

### 4.5.3.1 Plotting the force against displacement

Each movie, corresponding to a certain velocity of the stage, gives a set of 750 coordinates of the center of the particle which are fitted to a Gaussian distribution. These Gaussians are plotted in figure 4.25A. Two groups of curves can be seen, the group on the left corresponding to the stage moving right to left and the group on the right corresponding to the opposite direction. The position of the center of these Gaussians is then plotted in figure 4.25B against

## 4.5. RESULTS

---

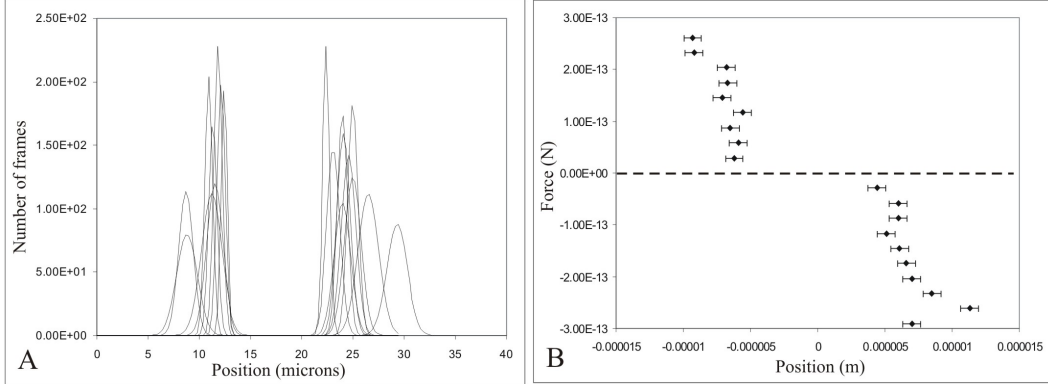


Figure 4.25: Distance of particle from optical spot. A) the Gaussian distributions of the particles position. B) The position of the center of the Gaussian plotted against corresponding drag force.

the drag force calculated using Stoke's law see equation 4.17. The average value of  $\sigma$  for the Gaussians gives a measure of how well the position of the particle can be measured, so this is used as the error in the displacement. A force to the right is defined as positive and to the left negative.

$$F_{drag} = 6\pi r \eta \nu \quad (4.17)$$

Where  $F_{drag}$  is the drag force,  $r$  is the Stokes radius (here just the radius of the sphere),  $\eta$  is the viscosity and  $\nu$  the velocity of the particle. The particle is close to a surface so it is also necessary to take into account Faxen's correction [12][13] given by equation 4.18;

$$F_{drag} = \frac{6\pi r \eta \nu}{\left(1 - \frac{9}{16}\left(\frac{r}{h}\right) + \frac{1}{8}\left(\frac{r}{h}\right)^3 - \frac{45}{256}\left(\frac{r}{h}\right)^4 - \frac{1}{16}\left(\frac{r}{h}\right)^5\right)} \quad (4.18)$$

Where  $h$  is the distance from the surface to the center of the particle. This correction to the drag coefficient (defined as  $F_{drag} = \beta \nu$  where  $\beta$  is the drag coefficient) is plotted in figure 4.26 for a sphere of  $2.5 \mu m$  radius and liquid

## 4.5. RESULTS

---

viscosity  $1 \times 10^{-3} \text{ Pas}$ .

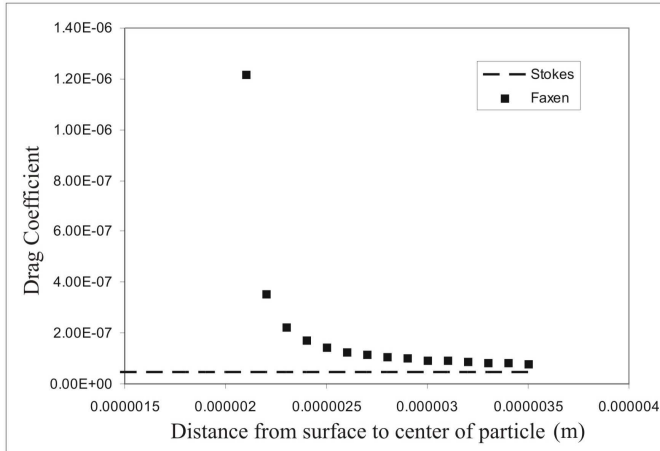


Figure 4.26: The drag coefficient as given by Stokes law and Faxen's correction for a sphere approaching a surface.

This gives a more accurate value of the drag force than just using Stoke's drag but is not complete as it does not hold for a particle coming in close to the surface ( $a \approx h$  [14]). It also does not account for the effect of friction between the particle and the surface. This experiment was repeated three times with different objectives giving different optical spot sizes. The size of the optical spots were measured by taking frames of video and using National Instruments Vision Assistant to do a line scan. This gives the value of the pixels in the frame which can then be fitted to a Gaussian curve (see figure 4.27A).

The size of the spot is taken as the Full Width Half Maximum of the Gaussian calculated as  $2.35 \times \sigma$ . The three different objectives used, 50x, 20x and 10x, gave optical spots of 2.3, 3.3 and 5.0  $\mu\text{m}$  diameter. The results of these three experiments are plotted in figure 4.27B. This shows the surprising result that although as the optical spot is reduced from 5 to 3.3  $\mu\text{m}$  the electrical trap size is reduced from 10.5  $\mu\text{m}$  to 8.6  $\mu\text{m}$ , when the optical spot is further

## 4.5. RESULTS

---

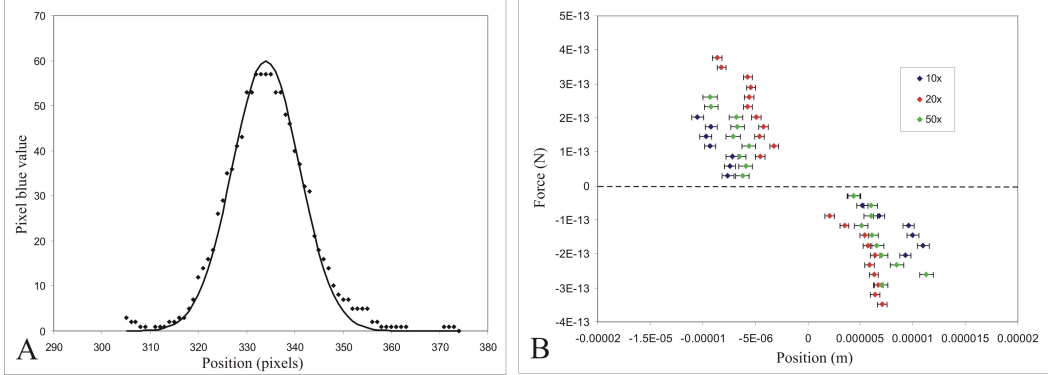


Figure 4.27: A) The optical spot using the 50x objective measured from a video still. This was converted into meters by calibrating the imaging system with a lithographically created pattern of known size. B) The experiment was repeated with three different objectives 10x, 20x and 50x giving 3 different spot sizes.

reduced to  $2.3 \mu\text{m}$  the size of the electrical trap does not reduce again but increases to  $9.3 \mu\text{m}$  radius. To explain this we compared the results with simulations.

### 4.5.3.2 Comparing force against displacement results with theory

To fit this data to theory, simulations were performed as described in section 4.2. The photoconductivity of the a-Si is simulated by assuming the conductivity changes from its dark conductivity of  $1 \times 10^{-4} \text{ Sm}^{-1}$  to its maximum light conductivity of  $1 \times 10^{-2} \text{ Sm}^{-1}$ . The simulation gives the gradient of the square of the electric field which is plotted as a function of position and height above the surface in figure 4.28A. The line representing 500nm above the surface is also shown in figure 4.28B but converted into force using equation 4.1. For this calculation a Clausius-Mossotti factor of 0.005 was used which can be

## 4.5. RESULTS

---

calculated from equation 4.2 using a frequency of 2MHz, a bulk conductivity of  $1 \times 10^{-16} Sm^{-1}$  and a surface conductivity of  $1.56 \times 10^{-8}$ . This value for surface conductivity was not measured but chosen so that the magnitude of the calculated force was similar to the experimentally measured force.

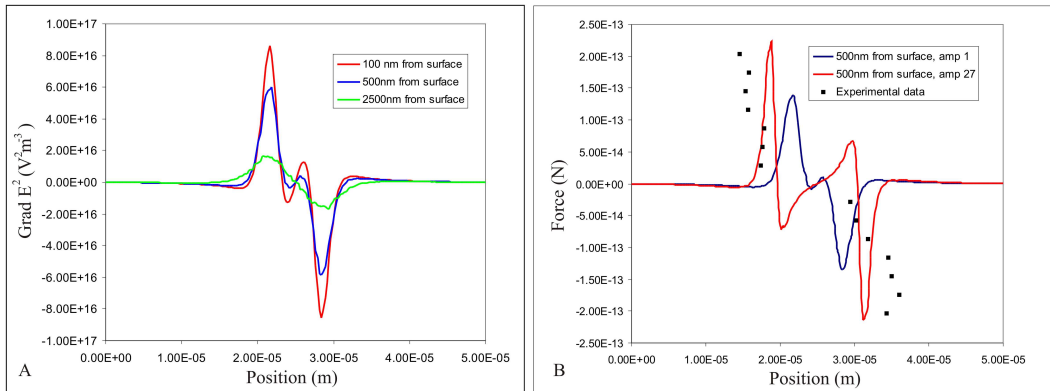


Figure 4.28: A) Simulated data for a 5 micrometer optical spot for 3 different heights above the surface. B) The data is shown for the case where the conductivity varies from the minimum to the maximum in a gaussian profile and for the case of the conductivity is saturated by a gaussian with 27 times the amplitude of the first case.

The optical spot used for figure 4.28A was  $5 \mu\text{m}$  in diameter; in contrast, the peaks of force are  $8 \mu\text{m}$  apart. This is due to the peak gradient in the resistivity being further from the center of the optical spot than the peak gradient in the conductivity. Figure 4.28A also shows that it is not just the strength of the force that changes with height above the surface but also the shape of the curve. For a particle  $2.5 \mu\text{m}$  from the surface the force curve is close to a straight line for small displacements from the center of the optical spot. This could then be described using Hooke's law  $F = -kx$  and the spring constant  $k$  which, if found, would give the stiffness of the trap (see

## 4.5. RESULTS

---

section 4.5.3.3). The curves representing the force at smaller distances from the surface do not show a force that is proportional to the displacement but instead have small peaks of the opposite sign to the larger peaks. These would represent a force away from the center of the optical spot and would result in a ring trap.

The experimental data for a 5 micrometer optical spot is compared to simulated data in figure 4.28B. There are two simulated lines, one showing the case where there is gaussian change in resistivity (as assumed before). The other represents the case where the conductivity is saturated by a gaussian 27 times the amplitude of the first case. The value of 27 was calculated from comparing the optical intensity used in this experiment with that required to saturate a 1 micrometer a-Si:H film from literature [10]. As the power was kept the same for the 3 different objective lenses and the spot size decreases the amplitude of the gaussian was adjusted accordingly to give gaussians 27, 60 and 123 times the original amplitude for the 10, 20 and 50 times objectives. The resulting conductivities can be seen in figure 4.29.

Figure 4.28B also shows that when the photoconductor has been saturated the repulsive force (a force that pushes the particle away from the center of the optical spot) is exaggerated. This is still positive DEP as the particle is being attracted to an area of high electric field gradient and comes from the fact that when the photoconductor is saturated there is a larger area of constant resistivity in the a-Si in the center of the trap giving zero electrical field gradient. This attracts particles to edges of the optical spot where there is a high gradient giving a ring trap similar to that found in optical tweezing when a ring of light is used such as a Laguerre-Gaussian beam. The experimental data can be seen to agree with this as although the points for positive and negative force each form reasonable straight lines the lines do not join up

## 4.5. RESULTS

---

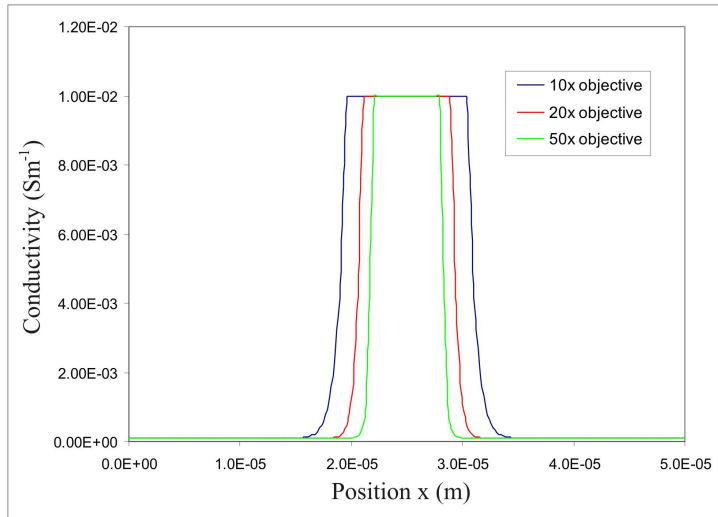


Figure 4.29: A Gaussian optical spot creates a Gaussian conductivity profile.

If the amplitude is increased so that it saturates the photoconductor a flat top profile is formed.

through the point  $2.5 \times 10^{-5} m$ , the center of the optical spot, but are offset.

Figure 4.28A also shows that the force is stronger closer to the surface. This shows a limitation of the equation 4.1 that does not allow for the force to vary over the volume of the colloid. This results in the colloid experiencing a stronger force than suggested by the line for  $2.5\mu m$  from the surface that would normally be chosen to represent a  $5\mu m$  diameter colloid at the interface. To account for this I have chosen to use the line representing 500nm from the surface as an effective distance for the colloid. This was chosen as the shape of this line fits well with the experimental data.

The simulated force vs displacement 500nm from the surface is plotted with the experimental data for the three optical spot sizes in figure 4.30. This shows that the experimental results fit much better with the simulated forces for the 5 and  $3.3\mu m$  spot sizes than for the  $2.3\mu m$  spot. To quantify this

## 4.5. RESULTS

---

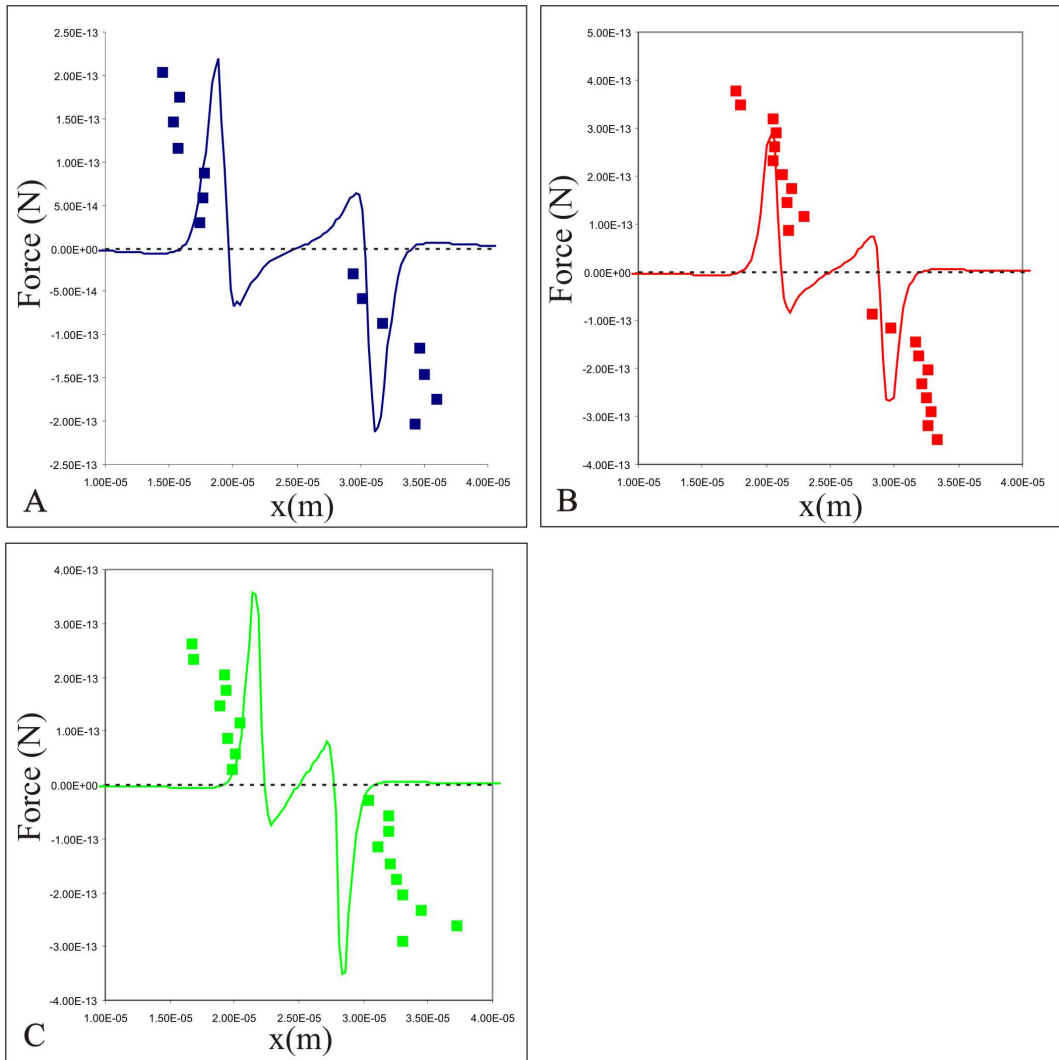


Figure 4.30: Dielectrophoretic force plotted against position. Experimental measurements (shown as squares) are plotted with simulations (shown as lines) for the A) 10x objective, B) 20x objective and C) 50x objective.

the difference in the simulated and experimentally measured x positions of the peak force were calculated. An average for this difference was then taken from the positive and negative force peaks. Then dividing this by the distance of

## 4.5. RESULTS

---

the peaks from the center of the optical spot, gives an error that is the fraction of the trap size that the two disagree by. This was calculated as 0.29 for the 10x objective, 0.39 for the 20x objective and 0.67 for the 50x objective. One possible reason for the increase in the error is that as the optical spot decreases in size the gradients vary over decreasing distance. Thus again we reach the limit of equation 4.1 which assumes that the gradient is the same over the volume of the colloid. As the gradients in the x direction now vary over a distance comparable to the size of the colloid they experience both positive and negative forces and can not accurately be modeled as a simple dipole. This means that the position of the peak force on the particle will vary with the size of the particle.

These results can be summarised as showing that the size of the electrical trap is dependant on the size of the optical spot but also on;

- The position of the peak gradient of the resistance (as this is frequency dependent at high frequencies, see figure 4.10, the trap size is frequency dependant).
- The input optical power (this will cause saturation shown in figure 4.29).
- The particle size (this only has an effect when the optical spot is of similar size to the particle, see figure 4.30).

### 4.5.3.3 Trap stiffness

The experiments described in this chapter were carried out using a laser pointer as a light source with just 0.9mW reaching the sample. This demonstrates the advantage of LIDEP over optical tweezing of requiring less input light to activate. In order to compare the two techniques more quantitatively it is necessary to compare the trap created as well as the light intensity required.

## 4.5. RESULTS

---

To do this we have measured the trap stiffness of a LIDEP trap and compared it to stiffness values of optical traps from literature [15].

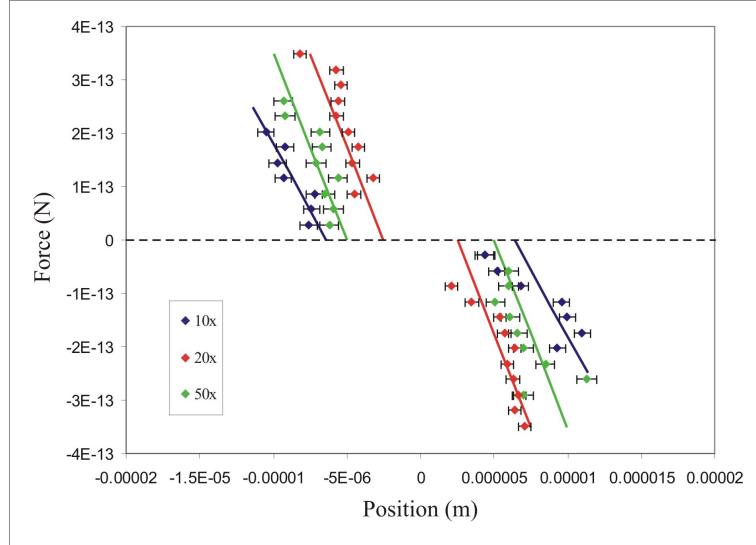


Figure 4.31: Straight lines are fitted to the experimental data the gradient of which are taken as the trap stiffness.

The stiffness of a trap is defined as the force it takes to move a particle a given distance in the trap in  $Nm^{-1}$ . It can be calculated as the gradient of line of best fit for the experimental data for the three spots (see figure 4.31). It would also be possible to draw a straight line through the origin to the point of maximum force to represent the trap stiffness. As a particle at the origin would travel to here under this force this would seem reasonable, however for a particle sitting at equilibrium in the trap the lines shown give a more accurate measure of the stiffness they experience. The stiffness was measured as  $5 \times 10^{-8} Nm^{-1}$  for the  $5 \mu m$  optical spot and  $7 \times 10^{-8} Nm^{-1}$  for the 3.3 and  $2.3 \mu m$  optical spots. From literature, an optical trap using 225 mW optical power gives a stiffness of  $5 \times 10^{-6} Nm^{-1}$ . To compare these, we can use

## 4.5. RESULTS

---

stiffness per input power as a figure of merit as the stiffness of an optical trap is proportional to the input power giving optical traps  $2.2 \times 10^{-8} Nm^{-1} mW^{-1}$  and LIDEP  $7.8 \times 10^{-8} Nm^{-1} mW^{-1}$ . Optical tweezers also need the input light to be more tightly focused with an irradiance of  $10^5$  to  $10^7 W cm^{-2}$  [10]. This compares to the experiment shown above with the 10x objective using just  $4.6 \times 10^3 W cm^{-2}$ .

## 4.6. CONCLUSIONS

---

# 4.6 Conclusions

## 4.6.1 Dielectrophoresis (DEP)

Dielectrophoresis experiments have been carried out to compare to LIDEP experiments. The dielectrophoretic behavior of colloid and cells have been studied and compared to standard theory. Colloid experiences a positive force at low frequencies and a negative force at high frequencies with the crossover frequency for  $1\mu m$  diameter latex colloid around 1.1MHz. It has been shown that red blood cells show a negative force at low frequencies and a positive force at high frequencies, the opposite of colloid, as is consistent with theory for a shelled object.

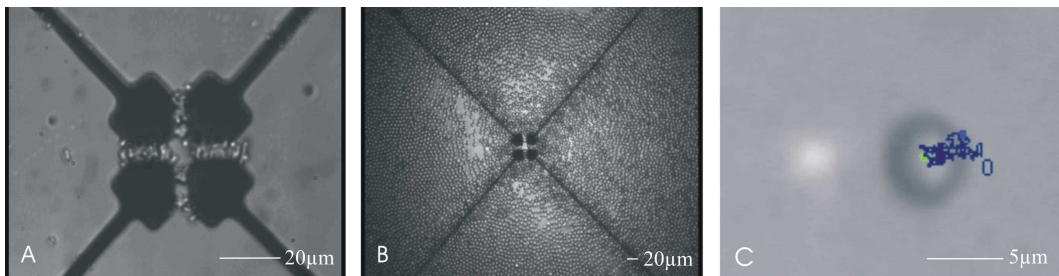


Figure 4.32: DEP force comparison. A) Positive DEP of colloid at 1MHz. B) Positive DEP of RBCs at 1MHz. C) Positive LIDEP of colloid at 2MHz

## 4.6.2 Light Induced Dielectrophoresis (LIDEP)

LIDEP experiments have been demonstrated that show manipulation of  $5\mu m$  polymer colloid is possible and the trajectories of these particles have been analyzed to measure the resolution they can be manipulated with. Reducing the optical spot size from  $5\mu m$  to  $3.3\mu m$  caused a reduction in the DEP trap

## 4.6. CONCLUSIONS

---

from  $10.5 \mu m$  to  $8.6 \mu m$  radius. A further reduction in optical spot size to  $2.3 \mu m$ , however, did not reduce the trap size further giving a trap radius of  $9.3 \mu m$ .

Comparing these results with theory shows us that the gradients of the electrical field, that cause the DEP response, vary over distances comparable to the particle size. This means that for optical spots that are large compared to the particle, the force can be described by simple dielectrophoretic theory. However for optical spots that are small compared to the particle, here  $2.3 \mu m$ , just under half the particles diameter, the simple DEP theory does not describe the forces on the particle well. To gain a better description of the force on the particle with a nonuniform gradient, a more complicated description of the DEP force will be needed that accounts for the presence of not just one dipole in the particle but multipoles [9].

A comparison of the traps created by LIDEP and optical tweezing has been performed. The stiffness per input optical power has been used as a figure of merit and LIDEP gave over 3 times the stiffness per Watt. Comparing the optical irradiance necessary for each technique gives a 20 times reduction in the irradiance necessary for LIDEP. This enhancement is less than previously suggested [10]. One reason for this is that these experiments were performed with 0.9 mW, the power from a laser pointer. As the simulations suggest the photoconductor is being saturated, it should be possible to reduce the power used thus increasing the power advantage of LIDEP over optical tweezing. It would also be advantageous to indirectly measure the trap stiffness by either measuring the thermal fluctuations of the particle [12] or by finding the trap's oscillation frequency [15]. This would give a measure of the trap strength independent of the drag force so that we would not need to know the drag coefficient. Here we have calculated the drag coefficient using Faxen's correction

## 4.6. CONCLUSIONS

---

but as we have not allowed for friction with the surface this could still be too low.

### 4.6.3 Future development

Simulations show that reducing the chamber height increases the force due to LIDEP without loosing any of the resolution. In this way, it should be possible to produce a stiffer trap with the same input light and voltage. To do this, it will be necessary to create a flow chamber for LIDEP as the present method of trapping the colloid between two plates would suffer from evaporation. If the chamber is reduced to a height similar to the size of the particle the upper surface will also have an effect on the drag coefficient of the particle making it harder to move. This may give an optimum height for the chamber for a given particle size.

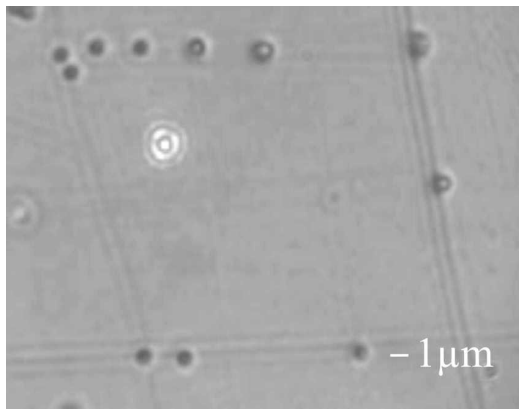


Figure 4.33: Scratches in the photoconductive layer cause electric field gradients larger than those created by the light induced electrode. This causes the particles to be attracted to the faults rather than the light.

To produce an optimized cell sorting device using LIDEP it will be neces-

## 4.6. CONCLUSIONS

---

sary to know the size of the electrical trap created by a given optical spot, as we have shown here, but the minimum optical power necessary to produce this trap. For this reason future work should include reducing the optical power and remeasuring the LIDEP trap size. With these two pieces of information it would be possible to calculate the optimum amount to demagnify the image from a data projector onto the photoconductive surface so that the least number of pixels are used to create each LIDEP trap.

Another limitation of LIDEP is the need for a faultless photoconductive layer. Any scratches or imperfections in this layer create larger electric field gradients than those created by the light induced electrode (see figure 4.33). This causes the particles to be attracted to the faults rather than the light. One way to make more uniform substrates may be to use sputtering rather than vapor deposition to produce the film of a-Si:H. It may also be possible to use a photo-conducting polymer such as polyvinyl carbazole (PVK) to produce a more uniform photoconductive layer.

---

## BIBLIOGRAPHY

- [1] Dholakia K. and Reece, P. Optical micromanipulation takes hold, *Nano Today* 1, 18 (2006).
- [2] Gascoyne R.C., and Vykoukal J., Particle seperation by dielectrophoresis, *Electrophoresis* 23, 1973-1983 (2002).
- [3] Chiou P.Y., Ohta A.T. and Wu M.C., Massively parallel Manipulation of single cells and microparticles using optical images. *Nature* 436, 370-372 (2005).
- [4] Pohl H.A., *Dielectrophoresis*, Cambridge University Press, Cambridge, 1978.
- [5] Value taken from Wikipedia [www.wikipedia.org](http://www.wikipedia.org)
- [6] COMSOL Electromagnetics Module Users Guide, Magnetostatic and Quasi Static Fields.
- [7] Value calculated by squaring refractive index for a Polystyrene divinylbenzene (PS-DVB) colloid with refractive index 1.59 [www.dukescientific.com](http://www.dukescientific.com)

## BIBLIOGRAPHY

---

- [8] Hughes M.P., Nanoelectromechanics in engineering and biology, CRC Press (2003) gives a value of  $1 \times 10^{-9} \text{ Sm}^{-1}$  here we take  $2 \times 10^{-9} \text{ Sm}^{-1}$  as it fits with experimental results see figure 4.22.
- [9] Hughes M.P., Nanoelectromechanics in engineering and biology, CRC Press (2003).
- [10] Chiou P.Y., Ohta A.T. and Wu M.C., Toward all optical lab-on-a-chip system: optical manipulation of both microfluid and microscopic particles. Proc. Optical Trapping and Optical Micromanipulation SPIE Vol. 5514, 73-81.
- [11] MacDonald MP, Spalding GC, Dholakia K. Microfluidic sorting in an optical lattice. Nature Vol 426 p421-424.
- [12] Svoboda K. and Block S.M., Biological applications of optical forces. Ann. Rev. Biophys. Biomol. Struct. 23: 247-285 (1994).
- [13] Happel and Brenner, Low Reynolds Number Hydrodynamics, Prentice Hall (1965)
- [14] Vermeulen K.C., Wuite G.J.L., Stienen G.J.M. and Schmidt C.F., Optical trap stiffness in the presence and absence of spherical aberrations, Applied Optics, 45, 1812-1819 (2006).
- [15] Joykutty J., Mathur V., Venkataraman V. and Natarajan V. Direct measurement of the oscillation frequency in an optical trap by parametric excitation. Physical Review Letters 96, 193902 (2005).
- [16] Lu, L-S., Huang, Y-P., Yeh, J.A., Lee, C., and Chang, Y.H. Controllability of non-contact cell manipulation by image dielectrophoresis (iDEP). Optical and Quantum Electronics 37, 1385-1395 (2005).

## BIBLIOGRAPHY

---

- [17] Green N.G., Morgan H. Separation of submicrometer particles using a combination of dielectrophoretic and electrohydrodynamic forces. *J. Phys. D: Appl. Phys.* 31 25-30 (1998).
- [18] Pethig R. Dielectrophoresis: Using inhomogeneous AC electrical fields to separate and manipulate cells. *Critical Reviews in Biotechnology*, 16(4): 331-348 (1996).
- [19] Taff B.M., Voldman J. A scalabe addressable positive-dielectrophoretic cell-sorting array. *Anal. Chem.* 77: 7967-7983 (2005).
- [20] Gascoyne P., Hahidol C., Ruchirawat M., Satayavivad J., Watcharasit P., Becker F.P. Microsample preparation by dielectrophoresis: isolation of malaria. *Lab Chip* 2: 10-75 (2002).
- [21] Minerick A.R., Zhou R., Takhistov P., Chang H-C. Manipulation and characterization of red blood cells with alternating current fields in microdevices. *Electrophoresis* 24: 3703-3717 (2003).
- [22] Hu X., Bessette P.H., Qian J., Meinhart C.D., Daugherty P.S., Soh H.T. Marker-specific sorting of rare cells using dielectrophoresis. *PNAS* 102 (44): 15757-15761 (2005).

---

---

# CHAPTER 5

---

## Conclusions

### 5.1 Microgears

We have demonstrated the design, fabrication and testing of form birefringent microgears. The form birefringence allows the transfer of Spin Angular Momentum (SAM) from a circularly polarised beam to the microgears causing them to rotate. The first microgears were made from silicon however it was found that they were not attracted to areas of high intensity as the scattering forces were stronger than the optical gradient force. Using the lower refractive index of SU-8 allowed the microgears to be optically trapped leading to a successful demonstration of optically actuated rotation. The magnitude of the birefringence was measured as  $\Delta n_{eff} = 0.015 \pm 0.001$  which was similar to the simulated value of  $\Delta n_{eff} = 0.018 \pm 0.001$ . The microgears rotated at a maximum rate of 80 rpm when illuminated with 1W of light.

## 5.1. MICROGEARS

---

### 5.1.1 Increasing the rotation rate

To increase the rotation rate it will be necessary to increase the torque exerted on the microgear by each incident photon. This can be done either by increasing the birefringence, making the microgear thicker or passing each photon through the microgear many times.

#### 5.1.1.1 Increasing the birefringence

Making the microgear thicker to increase the torque per photon will be technologically difficult due to the hight aspect ratios needed. An easier alternative is to increase the birefringence. This can be done by increasing the refractive index of the microgear material. Simulations have shown that for silicon (refractive index 3.5) a birefringence as high as 0.5 could be achieved. To reduce the scattering forces the reflections could be reduced with an antireflection (AR) coating. A 150nm layer of OptiNDEX A14 would make a suitable AR coating. By increasing the birefringence, the torque on the microgear per photon could be increased up to a maximum where the microgear is acting as a 1/2 wave plate. This will increase the rotation rate up by a factor of up to 100 compared to the results presented here.

#### 5.1.1.2 Multiple pass system

Once the microgear is acting as a 1/2 wave plate, the torque can not be increased by increasing the birefringence or the thickness of the microgear. However it can be increased by passing each photon through the microgear many times. To do this the microgear would have to be placed in a cavity that corrects the phase of the light so that every pass of the light pushes the microgear in the same direction. To do this  $3/4 \pi$  wave plates need to be placed between the microgear and the mirrors of the cavity. The torque will then be increased

## **5.2. OPTICAL SORTING**

---

by a factor equal to the Q factor of the cavity.

### **5.1.2 Microgear applications**

The main advantage of the microgears we have demonstrated is the ease in which they can be manipulated. They can be rotated simply by placing them in a circularly polarised beam and do not rely on scattering so can be optically tweezed. They were originally designed as a pumping mechanism for a Lab-on-Chip (LOC) application. However the LOC application would need to only require tiny volumes of liquid due to the small size and slow rotation rate of the microgears. An application that does not require high rotation rates would be a microrheometer that could measure the local viscosity in biological samples. Here the microgears have the advantage of precise dimensions so that the drag coefficient can be calculated accurately. The rotation rate can also be conveniently measured by looking at the transmitted light. They may also find other applications in biology such as placing shear stresses on cells to monitor their responses.

## **5.2 Optical Sorting**

Flow chambers for optical sorting experiments have been created. Different fabrication techniques have been tried and the finished flow chambers have been tested to find the maximum flow rate that could be used for sorting.

### **5.2.1 Fabricating a flow chamber**

Two methods were tried to create flow chambers. First, creating the channels in photoresist and then glueing them to a cover slide. This was unreliable with no amount of glue giving unblocked channels repeatedly. The second method

### **5.3. LIGHT INDUCED DIELECTROPHORESIS (LIDEP)**

---

was using PDMS and and a soft lithography process. This was found to be reliable and gave good channels suitable for optical tweezing experiments.

#### **5.2.2 Maximum flow rate for optical sorting**

A flow chamber was used with an interference pattern to demonstrate optical sorting and find the maximum flow rate that could be sorted. Previous experiments simulated flow by moving a sample with respect to the optical pattern. By using the chamber, however, it was possible to show that sorting could also be performed in a real flow. The maximum flow rate was  $50\mu Lmin^{-1}$  with the lattice at  $10^\circ$  and this decreased roughly proportionally with increasing lattice angle. Optical sorting is a very elegant technique as it uses the inherent optical properties of the particles to discriminate and to sort. In order to compete with established cell sorting technology, it will be necessary to increase the rate that particles can be sorted at. One way to do this may be to increase the area over which particles can be sorted by using light induced dielectrophoresis (LIDEP) rather than an optical force. The interference pattern used here has an area of  $2 \times 10^3 \mu m^2$  where it has been shown that LIDEP can manipulate particles over an area of  $1 \times 10^6 \mu m^2$  [1], 500 times the area.

## **5.3 Light Induced Dielectrophoresis (LIDEP)**

### **5.3.1 Designing a LIDEP device**

To design the optics of a LIDEP device it is necessary to know two parameters. The shape of the input beam needed to produce the shape of the electrical field gradients desired, and the minimum irradiance necessary to "turn on" the photoconductor to do this. We have addressed these two issues, first by

## 5.3. LIGHT INDUCED DIELECTROPHORESIS (LIDEP)

---

measuring the shape of the electrical trap created by different optical spots, then by looking at the stiffness of the traps produced.

### 5.3.1.1 Comparing the optical spot size to the electrical trap size

It has previously been proposed that the size of trap achievable is limited just by the size of optical spot it is possible to create and hence the diffraction limit of the light used [2]. This is suggested as the diffusion of carriers in a-Si is smaller than the diffraction limit for visible wavelengths so that the trap is not broadened by the movement of the carriers. The results shown here, however, demonstrate that the size of the trap is also dependent on other parameters. Firstly, the electrical spot is dependant on the gradient of the resistivity and the peaks in resistivity gradient are wider apart than the width of the optical spot. Second, the input power can cause the trap to broaden. If a power larger than that necessary is used the conductivity becomes saturated which increases the trap size. Also the size of the particle is important. If the trap becomes similar to the size of the particle the electrical gradient will vary over the volume of the particle, which in this case caused a broadening of the trap.

### 5.3.1.2 Trap stiffness

The stiffness of the traps produced were measured and a comparison made with optical trapping. The stiffness per input optical power for LIDEP was  $7.8 \times 10^{-8} Nm^{-1}mW^{-1}$  compared to a typical value for optical traps of  $2.2 \times 10^{-8} Nm^{-1}mW^{-1}$ . However it should be possible to reduce the optical power used for LIDEP and hence increase this figure of merit. Optical tweezers also need the input light to be more tightly focused with an irradiance of  $10^5$  to  $10^7 Wcm^{-2}$  [3]. This compares to the experiment shown above with the 10x objective using just  $4.6 \times 10^3 Wcm^{-2}$ .

## 5.3. LIGHT INDUCED DIELECTROPHORESIS (LIDEP)

---

### 5.3.1.3 Using two photoconductive layers

It may be possible to increase the gradients of the electric field by reducing the size of the top electrode. This could be done by using two photoconductive layers and illuminating both (see figure 5.1). Although a Gaussian beam would not have sufficient depth of focus to illuminate both photoconductive layers this could be done by illuminating one with a beam from the top and one with a beam from the bottom. A more elegant solution would be to use a non-diffracting beam shape such as a Bessel beam as shown in figure 5.1.

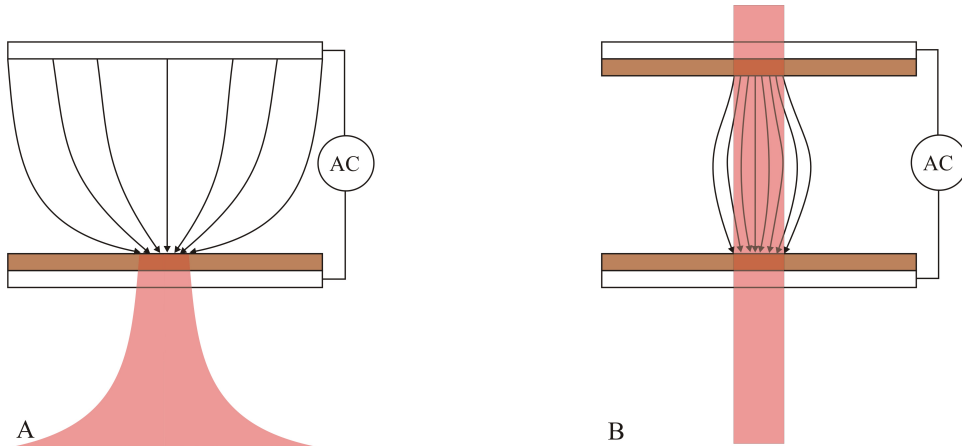


Figure 5.1: Using two a-Si layers (shown here in brown) it may be possible to increase the electric field gradients by reducing the size of the top electrode.

## 5.3.2 Combining a LIDEP chamber with microfluidic channels

### 5.3.2.1 Microfluidic channels between two conducting plates

After the optics of the device have been designed, it is only necessary to combine microfluidic channels onto the substrate to complete the device. There

### **5.3. LIGHT INDUCED DIELECTROPHORESIS (LIDEP)**

---

are two different ways to combine LIDEP with microfluidic channels. One is to produce a network of channels between the two conducting plates. This is a more difficult task than producing the channels shown in section 3.2.3 as it requires the precise control of the height of the channels, no thick layer of PDMS on top and to be bonded to two different surfaces. A possible method would be to use photolithography to define channels in a resist and then bond them together using a layer of glue. However I have found it this method to be unreliable, see section 3.2.2. Another way to do this would be to produce patterned PDMS channels that could be bonded to the ITO and insulating layers. This would require PDMS channels with no top, which can not be done using soft lithography. One could, however, fabricate such structures by starting with a flat layer of PDMS and using conventional photolithography and etching to create the patterned channels.

#### **5.3.2.2 A one sided LIDEP chamber**

The other method is to produce a LIDEP chamber that does not require two conducting plates. This could be done by creating two electrically isolated areas on the photoconductive surface and passing the AC across these. The LIDEP pattern then could be drawn between these two areas creating the horizontal electrical field gradients necessary for dielectrophoresis that may be even stronger than those created with vertical LIDEP (see figure 5.2). If this is possible it then will be easy to incorporate channels onto the device in the same way as before (see section 3.2.3).

#### **5.3.3 The future of LIDEP**

LIDEP will only survive where it has a clear advantage over the established methods of optical tweezing and dielectrophoresis, as it has the disadvantage

### 5.3. LIGHT INDUCED DIELECTROPHORESIS (LIDEP)

---

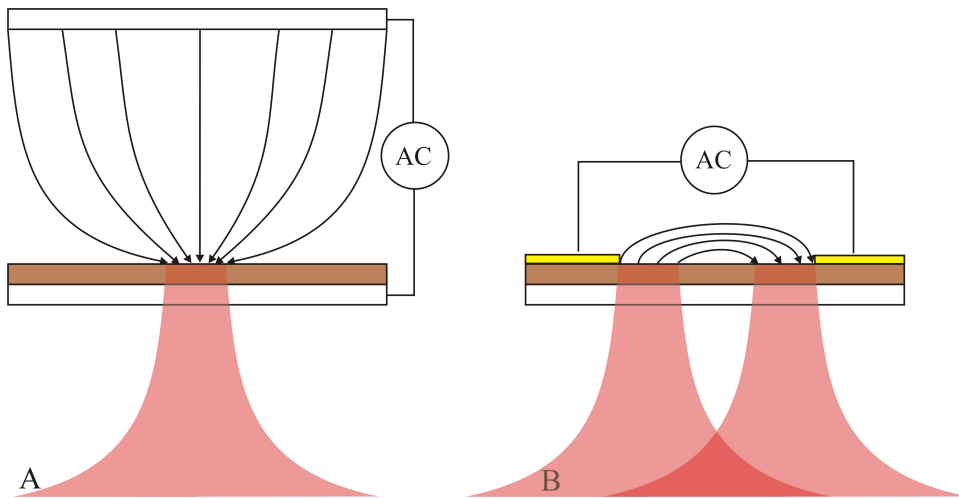


Figure 5.2: The AC is dropped between the two metal contacts shown in yellow. The light pattern is then focused onto the photoconductor shown in brown between the electrodes creating the desired virtual electrode pattern.

of needing a chamber that includes conductive and photoconductive layers. It must also overcome the disadvantage of not giving vertical control of the trapped particle as in optical tweezing. At present it appears that LIDEP has two main advantages, producing similar control as optical tweezing with less input optical power and demonstrating control over arrays of particles that optical tweezing can not. As it takes less irradiance to activate the a-Si's photoconductivity than is needed for optical tweezing LIDEP devices can give control over a much larger area. Alternatively it could allow the construction of a device that does a similar task as an optical tweezing device with a much cheaper light source.

Both optical tweezing and dielectrophoresis offer control over a range of biological particles such as suspended cells. However one crucial advantage of LIDEP may be how selectivity it can move one species of particle and not

## 5.4. OPTICALLY CONTROLLED MICROFLUIDICS

---

another. Most biological sample have similar optical properties with a slightly higher refractive index than water and so respond to an optical trap in the a similar way. Similarly most have similar electrical properties such as an insulating shell surrounding a more conductive center. Thus they show a similar response to a dielectrophoretic trap. However dielectrophoresis is frequency dependent and for each particle, there is a frequency where the force goes from positive to negative. Any small difference in the particle's electrical properties may change this crossover frequency allowing us to distinguish between two very similar particles. In this way, we may be able to demonstrate a level of control that is impossible with optical tweezing alone.

## 5.4 Optically controlled microfluidics

The results shown in this thesis show that optics can be used to control microfluidics. Optical forces can be used to either move microgears that can be used to move fluid (see section 2), or to move particles through fluids (see section 3). The forces that result, however, are small (pN to fN) limiting their usefulness. In Lab-on-Chip (LOC) devices with typical channel dimensions of  $100\mu m$  optical forces alone will not be enough for fluid pumping. Optical particle manipulation on such a device may turn out to be useful as the force available is enough to move cells on a small scale. Using optics to control electrical forces (see section 4) can increase the force per incident photon on a particle. This may give the critical extra level of control that allows the creation of a viable cell sorting device that uses optically controlled actuation.

The main benefit that optics bring to LOC devices is the ease of control. As it is easy to change the shape of an incident light pattern they become continually reconfigurable. This is a great advantage in a research lab as

#### **5.4. OPTICALLY CONTROLLED MICROFLUIDICS**

---

the experiment can be continually changed and tuned. It is not necessary, however, in a LOC device designed for a specific purpose, such as cell sorting. Thus optically controlled microfluidics will be most beneficial and hence find its first applications in the research lab.

---

## BIBLIOGRAPHY

- [1] Chiou P.Y., Ohta A.T. and Wu M.C., Massively parallel Manipulation of single cells and microparticles using optical images. *Nature* 436, 370-372 (2005).
- [2] Ohta A.T., Chiou P., Jamshidi A., Hsu H., and Wu M.C. Optically-controlled manipulation of live cells using incoherent light-driven opto-electronic tweezers. *SPIE Optics and Photonics* 2006, 6326-45.
- [3] Chiou P.Y., Ohta A.T. and Wu M.C., Toward all optical lab-on-a-chip system: optical manipulation of both microfluid and microscopic particles. *Proc. Optical Trapping and Optical Micromanipulation SPIE* Vol. 5514, 73-81.